INVESTIGATING ACTIVE GALACTIC NUCLEI IN LOW-MASS SYSTEMS:

FEEDBACK AND SEEDS OF SUPERMASSIVE BLACK HOLES

by

Sheyda Salehirad

A dissertation submitted in partial fulfillment
of the requirements for the degree

of

Doctor of Philosophy

in

Physics

MONTANA STATE UNIVERSITY
Bozeman, Montana

May 2025

DEDICATION

To my mom, who always believed in me when others doubted. To my brother, whom I miss deeply and feel watching over me.

ACKNOWLEDGEMENTS

I gratefully acknowledge Dr. Amy Reines for her invaluable advice and support throughout my PhD program at Montana State University. I also extend my appreciation to the Physics department faculty and staff at Montana State University for their substantial assistance along the way. Finally, I thank my family for their unwavering love and encouragement.

Support for this work was provided by Montana State University, NASA through the EPSCoR grant number 80NSSC20M0231, and the NSF through CAREER award 2235277.

TABLE OF CONTENTS

TABLE OF CONTENTS – CONTINUED

LIST OF TABLES

LIST OF FIGURES

LIST OF FIGURES – CONTINUED

Figure Page

LIST OF FIGURES – CONTINUED

Figure Page

LIST OF FIGURES – CONTINUED

Figure Page

LIST OF FIGURES – CONTINUED

Figure Page

LIST OF FIGURES – CONTINUED

Figure Page

LIST OF FIGURES – CONTINUED

Figure Page

LIST OF FIGURES – CONTINUED

Figure Page

NOMENCLATURE

$M_\odot$	Solar mass
M_*	Stellar mass
BH	Black hole
AGN	Active galactic nucleus
PC	Parsec
EW	Equivalent width

ABSTRACT

Massive black hole (BH) populations in dwarf galaxies and their outflows provide key insights into supermassive BH seed formation and galaxy evolution. This dissertation examines active galactic nuclei (AGNs) in low-mass systems through two projects. First, I identify 388 new AGN candidates in low-mass galaxies ($M_* < 10^{10} M_\odot$ and $z < 0.3$) from 23,460 Galaxy and Mass Assembly (GAMA) survey spectra and using four optical diagnostics: two narrow emission-line ratio diagnostic diagrams and two high-ionization coronal lines. Of these, 47 exhibit broad Hα emission, indicating virial BH masses of $M_{BH} \sim 10^5 - 10^{7.7} M_\odot$. This multi-diagnostic approach reveals a diverse AGN population, from blue star-forming dwarfs to "miniquasars", extending prior Sloan Digital Sky Survey searches to higher redshifts and new sky regions. Second, from 39,612 GAMA galaxies, I detect 398 with outflow signatures, of which 45 are among low-mass objects. I searched for second velocity components in the [O III]$\lambda\lambda 4959, 5007$ doublet emission-line profiles and found that the outflow velocities are generally faster in AGNs than those in star-forming galaxies across massive and low-mass systems. This work emphasizes the key role of AGN-driven outflows in low-mass galaxies, requiring their integration into galaxy evolution models. These results advance our understanding of BH seeding and feedback in low-mass regimes.

1

INTRODUCTION

Supermassive black holes (BHs) with masses ranging from $M_{BH} \sim 10^6 - 10^{10}\ M_\odot$ are a fundamental feature of massive galaxies, growing through merger-driven accretion over cosmic time (Kormendy & Ho, 2013). When material accretes onto these BHs, it powers active galactic nuclei (AGNs), which span a wide luminosity range from low-luminosity systems to the brilliant quasars of the early universe. While supermassive BHs dominate in massive galaxies, their origins are far from understood.

The Active Galactic Nucleus Unification Model

The supermassive BH serves as the central engine of an AGN. The current model describing the geometric arrangement of regions surrounding the BH integrates several key components (see Figure 1 for a schematic illustration):

1. **Accretion Disk**: A flat, rotating disk of gas encircles the central BH ($\sim 0.01 - 0.1$ pc). Angular momentum causes the material to flatten into a disk and spiral inward. Frictional heating can raise temperatures to millions of degrees, emitting radiation across the electromagnetic spectrum (Lasota, 2022). This emission ionizes gas in the surrounding regions.

2. **Broad-Line Region (BLR)**: Located beyond the accretion disk ($0.1 - 1$ pc), the BLR consists of dense gas clouds orbiting the supermassive BH at velocities up to thousands of kilometers per second (Czerny & Hryniewicz, 2011; Shen, 2013). These rapid motions produce broadened permitted emission lines such as the Balmer series (Hα and Hβ), a characteristic of Type 1 AGNs.

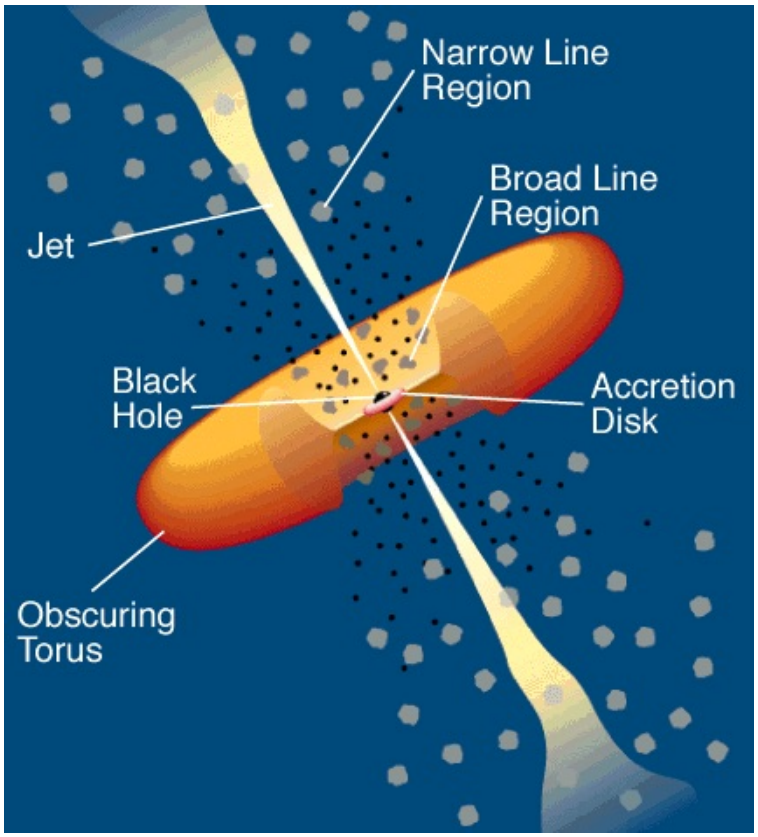

Figure 1: A schematic of the current AGN unification model (not to scale). This model accounts for the observed diversity of AGNs, from head-on views revealing jets to edge-on Type 2 AGNs with an obscured BLR. See section 1 for details. Image credit: C.M. Urry & P. Padovani. `https://heasarc.gsfc.nasa.gov/docs/objects/agn/agn_model.html`.

3. **Obscuring Torus**: A thick doughnut-shaped ring of dust surrounds the BLR ($\sim 1 - 100$ pc). The torus obscures the accretion disk and BLR from certain viewing angles, explaining why some AGNs lack broad emission lines. These obscured systems, known as narrow-line AGNs or Type 2 AGNs, appear different due to this orientation-dependent effect.

4. **Narrow-Line Region (NLR)**: Situated outside the torus ($100 - 1000$ pc), the NLR is a lower-density cloud of gas ionized by the radiation from the accretion disk. Here, gas moves more slowly (100 to 1000 km s^{-1}), producing narrower emission lines. The conditions in this region allow for the emission of "forbidden" transitions, such as

[O III]λ5007 and [N II]$\lambda\lambda$6548, 6583, alongside Balmer lines.

5. **Jets and Outflows**: In some AGNs, radiation pressure, magnetic fields, or thermal winds from the accretion disk drive outflows. These can manifest as gas expelled at hundreds to thousands of kilometers per second or as collimated relativistic plasma jets aligned with the spin axis of the black hole (Blandford et al., 2019).

Active Galactic Nucleus Observation in the Optical Regime

AGNs can be identified through the multi-wavelength radiative signatures of material accreting onto central BHs (see Ho, 2008, for a review). Current diagnostics distinguish between sources excited by stellar photoionization and photoionization by the spectrally hard radiation field of an accretion disk. The accretion disk's higher fraction of high-energy photons creates partially ionized regions around the BH, ideal for producing forbidden emission lines like [N II], [S II], [O III], and [O I]. In contrast, massive young stars have thin partially ionized zones, so a stronger ratio of forbidden lines to Balmer lines (e.g., Hα, Hβ) often signals AGN activity. This principle underpins optical two-dimensional line ratio diagnostic diagrams (Baldwin et al., 1981; Shirazi & Brinchmann, 2012; Veilleux & Osterbrock, 1987).

Broad emission lines, such as Hα, may arise from the BLR near the BH, though stellar processes like supernovae can also produce similar features. Additionally, coronal emission lines with high ionization potentials are stronger under the hard radiation of an AGN, providing another indicator of an accreting BH in a galaxy.

Active Galactic Nucleus in Low-mass and Dwarf Galaxies

The discovery of high-redshift quasars with masses reaching billions of solar masses, when the universe was only about 1 billion years old (e.g., Mortlock et al., 2011), suggests that supermassive BHs originated with masses exceeding those of stellar-mass BHs and

underwent rapid growth over cosmic time. Despite this, no definitive model has emerged to explain their origins (e.g., Inayoshi et al., 2020). Some researchers propose that the death of massive population III stars could have produced supermassive BH seeds with masses $M_{BH} \sim 100\ M_{\odot}$ (Fryer et al., 2001). However, these seeds would require exceptionally fast accretion to achieve the supermassive BH masses observed in the early universe. Alternative scenarios, such as gravitational runaway processes in dense stellar clusters or the collapse of gas clouds, have been suggested as mechanisms capable of forming more massive seeds, with masses ranging from $M_{BH} \sim 10^3 - 10^6\ M_{\odot}$ (Antonini et al., 2019; Begelman et al., 2006; Giersz et al., 2015; Lodato & Natarajan, 2006). These different models are shown in Figure 2.

Investigating BH seeds in the early universe offers the most direct way to address this question, but their faintness and small size make them undetectable with current facilities. Over the past two decades, observations of massive BHs in dwarf galaxies, those with stellar masses $M_* < 3{*}10^9\ M_{\odot}$ or in some cases $M_* < 10^{10}\ M_{\odot}$, have provided an alternative avenue for exploring the origins of supermassive BHs (see, Greene et al., 2020; Reines, 2022, and the references therein). The relatively calm merger histories of dwarf galaxies (Bellovary et al., 2011), which influence the availability of material for accretion within the gravitational reach of a BH, combined with supernova remnants that can suppress BH growth (Anglés-Alcázar et al., 2017), suggest that BHs in these galaxies remain relatively pristine, with masses closer to their initial seed values. Additionally, a correlation exists between observed BH masses and the masses of their host galaxies, with more massive galaxies typically harboring more massive BHs (Baldassare et al., 2015; McConnell & Ma, 2013; Reines & Volonteri, 2015). Models of BH growth across cosmic time further indicate that evidence of the dominant formation mechanisms should be preserved in dwarf galaxies. Since light BH seeds are expected to be more common than their heavier counterparts, the BH occupation fraction in dwarf galaxies, the proportion hosting massive BHs, could help distinguish between seeding

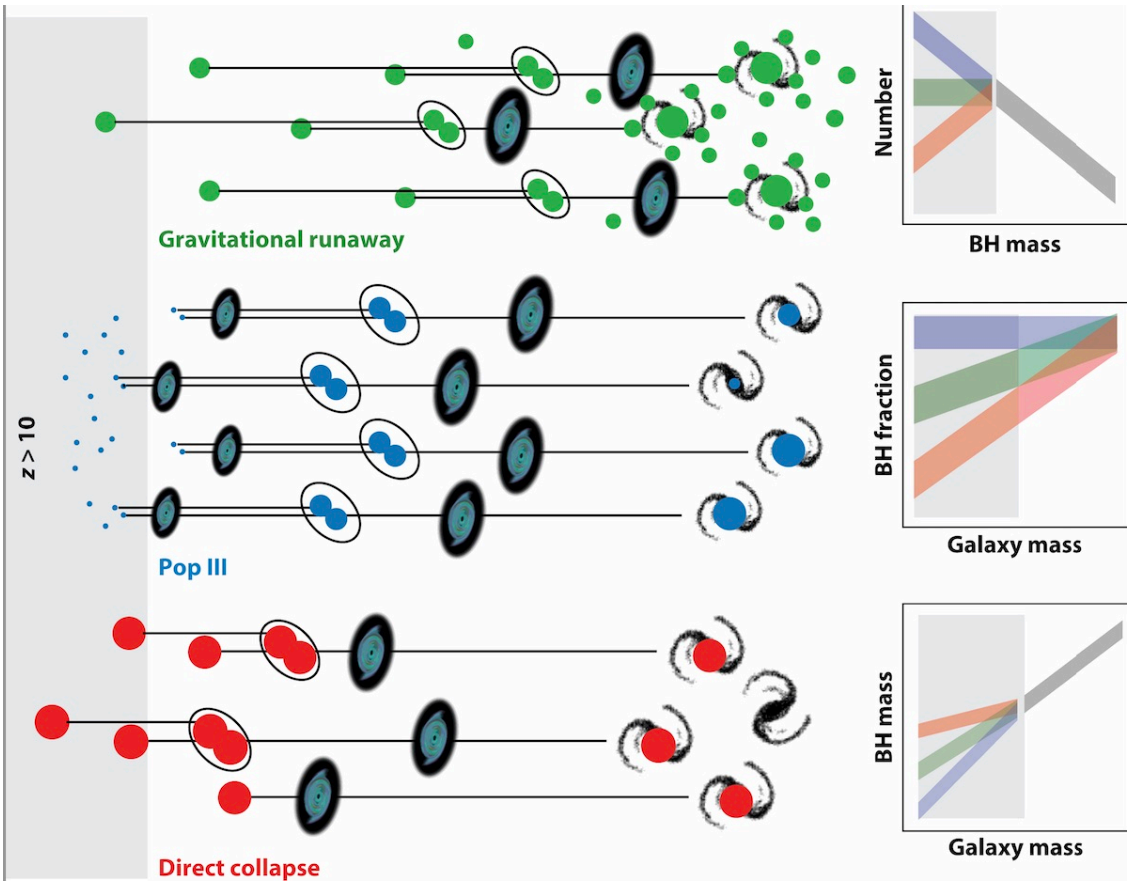

Figure 2: Various potential observable indicators of different BH seeding mechanisms, as outlined in Greene et al. (2020). The right panels display the BH functions, occupation fractions, and scaling relations for three scenarios: gravitational runaway (shown in green), Population III stars (in blue), and direct gas collapse (in red). Gray areas indicate regions lacking observational constraints. Formation via direct collapse or Population III stars occurs at redshifts $z > 10$, whereas gravitational runaway events may take place across cosmic time. BH mergers throughout cosmic history (depicted as black ovals) can emit gravitational waves, while accretion events, observed as AGNs (shown as blue disks), also occur.

mechanisms (Volonteri et al., 2008). Examining the low-mass end of scaling relations, such as the $M_{BH} - \sigma_*$ relation, using BHs in dwarf galaxies may also shed light on the processes that initiated supermassive BHs. Ultimately, detecting the least massive BHs in dwarf galaxies could establish an upper limit on the masses of supermassive BH seeds.

Active Galactic Nucleus Outflows

Observational and theoretical studies have revealed a connection between the evolution of central BHs and their host galaxies. Observations show a relationship between BH mass, the mass of the galaxy's bulge, and the stellar velocity dispersion (Ferrarese & Merritt, 2000; Gültekin et al., 2009). Theoretical models suggest that this co-evolution may be driven by material expelled into the interstellar medium by AGNs through radiation and outflows, a process known as AGN feedback (Silk & Rees, 1998; Vogelsberger et al., 2014). Without including feedback in these models, key observed galaxy properties, such as the abrupt drop-off at the high end of the galaxy luminosity function, cannot be accurately replicated (e.g., Baldry et al., 2012; Bower et al., 2006).

Over the past two decades, AGN feedback has been observed in numerous galaxies (Alexander et al., 2010; Carniani et al., 2015; Cicone et al., 2014; Fluetsch et al., 2021; Rupke & Veilleux, 2011; Veilleux et al., 2005) and is believed to play a critical role in regulating star formation. Evidence exists for both the suppression of star formation (negative feedback; Hopkins et al., 2006; Pereira-Santaella et al., 2018) and its enhancement (positive feedback; Cresci et al., 2015; Schutte & Reines, 2022). However, the role of AGN feedback in dwarf galaxies remains uncertain. Some observational and theoretical studies argue that outflows driven by stellar processes dominate in this mass range (e.g., Martín-Navarro & Mezcua, 2018; Trebitsch et al., 2018), while other models suggest that AGN feedback is the primary mechanism quenching star formation (Barai & de Gouveia Dal Pino, 2019; Dashyan et al., 2018). Recent high-resolution zoom-in simulations of dwarf galaxies further highlight the

potential significance of AGN feedback in these systems (Koudmani et al., 2021, 2019). Thus, detecting and analyzing AGN-driven outflows in dwarf galaxies is essential for understanding their impact in this mass regime.

The presence of broad-line features in the [O III]$\lambda\lambda$4959, 5007 doublet line profile has been used as a tracer for ionized gas outflows (Heckman et al., 1981; Stockton, 1976). Gas motions exceeding typical dynamics in the NLR around a BH can appear as asymmetrical features and broadened wings in these lines, observable on galaxy-wide scales.

Overview of This Work

In this dissertation, I present original contributions to the study of massive BHs and outflows in low-mass and dwarf galaxies. My research leverages data from the Galaxy and Mass Assembly (GAMA) Survey, which remains relatively unexplored compared to widely used surveys like the Sloan Digital Sky Survey (SDSS). I developed Python-based code to analyze the spectra of tens of thousands of galaxies, fitting the stellar continua and absorption lines, and used multi-Gaussian models to characterize emission lines.

In Chapter 2, I describe the methodology for systematically identifying AGN candidates within approximately 24,000 low-mass galaxies using GAMA spectra (Salehirad et al., 2022). To minimize biases associated with optical diagnostics, I applied four distinct AGN diagnostic techniques. This effort produced a completely new catalog of low-mass active galaxies, expanding the known population of AGNs in this mass range and extending the search to deeper southern skies and higher redshifts.

In Chapter 3, I present newly identified outflow candidates among approximately 40,000 GAMA galaxies by searching for two-component features in the [O III]$\lambda\lambda$4959, 5007 doublet emission lines (Salehirad et al., 2025). Notably, I detected outflows in low-mass galaxies, with faster AGN-driven outflows than those in star-forming (SF) objects. These findings underscore the significance of AGN feedback in these objects and provide observational

benchmarks for theoretical models.

Finally, in Chapter 4, I summarize my findings and offer conclusions. I also discuss future directions for research in this field.

9

HUNDREDS OF LOW-MASS ACTIVE GALAXIES IN THE GALAXY AND MASS ASSEMBLY (GAMA) SURVEY

Contribution of Authors and Co-Authors

Manuscript in Chapter 2

Author: Sheyda Salehirad

Contributions: Analyzed the data, visualized the data, and wrote the manuscript.

Co-Author: Amy E. Reines

Contributions: Provided feedback on the results, edited and provided comments on the manuscript.

Co-Author: Mallory Molina

Contributions: Edited and provided comments on the manuscript.

Manuscript Information

Sheyda Salehirad, Amy Reines, Mallory Molina

The Astrophysical Journal

Status of Manuscript:
____ Prepared for submission to a peer-reviewed journal
____ Officially submitted to a peer-reviewed journal
____ Accepted by a peer-reviewed journal
_X_ Published in a peer-reviewed journal

IOP Publishing
The Astrophysical Journal, Volume 937, Number 1
DOI: 10.3847/1538-4357/ac8876

Introduction

Supermassive black holes (BHs) are found in the nuclei of almost all massive galaxies (e.g. Kormendy & Ho, 2013; Kormendy & Richstone, 1995), however the "memory" of BH seeding is erased during merger-driven growth over cosmic time (e.g. Natarajan, 2014; Volonteri, 2010). The current proposed seeding models include remnants of Population III stars (e.g., Bromm & Yoshida, 2011), direct collapse scenarios (e.g., Begelman et al., 2006; Lodato & Natarajan, 2006; Loeb & Rasio, 1994), and runaway collisions in dense star clusters (e.g., Devecchi & Volonteri, 2009; Miller & Davies, 2012; Portegies Zwart et al., 2004). These models result in different BH seed masses; the remnants of Population III stars would create seeds with $M_{\rm BH} \sim 100\ M_{\odot}$, while stellar collisions and direct collapse would create BHs with $M_{\rm BH} \sim 10^3$–$10^5\ M_{\odot}$.

While the early BH seeds at high redshift are too faint to be detected with current facilities (e.g. Schleicher, 2018; Vito et al., 2018; Volonteri & Reines, 2016), lower-mass galaxies, especially nearby dwarf galaxies, that harbor massive BHs can constrain BH seed models (see Greene et al., 2020; Reines, 2022, for reviews). The relatively quiet merger history of dwarf galaxies (Bellovary et al., 2011) as well as supernova feedback that may stunt BH growth (Anglés-Alcázar et al., 2017; Habouzit et al., 2017) can leave their BH masses close to their initial seed mass. Finding and studying BHs in dwarf galaxies is also important for understanding the role of both negative (Manzano-King et al., 2019) and positive (Schutte & Reines, 2022) AGN feedback in the low-mass regime.

There are multiple ways to search for BHs in the form of active galactic nuclei (AGNs; see Ho, 2008; Kewley et al., 2019, for a review). In the optical regime, narrow-line ratio diagnostic diagrams (e.g., Baldwin et al., 1981; Shirazi & Brinchmann, 2012) that differentiate between star forming (SF) and AGN ionizing spectral energy distributions (SEDs) have been employed to identify AGN activity in lower-mass and dwarf galaxies (e.g.,

Baldassare et al., 2016; Moran et al., 2014; Reines et al., 2013; Sartori et al., 2015). Moreover, detection of broad Hα emission (Chilingarian et al., 2018; Dong et al., 2012; Greene & Ho, 2004, 2007; Reines et al., 2013) can be indicative of the presence of dense gas in the broad line region (BLR) around a BH, thus suggestive of AGN activity in galaxies. High-ionization coronal emission lines, such as [Fe X]λ6374 and [Ne V]λ3426, can also be produced in the presence of massive BHs, thus an indicator of AGN activity (e.g., Cerqueira-Campos et al., 2021; Gilli et al., 2010; Goulding & Alexander, 2009; Molina et al., 2021a,b; Penston et al., 1984; Prieto et al., 2002; Satyapal et al., 2008; Schmidt et al., 1998).

There are selection biases associated with each AGN diagnostic, which results in the selection of different populations of galaxies. The narrow-line diagnostic diagrams typically observe high-accretion rate AGNs (Greene et al., 2020) and struggle with identifying low ionization nuclear emission regions (LINERs), low-luminosity AGNs (LLAGNs), and shock activity (Ho, 2008; Kewley et al., 2019; Molina et al., 2018). This leaves a significant portion of lower-mass galaxies with lower accretion rates unexplored. Moreover, the radiation from the host galaxy can obscure AGN activity in SF galaxies (Cann et al., 2019; Groves et al., 2006; Moran et al., 2002; Stasińska et al., 2006). Thus, it is crucial to conduct searches for AGN activity that can minimize these effects and probe different populations of lower-mass galaxies.

In this paper, we present a spectroscopic search for BH activity in low-mass galaxies utilizing data from the Galaxy And Mass Assembly (GAMA) survey Data Release 4 (DR4; Driver et al., 2022; Liske et al., 2015). We analyze the spectra and search for AGN signatures in galaxies with stellar masses $M_\star \leq 10^{10} M_\odot$ and redshifts $z \leq 0.3$. Given that the GAMA spectroscopic survey covers different sky regions and is approximately two magnitudes deeper than the Sloan Digital Sky Survey (SDSS) spectroscopic survey (York et al., 2000), where most previous optical searches have been conducted (e.g., Greene & Ho, 2007; Moran et al., 2014; Reines et al., 2013), we aim to find novel AGN candidates in this stellar mass range.

We proceed by employing four AGN diagnostics, including two narrow-line diagnostic diagrams ([O III]/Hβ vs. [N II]/Hα and He II/Hβ vs. [N II]/Hα), as well as searching for the [Fe X]λ6374 and [Ne V]λ3426 high-ionization coronal emission lines. This multiple diagnostic approach allows us to perform a more comprehensive search for AGN activity in this low-mass range, and thus potentially identify massive BHs from different populations of galaxies (e.g. in terms of their masses and colors). We explain the data and our sample selection process in section 2 and the analysis of the GAMA spectra in section 3. The results of each emission-line diagnostic and the host galaxy properties are included in sections 4 and 5, respectively. A summary and conclusions are presented in section 6. Here we assume a ΛCDM cosmology with $\Omega_m = 0.3$, $\Omega_\Lambda = 0.7$ and $H_0 = 70$ km s^{-1} Mpc^{-1}.

Data and Parent Sample of Low-Mass Galaxies

The GAMA Survey

The GAMA Survey includes optical spectroscopy taken with the AAOmega multi-object spectrograph on the 3.9 m Angelo-Australian Telescope (AAT; Saunders et al., 2004; Sharp et al., 2006; Smith et al., 2004). The spectrograph is equipped with a dual-beam setup that covers the wavelength range of 3730–8850 Å with a dichroic split at 5700 Å. The spectral resolution of the blue and red arms are 3.5 and 5.3 Å, respectively, and the spectroscopic fibers are 2 arcsec in diameter. In this work, we utilize spectra and stellar masses released in GAMA DR4 covering three equatorial 60 deg^2 regions (G09, G12 and G15) and two southern $\sim$ 50 deg^2 regions (G02 and G23). The combined limiting magnitude for the main survey objects in the equatorial and G23 regions is $r < 19.65$ mag and the G02 region has a limiting magnitude of $r < 19.8$ mag (Baldry et al., 2018; Driver et al., 2022).

Parent Sample

The GAMA database is stored in tables organized into data management units (DMUs)[1]. The current GAMA spectra are provided in the `AATSpecAll v27` table in the `SpecCat` DMU (Liske et al., 2015). We only use spectra with redshift estimates that are correct by the probability of at least 95%. Additionally, if multiple GAMA spectra are matched to a single GAMA object, we use the spectrum that provides the best redshift for that object. We also exclude problematic spectra such as those that are affected by fringing and bad splicing.

To select our parent sample of low-mass galaxies, we impose a stellar mass cut of $M_\star \leq 10^{10} M_\odot$ using galaxy stellar masses provided by GAMA, which are stored in the `StellarMasses` DMU (Taylor et al., 2011). Stellar masses are obtained from stellar population fits to multiband SEDs. We utilize the mass estimates in the `StellarMassesGKV v24` table (Driver et al., 2022) for the equatorial and G23 survey regions, which uses matched-segment photometry across all bands derived from the Kilo-Degree Survey (KiDS; Kuijken et al., 2019) and the Visible and Infrared Survey Telescope for Astronomy Kilo-degree Infrared Galaxy Public Survey (VIKING; Edge et al., 2013). Stellar masses for galaxies in the G02 survey region are provided in the `StellarMassesG02CFHTLS v24` and `StellarMassesG02SDSS v24` tables, which are based on multi-band SED fitting to Canada-France-Hawaii Telescope Lensing (CFHTLenS; Heymans et al., 2012) and SDSS photometry, respectively. We utilize the mass estimates given in the `StellarMassesG02CFHTLS v24` table, but use the `StellarMassesG02SDSS v24` table to remove galaxies with masses that are different by at least 0.3 dex in both tables. Finally, we apply the mass constraint of $10^5 \leq M_* \leq 10^{10} M_\odot$, which results in 52,782 objects.

In addition to the stellar mass constraint, we also employ signal-to-noise (S/N) cuts

[1] `http://www.gama-survey.org/dr4/schema/`

using emission line measurements provided by GAMA. In particular, we use the Gaussian-fit, emission-line fluxes and equivalent widths (EWs) from the `GaussFitSimple v05` table from the `SpecLineSFR` DMU (Gordon et al., 2017). Following the Reines et al. (2013) methodology, we impose the following requirements: the Hα, [O III] λ5007 and [N II] λ6583 lines must have S/N ≥ 3 and EW > 1 Å, and Hβ must have S/N ≥ 2. We also only include the objects with redshifts $z \leq 0.3$ to ensure the [S II] doublet is in the observed wavelength range. This leaves us with a parent sample consisting of 23,460 galaxies.

Analysis of the GAMA Spectra

In this work, we use a variety of optical emission line diagnostics to search for AGN activity in our parent sample of low-mass emission-line galaxies. While we use the GAMA flux measurements to help define our parent sample, we create custom code to carry out our spectral analysis and search for AGN signatures. This includes fitting and subtracting the stellar continuum, separating broad and narrow Hα and Hβ components, and fitting various other emission lines. All of our custom code is written in the `Python` programming language[2].

Stellar Continuum Subtraction

The stellar continuum, which significantly contributes to the observed spectra of the galaxies in our parent sample, needs to be removed before we can search for emission-line signatures of AGNs. Stellar light will generally contain absorption features and it is especially important to model and remove Balmer absorption lines when searching for broad Hα or Hβ emission that could signify dense gas orbiting a massive BH.

We use the publicly available package `pPXF` (Cappellari, 2017) to find the best fit stellar continuum model for each spectrum. We use the Bruzual & Charlot (2003) SSP models in

[2] `https://www.python.org/`

the wavelength range of 3350 to 8850 Å with spectral resolution of 3 Å, which are calculated for 3 different metallicities (Z = 0.008, 0.02, 0.05) and 10 different ages (t = 0.005, 0.025, 0.1, 0.29, 0.64, 0.9, 1.4, 2.5, 5, and 11 Gyr). We model each spectrum with a combination of single-metallicity SSP models, modified by a low-order multiplicative polynomial to account for reddening by dust. This method yields acceptable continuum models as well as plausible velocity dispersions by `pPXF` for the majority of the objects in our sample. However, if the velocity dispersion is unrealistically large (200–1000 km/s), we refit the continuum including additive polynomials, which can change absorption line strengths and thereby help minimize template mismatch (Cappellari, 2017). This was the case for 95 objects. We select the model metallicity with the smallest χ^2 value. The majority of the galaxies in our sample ($\sim$ 72%) are best fitted by the sub-solar metallicity model (Z = 0.008). This is consistent with previous studies that show low-mass galaxies generally have low metallicities (e.g., Tremonti et al., 2004). Since our primary goal is to measure the emission lines, we attempt good fits to the stellar continua but do not fully explore the parameter space. An example of a fitted galaxy spectrum is shown in the top panel of Figure 3. In the end, we subtract the best-fit model from the data to achieve a pure emission-line spectrum.

Emission Line Measurements

We use the `LMFIT` package in python (Newville et al., 2014) to model the emission lines with Gaussians. For each spectral region that we fit, we also include a linear component in the model to account for uncertainties associated with the initial stellar continuum fit. Examples of fitted emission lines are shown in the bottom panel of Figure 3.

Following the methodology in Reines et al. (2013) and references therein, we first fit the [S II]$\lambda\lambda$6716,6731 doublet with single Gaussian models for each line in the doublet. We assume equal widths for the lines (in velocity space) and hold their relative laboratory wavelengths fixed. We then fit each line in the [S II] doublet with a two-component Gaussian

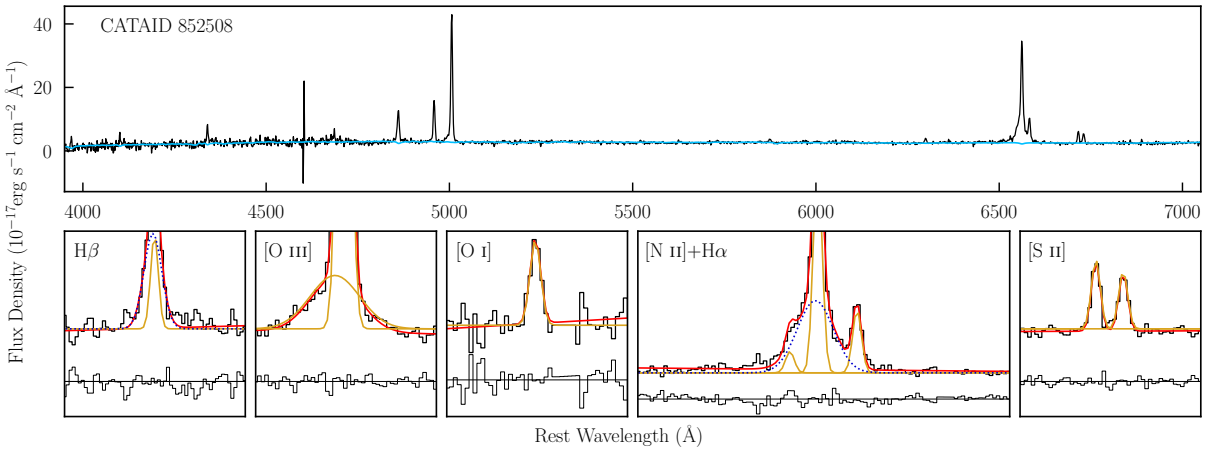

Figure 3: An example of a redshift-corrected spectrum (top panel) for a broad-line AGN in our sample with chunks showing various emission-lines (bottom panels). This galaxy has CATAID 852508 and is among the [N II]/Hα-selected AGN candidates that also has broad Hα emission. In the top panel, we show the observed spectrum in black and the best-fit continuum + absorption line model in blue. In the bottom panels, we plot chunks of the emission-line spectra in black, the best fitting total model (Gaussian emission-line model + local linear continuum model) in red, and the individual Gaussian components in gold. The Gaussian broad Hα and Hβ components are plotted in dotted dark blue.

model. In this case, we additionally constrain the relative heights, widths and positions of the two components to be the same for both lines. We adopt the two-component Gaussian model if the reduced χ^2 is at least 20% lower than that of the single Gaussian model. Only 15 galaxies meet this criterion and require a two-component Gaussian model for the narrow line profile.

We then fit the [N II]$\lambda\lambda$6548,6583 doublet and narrow Hα line based on the parameters from the [S II] emission-line model, as the [N II] and narrow Hα line profiles are well-matched to the [S II] lines (Filippenko & Sargent, 1988, 1989; Greene & Ho, 2004; Ho et al., 1997). The relative separation between the [N II] lines is held fixed using their laboratory wavelengths and the flux ratio of [N II]λ6583/[N II]λ6548 is set to the theoretical value of 2.96. We fix the width of the lines in the [N II] doublet (in velocity space) to that of the [S II] lines, but let the width of the narrow Hα line increase by as much as 25%. We scale the two-component [S II] parameters for the 15 galaxies with two-component [S II] models to fit the narrow-line emission of the [N II] and Hα group. The [N II]+Hα complex is then fitted a second time with an additional broad Hα component. If the computed reduced χ^2 value is at least 20% less than that of the narrow-line model, and the full-width at half maximum (FWHM) of the broad Hα line is at least 500 km s^{-1} after correcting for the fiber-dependant instrumental resolution, we select the model with broad Hα component. We fit the Hβ line using the same method as the Hα line.

We also model the [O III]λ5007 and [O I]λ6300 emission lines. Since the [O III] line normally shows a broad, blue shoulder (e.g. Heckman et al., 1981; Whittle, 1985) and does not match the other line profiles (Greene & Ho, 2005), we use an independent Gaussian model for the fitting process. We also need independent [O I] model to accurately model the [Fe X] line, which is discussed below. We fit the [O III] and [O I] lines with one- and two-Gaussian models, and accept the two-component model if the measured reduced χ^2 is lowered by at least 20%.

We follow the methodology described in Molina et al. (2021b) to fit the [Fe X]λ6374 line, which allows us to detect [Fe X] even if it is blended with the [O I]λ6363 line. We use the model parameters of the fitted [O I]λ6300 line to describe the [O I]λ6363 line. Specifically, we shift the model using the laboratory line wavelengths, assume the same width in velocity, and keep the flux ratios of [O I]λ6300/[O I]λ6363 = 3. We also add a linear fit to the continuum in this spectral region. Finally, we subtract the [O I]λ6363 Gaussian component and the linear fit so we are left only with a potential [Fe X] line, which we fit with a single Gaussian model.

We also search for He II λ4686 and [Ne V]λ3426 lines and fit a single Gaussian model to each line. Given the observed wavelength range of the GAMA survey, we only search for [Ne V] emission in galaxies with redshift $z \geq 0.15$.

We use the parameters from the Gaussian models to calculate the emission-line fluxes. We consider a line detected if the flux has a S/N $\geq$ 3. In addition to the flux requirement, we require the line peak to be at least 3σ above the noise for the relatively weak He IIλ4686, [O I]λ6300, [Fe X]λ6374, and [Ne V]λ3426 lines, where the noise is determined as the root mean square (rms) of the continuum windows around the lines. Finally, we visually inspect the AGN candidates that are flagged by our automated code and remove those that have spectra with missing pixel values within the emission lines, those affected by bad splicing or fringing, and those with bad fits to emission lines (e.g., noise or broad fits to the continuum). Given that the [N II] and Hα lines are fitted based on the [S II] model parameters, a good fit the to the [S II] lines is needed. However, if the flagged AGN candidates have strong [N II] and Hα detections, despite unreliable [S II] detection, we keep them as potential AGN candidates in our final sample.

AGN Selection

In this work, we search for various optical spectroscopic indicators of AGN activity using the emission line measurements described above. In order to provide a comprehensive search for AGN activity, we employ four different AGN diagnostics that we consider to be relatively robust in the low-mass regime. These include the [O III]/Hβ vs. [N II]/Hα and He II/Hβ vs. [N II]/Hα 2D narrow emission line ratio diagrams (Baldwin et al., 1981; Shirazi & Brinchmann, 2012), as well as searching for [Fe X] and [Ne V] and coronal-line emission (Gilli et al., 2010; Molina et al., 2021b; Schmidt et al., 1998). We also search for broad Hα emission (e.g., Chilingarian et al., 2018; Greene & Ho, 2005; Reines et al., 2013) in our parent sample, but only include the broad-line AGN candidates that overlap with other AGN diagnostics in this work since broad Hα can also be produced by transient stellar phenomena (e.g., Type II supernovae, in star-forming galaxies with low masses; Baldassare et al. 2016). We describe each of the four AGN diagnostics below, and present the results of applying each diagnostic to our parent sample of low-mass emission-line galaxies (also see Figure 4). The galaxy properties of the AGN candidates and their respective emission-line flux measurements are listed in Tables 1 and 2, respectively.

[O III]/Hβ vs. [N II]/Hα

The photoionizing continuum from an AGN contains a larger fraction of high-energy photons relative to hot stars, which results in extended partially ionized regions in AGNs. In these regions, lines such as [N II]λ6583, [S II]$\lambda\lambda$6716,6731, and [O I]λ6300 are produced by collisional excitation. This results in larger intensities of these lines with respect to Hα in the narrow-line emission from AGNs than in H II regions, which allows them to be separated in emission-line diagnostic diagrams.

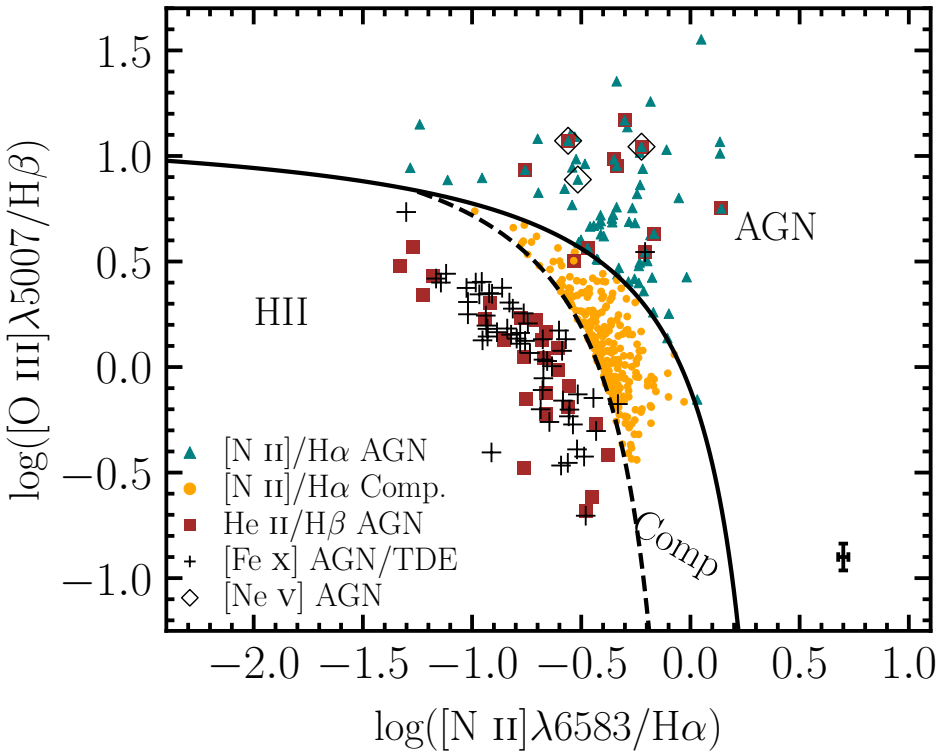

Figure 4: The [O III]/Hβ vs. [N II]/Hα diagnostic diagram (Baldwin et al., 1981) for all 388 AGN candidates found in this work. The [N II]/Hα AGNs and Composites are shown as teal triangles and orange circles, respectively, while the He II/Hβ AGNs are shown as brown squares and [Fe X]-selected AGNs as black pluses. The [Ne V]-AGNs are added as unfilled back diamonds. Eleven of the He II-selected AGNs, 2 of the [Fe X]-selected AGNs, and all 3 of the [Ne V]-selected AGNs overlap with the [N II]/Hα AGNs/Composites.

Table 1: AGNs in Low-mass Galaxies

CATAID	RA	DEC	z	log ($M_*/M_\odot$)	M_g	$g-r$	[N II]/Hα location	He II/Hβ location	[Fe X]λ6374 Detection	[Ne V]λ3426 Detection
(1)	(2)	(3)	(4)	(5)	(6)	(7)	(8)	(9)	(10)	(11)
2273067	30.26775	-4.17022	0.18946	9.95	-20.20	0.42	Comp.	...	...	...
1460491	30.47504	-7.00111	0.04907	9.43	-18.50	0.47	Comp.	...	...	...
1459023	30.57854	-7.08115	0.08646	9.60	-18.89	0.49	AGN	...	...	...
1555169	30.60408	-4.99215	0.19842	9.95	-20.34	0.42	AGN	...	...	...
2258819	30.87408	-9.49147	0.25170	9.60	-20.66	0.27	AGN	...	...	...
1379310	31.24338	-8.49599	0.11249	9.96	-20.44	0.40	Comp.	...	...	...
1366459	31.42363	-7.52362	0.13715	9.49	-19.12	0.39	SF	...	Detected	...
1431173	31.50662	-5.06840	0.29580	9.71	-20.70	0.24	AGN	...	...	...
2229220	31.53125	-5.62439	0.24479	9.90	-20.58	0.31	SF	AGN	...	...
1434726	31.77417	-4.82812	0.28103	9.99	-20.88	0.33	Comp.	...	...	...

Note—Galaxy properties for the low-mass AGNs. The values given in columns 1-7 are obtained from GAMA DR4 and assume $h = 0.7$. Column 1: Unique ID of the GAMA object. Columns 2–3: The right ascension and declination (in degrees) of the spectrum (J2000). Column 4: Redshift. Columns 5–7: The log galaxy stellar mass in units of $M_\odot$, absolute $g-$band magnitude, and $g-r$ color. All values are obtained from the `StellarMassesG02CFHTLS v24` and `StellarMassesGKV v24` tables (Bellstedt et al., 2020; Taylor et al., 2011). Columns 8–9: Our classifications of the galaxy in each of the narrow-line diagnostic diagrams. Columns 10–11: The [Fe X] and [Ne V] coronal line detections in this work. A three-dot ellipsis indicates that no line is detected. The entirety of Table 1 is published in the electronic edition of *The Astrophysical Journal*. We show a portion here to give information on its form and content.

Table 2: Emission-line Fluxes

CATAID (1)	[Ne V]λ3426 (2)	He IIλ4686 (3)	(Hβ)$_n$ (4)	(Hβ)$_b$ (5)	[O III]λ5007 (6)	[O I]λ6300 (7)	[Fe X]λ6374 (8)	(Hα)$_n$ (9)	(Hα)$_b$ (10)	[N II]λ6583 (11)	[S II]λ6716 (12)	[S II]λ6731 (13)
2273067	...	...	41(6)	...	160(3)	18(2)	...	214(6)	...	37(4)	43(3)	37(3)
1460491	...	...	85(25)	...	142(23)	...	...	325(16)	...	117(13)	116(17)	96(17)
1459023	...	...	87(7)	...	156(7)	...	...	303(4)	...	241(3)	105(5)	55(5)
1555169	...	...	6(7)	71(10)	27(3)	...	...	196(4)	...	68(3)	38(2)	23(2)
2258819	...	...	4(1)	42(3)	53(2)	...	...	32(2)	196(4)	17(1)	...	...
1379310	...	...	272(6)	...	238(8)	53(3)	...	1356(8)	...	616(6)	223(4)	182(4)
1366459	...	...	33(3)	...	18(2)	...	24(3)	110(3)	...	25(2)	30(3)	10(3)
1431173	...	...	27(2)	...	209(3)	...	...	186(3)	...	21(2)	26(4)	22(4)
2229220	...	38(4)	32(3)	...	26(3)	...	...	119(3)	...	33(3)	17(4)	19(4)
1434726	...	...	36(4)	...	54(3)	...	...	173(5)	...	73(4)	32(5)	26(5)

Note—Measured emission line fluxes for our sample of low-mass AGNs. Column 1: Unique ID of the GAMA object. Columns 2–13: The emission-line fluxes in units of 10^{-17} erg s^{-1} cm^{-2} with the errors shown in parentheses. No extinction correction has been applied. The subscripts n and b refer to the narrow and broad components, respectively. We do not show the flux values of the weaker lines [N II] and [O I] doublets, since their fluxes are fixed to be weaker by factors of 2.96 and 3, respectively. A three-dot ellipsis indicates that no line is detected. The entirety of Table 2 is published in the electronic edition of *The Astrophysical Journal*. We show a portion here to give information on its form and content.

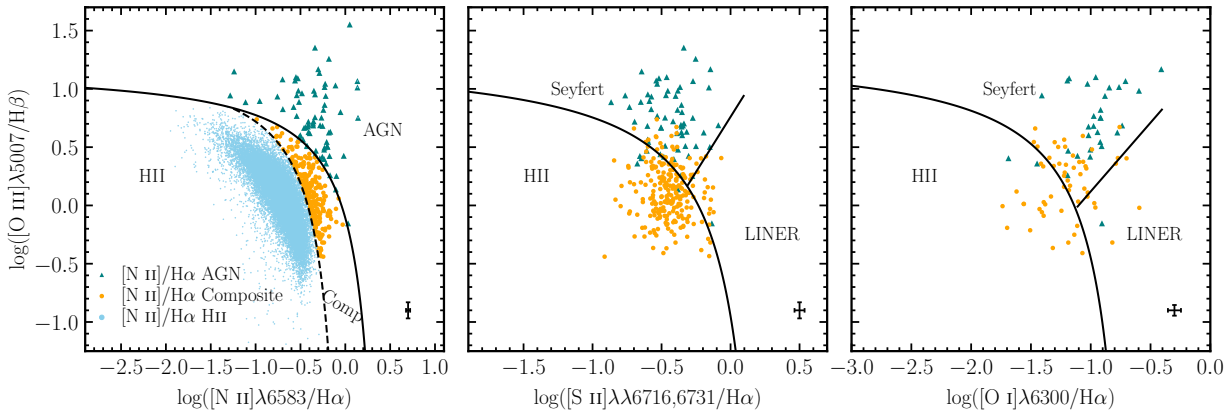

Figure 5: The [O III]/Hβ vs. [N II]/Hα narrow-line diagnostic diagram (left panel) for galaxies with stellar masses $M_\star \leq 10^{10} M_\odot$ in the GAMA survey using the classification scheme summarized in Kewley et al. (2006). We show the 71 AGN and 238 composite galaxies as teal triangles and orange circles, respectively, and those consistent with star-forming galaxies as sky blue points. The middle and right panels show the AGN and composite objects in the [O III]/Hβ vs. [S II]/Hα and [O I]/Hα diagrams. Only AGN candidates with reliable [S II] and/or [O I] detection are plotted in the middle and right panels. Characteristic error bars are located in the lower right region of each panel. See Section 4.1 for details.

The [O III]/Hβ vs. [N II]/Hα diagnostic diagram (Baldwin et al., 1981) has been widely used to separate SF galaxies from AGN-dominated ones. This diagram is metallicity sensitive, with SF galaxies varying in abundance from low metallicity (low [N II]/Hα ratio, high [O III]/Hβ ratio) to high metallicity (high [N II]/Hα ratio, low [O III]/Hβ ratio), while shocks and AGN-dominated galaxies generally have higher ratios of [O III]/Hβ and [N II]/Hα. This results in a clear separation between SF galaxies and those with an AGN contribution in the general population of galaxies (e.g., Kewley et al., 2019). However, this diagnostic diagram can struggle with identifying AGNs in low-mass galaxies, which tend to have lower metallicities than more massive ones. In other words, low-metallicity AGNs overlap with low-metallicity starbursts in this diagram (Groves et al., 2006) and so these AGNs may be missed. Nevertheless, this diagram appears to be robust at identifying bona-fide AGNs in the low-mass regime (Baldassare et al., 2017; Reines et al., 2013).

We employ this diagram as our first AGN indicator as shown in the left panel of Figure 5. We use the classification scheme outlined in Kewley et al. (2006), where star-forming/H II galaxies fall below the empirical composite line from Kauffmann et al. (2003), AGN-dominated galaxies fall above the theoretical extreme starburst line from Kewley et al. (2001), and composite galaxies fall in between the two lines. We identify 71 AGNs and 238 composite galaxies in our parent sample by using this diagram.

We also plot these AGN and composite galaxies in the [O III]/Hβ vs. [S II]/Hα and [O I]/Hα diagrams (Veilleux & Osterbrock, 1987) as shown in the middle and right panels of Figure 5. In these diagrams, we use the classification scheme in Kewley et al. (2006) where the star-forming galaxies and the AGN candidates are separated by the theoretical extreme starburst line from Kewley et al. (2001) and the Seyfert-like and LINER-like galaxies by the Seyfert-LINER line. We find that 298/309 and 89/309 of the AGNs and composites have reliable [S II] and [O I] detections (see section 3.2), out of which 39% fall in the AGN region of the [S II]/Hα diagram and 74% are AGN-like in the [O I]/Hα diagram. There are also 47 objects that show AGN activity in all three diagrams. Moreover, some of the AGNs/Composites selected by this diagnostic have additional AGN indicators (see Figure 4 and the following subsections).

He II/Hβ vs. [N II]/Hα

Nebular He II emission has a relatively high ionization potential (54.4 eV) and therefore can also be produced by a hard ionizing spectrum, which may indicate AGN activity. The He II/Hβ vs. [N II]/Hα diagram proposed by Shirazi & Brinchmann (2012) has been used to separate SF galaxies from AGN-dominated ones in dwarf galaxies (Sartori et al., 2015). While He II emission can originate from AGN activity, stellar processes can also produce this line; thus care is needed when using this diagnostic.

We search for He II emission in our parent sample of low-mass galaxies and identify 44

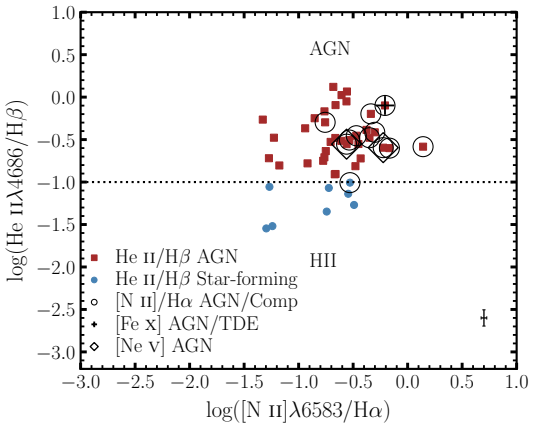

Figure 6: The He II/Hβ vs. [N II]/Hα diagnostic diagram. We apply the criterion log(He II/Hβ)> -1 (see section 4.2) to separate star-forming galaxies from galaxies with AGN activity, which is shown as the black dotted line. 36 out of the 44 galaxies with detectable He II emission in our parent sample fall above this line, which we show as brown squares, while the SF galaxies are shown as steel blue circles. 12 of the galaxies in this sample are also AGNs/Composites in the [N II]/Hα diagnostic, which we indicate with unfilled circles, while 1 AGN is observed with [Fe X] emission and 2 AGNs are also observed with [Ne V] emission, which are plotted as a plus and unfilled black diamonds, respectively. The characteristic error bars are added in the lower right of this diagram.

galaxies with detected emission, out of which 12 overlap with the [N II]/Hα-selected AGNs and composites. We select the He II/Hβ AGN candidates in our sample by employing the criterion proposed in Molina et al. (2021b), log(He II/Hβ)> -1, as shown in Figure 6. This limit is expected to be higher than that produced by X-ray binaries (XRBs) or Wolf-Rayet (WR) stars (Schaerer et al., 2019) and is slightly stricter than the criteria presented in Shirazi & Brinchmann (2012). We find that 36 of the He II-emitting galaxies meet this criterion, out of which 10 are also [N II]/Hα AGNs and 1 is a composite object. The remaining He II-emitting galaxy among the [N II]/Hα-selected composite galaxies, while strictly in the H II part of the diagram, is consistent with a He II-selected AGN within the measurement uncertainties (see Figure 6). One of the He II/Hβ AGNs has [Fe X] emission and 2 have [Ne V] emission (see sections 4.3 and 4.4), all three of which are also [N II]/Hα AGNs. In appendix 1, we show the observed spectra for a selection of these AGN candidates in Figure

13, and the He II emission line fits for all 36 He II/Hβ-selected AGNs in Figure 14.

Given that the majority (25/36) of the He II/Hβ AGN candidates are SF in the [N II]/Hα diagram, we further investigate these systems. First, we visually search for WR features in the spectra (Conti, 1991; Schaerer et al., 1999) such as the blue and red bumps that appear around 4650 Å and 5808 Å. We do not find WR signatures in these galaxies, and thus conclude that either WR stars are not responsible for the observed He II emission or any potential WR signatures are not detectable in the GAMA spectra.

Next, we investigate whether it is possible to have a He II/Hβ-selected AGN that is also SF in the [N II]/Hα diagram by combining a variety of AGN spectra with SF spectra. We begin by linearly adding emission-line fluxes from a well-known AGN in a dwarf galaxy, NGC 4395 (Filippenko & Ho, 2003; Filippenko & Sargent, 1989), to $\sim$ 3000 [N II]/Hα SF galaxies. We select these objects from our parent sample of low-mass galaxies described in section 2.2, and require a S/N $>$ 3 for all the emission lines of interest (Hβ, [O III], [N II], Hα). None of these SF objects have detectable He II emission, and each line of interest is scaled by the ratio of the [O III]λ5007 line for NGC 4395 to that of each SF galaxy by factors of 0.5, 1, and 2 (i.e., a scale factor of 0.5 indicates a lower amount of star formation contribution to the synthesized line ratios). We then linearly add the scaled emission-line fluxes to those of NGC 4395 and plot the resulting emission-line ratios in the He II/Hβ and [O III]/Hβ vs. [N II]/Hα diagrams as shown in the first two columns of Figure 7. None of the constructed line ratios in this test are simultaneously He II/Hβ AGNs and [N II]/Hα SF galaxies. However, if the He II line fluxes were stronger than that of NGC 4395 by at least a factor of 1.2, 1.4, and 2.1 for the scale factors of 0.5, 1, and 2, respectively, there would be galaxies that are both He II/Hβ AGNs and SF in the [N II]/Hα diagram.

In the next test, we employ the same methodology described above, but instead of using the emission-line fluxes from NGC 4395, we use 10 galaxies in our sample that are both [N II]/Hα and He II/Hβ-selected AGNs. In 4/10 of these case studies, we find that

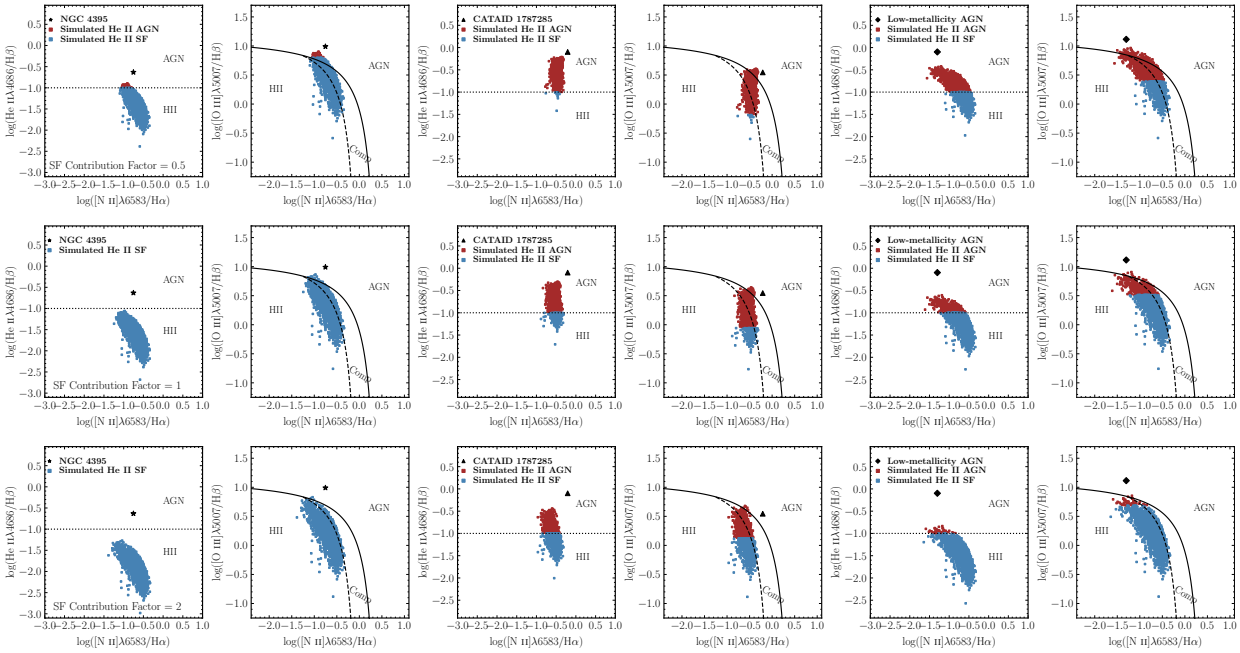

Figure 7: Simulated emission line ratios in the He II/Hβ and [O III]/Hβ vs. [N II]/Hα diagrams from various combinations of AGN + SF line fluxes demonstrating that it is possible to have He II-selected AGNs that fall in the SF region of the [N II]/Hα diagram. We show the results using three AGNs: NGC 4395 (first two columns), a He II-selected AGN from this work (CATAID 1787285; middle two columns), and a mock low-metallicity AGN (last two columns). The SF line fluxes are scaled by the ratio of the [O III]λ5007 line for each AGN to each SF galaxy by "SF contribution factors" of 0.5 (first row), 1 (second row), and 2 (third row) before the addition. See Section 4.2 for details.

there are objects that have emission-line ratios that are simultaneously AGN-like in the He II/Hβ diagram and SF in [N II]/Hα diagram. We show an example in the two middle columns of Figure 7. The AGN in this Figure (CATAID 1787285) has an He II/[O III] ratio $\sim$ 10 times higher than NGC 4395. The fraction of objects that are He II/Hβ AGNs and SF in the [N II]/Hα diagram ranges from 15 % to 50 % depending on the SF contribution scale factor. However, we note that there is a continuum of objects reaching up into the composite region of the [N II]/Hα diagram, which is not seen in our sample of He II-selected AGNs (Figure 4). The majority of the He II-selected AGNs in our sample fall in the SF region of the [N II]/Hα diagram, with only 1 composite object and a handful of AGNs. Motivated by this, we next investigate the impact of using a low-metallicity AGN on the simulated line ratios.

We carry out the final test with a mock low-metallicity AGN, setting $\log([\mathrm{N\,II}]/\mathrm{H}\alpha) = -1.3$ and $\log([\mathrm{O\,III}]/\mathrm{H}\beta) = 1.1$. We use the same value of $\log$ He II/H$\beta = -0.1$ as the GAMA object in Figure 7. The simulated AGN+SF line ratios are shown in the last two columns of Figure 7. In this case we again find He II/Hβ AGNs that are SF in the [N II]/Hα diagram for all the SF contribution scale factors.

The results given above indicate that factors such as metallicity, star formation versus AGN contribution, and the He II/[O III] ratio can impact where objects fall in the diagnostic diagrams. While this exercise has demonstrated that is certainly possible, and perhaps likely, that the detected He II emission in this work is driven by AGN activity, follow-up observations would be useful to confirm these He II-selected AGNs that are SF in the [N II]/Hα diagram.

[Fe X]λ6374 Coronal Line Emission

The presence of [Fe X]λ6374 emission with high ionization potential (262.1 eV; Oetken, 1977) can be indicative of AGN activity in galaxies (e.g., Cerqueira-Campos et al., 2021; Goulding & Alexander, 2009; Penston et al., 1984; Prieto et al., 2002; Satyapal et al., 2008).

Recent studies presented in Kimbro et al. (2021) and Molina et al. (2021a) also confirmed the existence of [Fe X]λ6374 line from accreting BHs in dwarf galaxies. We note that, however, this line is usually weak and thus hard to detect.

We search for the [Fe X]λ6374 line in our parent sample of galaxies and identify 56 reliable detections, out of which 1 overlaps with the [N II]/Hα-selected AGNs and 1 is a composite object. Moreover, the [N II]/Hα-selected AGN is also among the He II/Hβ AGNs. We show the observed spectra for a selection of these objects in Figure 15 and the [Fe X] and [O I] doublet emission-line fits for all 56 galaxies in Figure 16 in appendix 1. The luminosity of the [Fe X] lines in our sample span a range of $\sim 10^{38}-10^{41}$ erg s^{-1}, with a median of $10^{39.6}$ erg s^{-1}. Given these luminosities, there are two main sources that could explain the observed [Fe X] emission: AGNs or tidal disruption events (TDEs), which is where a massive BH tidally disrupts a star. AGN activity can produce the [Fe X] line as a result of gas photoionized by the AGN continuum (e.g., Negus et al., 2021; Nussbaumer & Osterbrock, 1970; Pier & Voit, 1995), or radiative shock waves emitted by radio jets from the AGN (e.g., Molina et al., 2021a; Wilson & Raymond, 1999). A class of tidal disruption events (TDEs) called extreme coronal line emitters (ECLEs) also produce coronal-line emission with $L_{[FeX]} \sim 10^{38-40}$ erg s^{-1} (Komossa et al., 2008; Wang et al., 2012, 2011).

Other potential origins of [Fe X] emission are discussed in Molina et al. (2021b), but these all fail to explain the high luminosities observed here. For example, supernovae rarely produce coronal lines and their luminosities are generally orders of magnitude lower than those observed in our sample. Even one of the most extreme examples, SN 2005ip, had a peak [Fe X]λ6374 luminosity of just 2×10^{37} erg s^{-1} (Smith et al., 2009). Therefore, we conclude that the observed [Fe X] emission in our sample of low-mass galaxies is indicative of AGN activity or tidal disruption events (TDEs), both of which require the presence of a massive BH.

[Ne V]λ3426 Coronal Line Emission

The presence of coronal lines with high ionization energies such as [Ne V]λ3426 ($\sim$ 97 eV) are generally considered strong indicators of AGN activity (Gilli et al., 2010; Schmidt et al., 1998). However, this line has also been found in star-forming galaxies (Izotov et al., 2004), and it is generally weak and hard to detect.

We search for [Ne V] emission in our parent sample of low-mass galaxies and identify 5 galaxies with such emission. However, we cut 2 of the objects with marginal [Ne V] detections and spectra that do not show any other AGN signatures. The remaining 3 [Ne V]-emitting galaxies are [N II]/Hα AGNs, 2 of which are also He II/Hβ-selected AGN candidates. We show the observed spectra as well as the [Ne V] emission-line fits for these galaxies in Figure 8. The luminosities of the [Ne V] lines are in the range of $10^{40.9-41.4}$ erg s^{-1}.

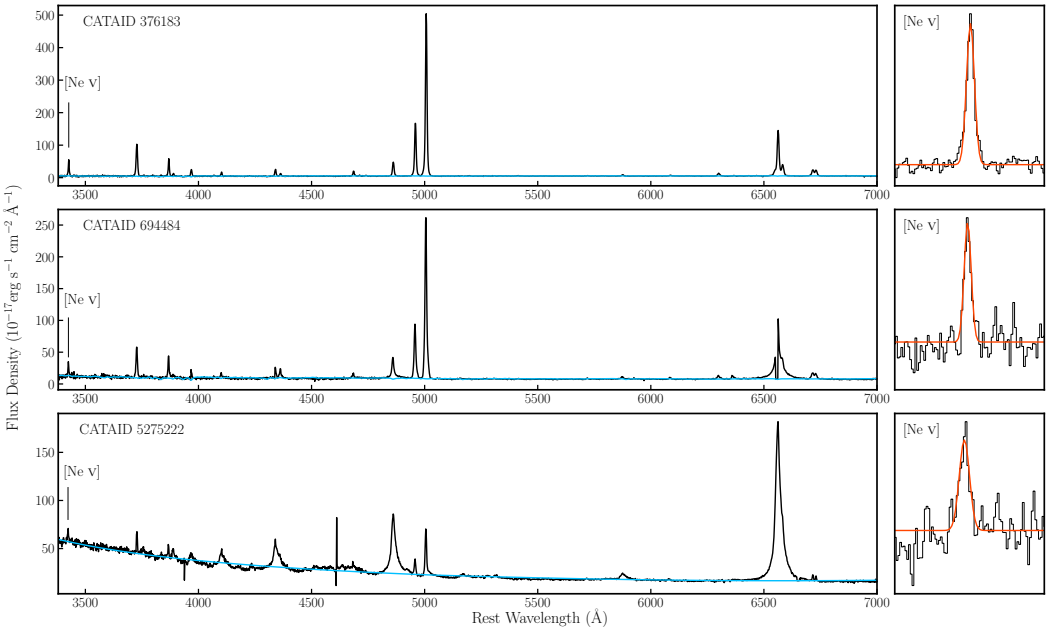

Figure 8: Redshift-corrected spectra and chunks showing [Ne V]λ3426 emission for the 3 strong [Ne V]-emitting galaxies in this work. Here we plot the best-fitting continuum model and individual Gaussian component as sky blue and orange-red, respectively. These galaxies are also [N II]/Hα AGNs and 2 of them (CATAIDs 376183 and 694484) are He II/Hβ AGNs. See section 4.4 for details.

Broad Hα Emission and Black Hole Masses

Dense gas orbiting in the vicinity of a BH can produce broad-line emission, such as broad Hα, and can be used to estimate the mass of the central BH (Greene & Ho, 2005). However, in low-mass galaxies, broad Hα emission from stellar-processes such as supernovae can mimic that of an AGN. Thus, transient broad Hα emission that disappears over time likely indicates a supernova origin, whereas persistent broad Hα favors an AGN origin (e.g., Baldassare et al., 2016).

We search for broad Hα emission in our parent sample of low-mass galaxies and identify 103 galaxies with such emission. As shown in Figure 9, 47 of these galaxies are in our [N II]/Hα-selected AGN and composite sub-sample. Additionally, 7 of these 47 objects show additional AGN-like signatures: 6 are also He II-selected AGNs, 1 has observed [Ne V] emission, and 1 is both a He II-selected AGN and has detectable [Fe X] emission, while 1 of the 47 galaxies is SF in the He II/Hβ diagram. There is also one broad-line AGN candidate that is consistent with SF in the [N II]/Hα and He II/Hβ diagrams. The remaining galaxies do not overlap with any of the diagnostics we employ in this work.

The broad Hα luminosities of the broad-line [N II]/Hα-selected AGN candidates range from $10^{39.7} - 10^{42.6}$, with a median luminosity of $10^{40.9}$ erg s^{-1}. The SF galaxies have broad Hα components with lower luminosities that span a range of $10^{39.1-41.6}$, with a median luminosity of $10^{40.3}$ erg s^{-1}. Moreover, the widths (FWHMs) of all the broad Hα components span a range of $\sim$500–3664, with median FWHM of 1490 km s^{-1} for the [N II]/Hα AGNs/Composites and 895 km s^{-1} for the SF galaxies. The distributions of FWHM and luminosity of the broad Hα components are plotted in panels (a) and (b) of Figure 10. Given that the luminosities and FWHMs of the broad Hα lines in the SF galaxies tend to be significantly lower than those of the [N II]/Hα AGNs/Composites, and that many star-forming galaxies with broad Hα are not in fact AGNs (Baldassare et al., 2016), we consider these objects suspect and do not include them in our final sample of AGNs.

We estimate virial BH masses for the 47 broad-line AGNs/Composites using equation 5 in Reines et al. (2013) and our measurements of the luminosity and FWHM of the broad Hα line. The resulting BH masses vary from $10^{5-7.7}$, with a median BH mass of $10^{6.2} M_{\odot}$. We plot the distribution of BH masses in panel (c) of Figure 10. A list of luminosities and FWHMs of the broad Hα components, and the corresponding BH masses, for the AGNs/Composites are given in Table 3. For the sake of completeness, we also estimate BH masses for the SF galaxies with broad Hα. These are in the range of $10^{4.9-7.3}$, with a median of $10^{5.8}$.

The BH masses for the rest of the AGN candidates in this work are unknown. However, if we assume the BH mass-to-total stellar mass relation for AGNs derived in Reines & Volonteri (2015), the BH masses for all of the AGN candidates span a range of $10^{4.3}-10^{6.4}$, with a median BH mass of $10^{6.2}$ $M_{\odot}$.

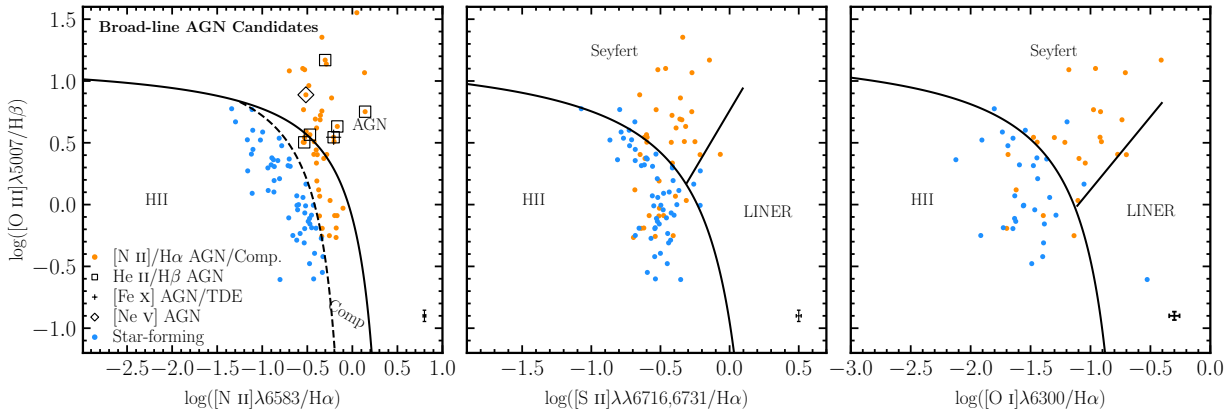

Figure 9: Galaxies with detectable broad Hα emission from our parent sample with stellar masses $M_{\star} \leq 10^{10} M_{\odot}$ in the [O III]/Hβ vs. [N II]/Hα diagram (left panel), [O III]/Hβ vs. [S II]/Hα diagram (middle panel), and [O III]/Hβ vs. [O I]/Hα diagram (right panel). As in Figure 5, we use the classification scheme summarized in Kewley et al. (2006). We find 103 galaxies with broad Hα emission, out of which 47 fall in the AGN/Composite regions of the [N II]/Hα diagram (orange points). Additionally, 6 of these are He II-selected AGNs (black squares), 1 is an [Fe X]-selected AGN (black plus), and 1 is a [Ne V]-selected AGN (black diamond). The broad Hα objects falling the star-forming part of the [N II]/Hα diagram (blue points) do not overlap with any of the narrow-line diagnostics used in this work. Only the objects with reliable [S II] and/or [O I] detections are plotted in the middle and right panels. Characteristic error bars are located in the lower right region of each panel. See section 4.5 for details.

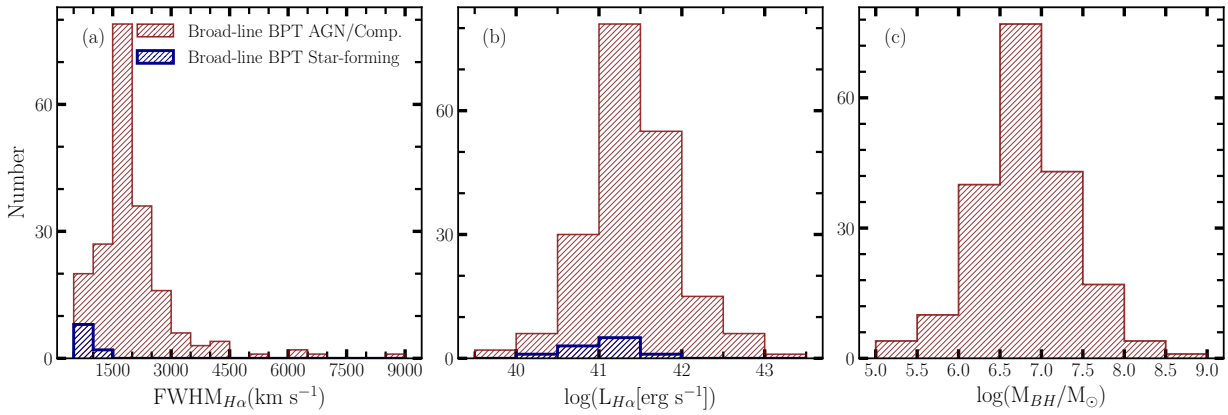

Figure 10: Broad Hα emission. *Panels (a)–(b)*: The distributions of FWHM and log luminosity of the broad Hα components. The [N II]/Hα AGN and composite galaxies are shown as hashed orange histograms, and the star-forming galaxies as blue histograms. See section 4.5 for details. *Panel (c)*: The virial BH mass distribution for the broad-line AGN candidates. We use equation 5 in Reines et al. (2013) to estimate these BH masses. See section 4.5 for details. Note that we do not include the broad-line star-forming objects in our final sample of AGNs.

Sample Properties

Newly-Identified AGNs and Active Fractions

In this work, we identify 388 unique AGN candidates from our parent sample of low-mass galaxies by utilizing two narrow-line diagnostic diagrams (sections 4.1 and 4.2) as well as searching for [Fe X]λ6374 and [Ne V]λ3426 coronal-line emission (sections 4.3 and 4.4). We do not find any matches between our parent sample of galaxies and the AGNs reported in Greene & Ho (2007), Reines et al. (2013), Moran et al. (2014), Chilingarian et al. (2018), and Molina et al. (2021b). In fact, only 2164/23460 galaxies in our parent sample have been observed by other surveys, out of which only 301 have SDSS spectra. Thus, we conclude that this work presents an entirely new sample of AGNs in low-mass galaxies.

Overall we find an active fraction among our parent sample of low-mass emission-line galaxies of 388/23460 $\approx$ 1.7%. Accounting for all of the low-mass galaxies in GAMA

Table 3: Sample of Broad-line AGNs

CATAID (1)	log $L(H\alpha)_b$ (2)	FWHM(Hα)$_b$ (3)	log M_{BH} (4)
[N II]/Hα AGNs			
2258819	41.44	926	6.2
1787285	41.35	889	6.2
346048	40.04	822	5.5
382771	40.70	690	5.6
656596	40.71	723	5.7
3856528	41.47	2247	7.0
3578870	41.17	1041	6.2
852508	41.29	994	6.2
689919	41.85	2160	7.2
273195	40.94	1205	6.2
537437	40.61	1296	6.1
703117	41.88	1778	7.0
696560	42.02	2118	7.3
544030	40.88	1395	6.3
238411	39.85	1582	6.0
320888	40.98	2352	6.9
740319	41.07	2043	6.8
484908	40.80	574	5.5
492449	41.67	1786	6.9
48050	40.07	1628	6.1
5247018	42.40	1642	7.2
5240292	42.46	2206	7.5
5265117	40.09	1442	6.0
5275222	42.63	1543	7.3
5220386	42.48	2670	7.7
[N II]/Hα Composites			
1125779	41.15	1620	6.6
2008726	40.88	699	5.7
1672767	40.74	2100	6.6
1791657	40.43	962	5.8
2123678	39.72	592	5.0
375406	40.84	833	5.9
3901665	41.53	2055	7.0
727091	41.32	2097	6.9
521922	39.81	1656	6.0
609225	40.13	1463	6.0
31941	39.74	721	5.2
98560	40.86	707	5.7
718498	40.94	2355	6.8
296972	40.54	1490	6.2
297773	40.13	1211	5.9
297764	40.24	559	5.2
593724	41.37	1620	6.7
267078	40.25	1550	6.1
62983	40.27	1618	6.2
5197149	41.58	1681	6.8
5337331	41.00	1135	6.2
5266552	41.29	742	6.0

Note—Note—Column 1: Unique ID of the GAMA object. Column 2: The luminosity of the broad Hα component in units of erg s^{-1}. Column 3: The width (FWHM) of the broad Hα component in units of km s^{-1}, corrected for instrumental resolution. Column 4: The virial mass estimate of the BH in units of $M_\odot$ by assuming the broad Hα emission is associated with the BLR. See section 4.5 for more details.

(including those that were cut from our parent sample due to weak/no lines, see §2), the active fraction drops to 388/52782 ≈ 0.7%. The majority of the active galaxies were found as AGNs/composites in the [N II]/Hα diagnostic diagram. These alone give an active fraction of $\sim$ 1.3% among our parent sample of low-mass emission-line galaxies. The active fraction using the He II/Hβ ratio and [Fe X]-emitting galaxies are each $\sim$ 0.2%, and the fraction of detectable [Ne V]-emitting galaxies is just $\sim$ 0.01%. While accurate comparisons to other spectroscopic searches for AGNs in the low-mass regime are complicated by various selection criteria and the differing survey characteristics, the values we find are in approximate agreement with prior work (Molina et al., 2021b; Moran et al., 2014; Polimera et al., 2022; Reines et al., 2013; Sartori et al., 2015).

Host Galaxies

The host galaxies of the AGNs in our sample have an upper mass limit of 10^{10} M$_\odot$ by design, and the lowest-mass galaxies with AGNs in our sample have stellar masses of $\log(M_*/M_\odot) \sim 8$ (see Figure 11). A summary of the host galaxy properties for each sub-sample can be found in Table 4 (also see Figure 11 and Table 1 for individual values). Consistent with previous studies (e.g., Reines et al., 2013), the [N II]/Hα-selected AGNs are predominantly among the higher-mass galaxies, although the minimum galaxy mass in this sub-sample has $\log(M_*/M_\odot) \sim 8.3$. The He II-selected AGNs show a similar trend. In contrast, the [Fe X]-emitting galaxies are more evenly spread out in terms of their stellar mass and tend to be more reflective of the parent sample of low-mass galaxies. The rare [Ne V]-emitting galaxies are exclusively found among higher mass objects with luminous AGNs.

The median total absolute g-band magnitude of our sample is $\langle M_g \rangle = -19.5$ mag. This is very similar to that of the Greene & Ho (2007) sample of broad-line AGNs with BH masses $M_{\rm BH} < 2 \times 10^6\ M_\odot$. Our median g-band magnitude is also $\sim$1 mag more luminous than

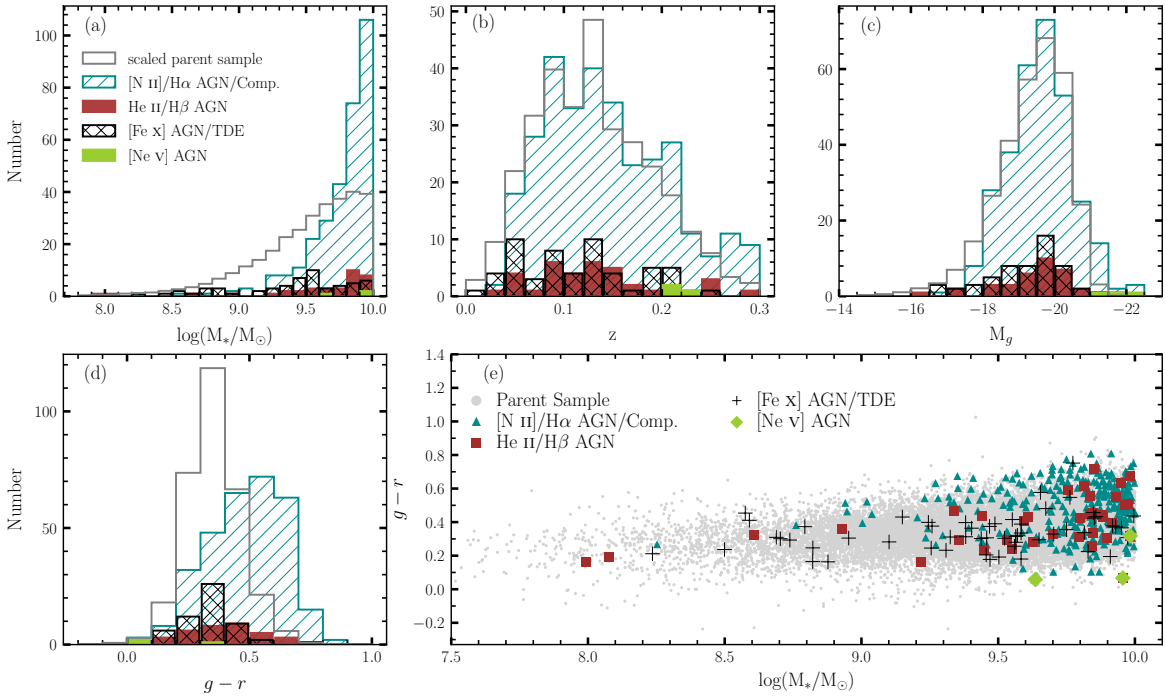

Figure 11: Host galaxy properties. *(a)–(d)*: Distributions of host galaxy stellar mass, redshift, absolute g-band magnitude and $g-r$ color. The [N II]/Hα-selected AGN candidates are shown as hashed teal histograms, the He II/Hβ-selected AGNs are plotted as brown histograms, the [Fe X] AGNs galaxies are shown as cross-hashed black histograms, and the [Ne V]-AGNs are shown as green histograms. Our parent sample of low-mass galaxies is also shown as gray histograms, normalized to the number of [N II]/Hα-selected AGN and composite galaxies. All values are adopted from `StellarMassesG02CFHTLS v24` and `StellarMassesGKV v24` tables (Bellstedt et al., 2020; Taylor et al., 2011). *(e)*: The $g-r$ vs. $\log(M_*/M_\odot)$ plot. Here we use similar color scheme as panels (a)–(d). The [N II]/Hα AGNs/Composites are among redder and more massive objects in our parent sample, which are similar to He II/Hβ AGNs. The [Fe X] AGNs seem to trace the general trend of our parent sample, while the [Ne V] AGNs are among more massive and bluer objects.

what Reines et al. (2013) found for their AGN sample and that of LMC ($M_g^{LMC} \sim -18.2$ mag; Tollerud et al., 2011). This is not surprising given that our upper mass limit is more than 3 times larger than that in the Reines et al. (2013) sample.

A color-mass diagram is shown in panel (e) of Figure 11. The host galaxies of the [N II]/Hα-selected AGN candidates tend to be redder and relatively massive overall, consistent with the findings in Reines et al. (2013). The bias towards redder galaxies selected using the [N II]/Hα diagnostic may be a selection effect, since this diagnostic is metallicity sensitive and struggles with detecting AGNs in low-metallicity star-forming galaxies (e.g., Groves et al., 2006; Kewley et al., 2019; Reines et al., 2013). On the other hand, the galaxies among the He II/Hβ and [Fe X] sub-samples extend to less massive and bluer, thus more star-forming galaxies. Molina et al. (2021b) found a similar trend for [Fe X]-emitting dwarf galaxies in the SDSS. The [Ne V]-emitting sub-sample are among galaxies that are more massive and bluer in our parent sample, characteristic of quasars with strong UV emission from the accretion disk. Given that these objects are powered by relatively low-mass BHs, they may be akin to "miniquasars" that have been proposed as potential contributors to cosmic reionization (Haiman & Loeb, 1998; Madau et al., 2004).

The redshift distributions of the active galaxies in this work, along with that of our parent sample of low-mass galaxies, are shown in panel (b) of Figure 11. The maximum redshift of $z = 0.3$ comes from our requirement of detecting and modeling the narrow-line profile using the [S II]$\lambda\lambda$6716,6731 doublet (§2). Overall, the median redshift of the active galaxies is $z = 0.13$. The [Ne V] line is only within the observable wavelength range for $z \geq 0.15$ and therefore the three [Ne V]-AGNs are at higher redshifts than the other sub-samples (see Table 4). The [Fe X]-selected AGNs/TDEs are at slightly lower redshifts compared to the [N II]/Hα and He II-selected objects, likely owing to the weakness of the [Fe X] line.

Our sample of active galaxies extends to higher redshifts than previous samples in the

low-mass regime based on SDSS spectroscopy. For example, the Reines et al. (2013) dwarf galaxies all have $z < 0.055$, the Moran et al. (2014) sample has $z < 0.018$, Sartori et al. (2015) finds a median redshift of $z \sim 0.03$, and the [Fe X]-selected objects in Molina et al. (2021b) have a median redshift of $z \sim 0.03$. The closest comparisons are to that of the Type 1 AGN sample of Greene & Ho (2007), which has a median redshift of 0.08, and the Type 2 AGN counterparts in Barth et al. (2008) that have $z < 0.08$. The higher redshifts probed by our study are likely due to the fact that the GAMA spectroscopic limiting magnitude is ~ 2 magnitudes deeper than that of the SDSS.

Table 4: Host Galaxy Properties

Diagnostic	$\log(M_*/M_\odot)$			z			M_g			$g-r$		
	min. (1)	max. (2)	med. (3)	min. (4)	max. (5)	med. (6)	min. (7)	max. (8)	med. (9)	min. (10)	max. (11)	med. (12)
[N II]/Hα	8.25	10.00	9.84	0.0277	0.2974	0.1365	-16.58	-22.25	-19.64	0.06	0.81	0.50
He II/Hβ	7.99	9.98	9.81	0.0289	0.2871	0.1289	-16.40	-21.81	-19.64	0.07	0.72	0.40
[Fe X]λ6374	8.24	10.00	9.50	0.0132	0.2421	0.1072	-16.51	-21.30	-19.45	0.16	0.75	0.32
[Ne V]λ3426	9.64	9.98	9.96	0.2095	0.2348	0.2102	-21.09	-22.07	-21.81	0.06	0.32	0.07

Note—Summary of the host galaxy properties of the low-mass AGNs using the four narrow-line diagnostics applied in this work. We show the minimum, maximum, and median values of the host galaxy stellar mass, redshift, g-band absolute magnitude, and $g-r$ color for each of the diagnostics. All the values are adopted from the `StellarMassesG02CFHTLS v24` and `StellarMassesGKV v24` tables (Bellstedt et al., 2020; Taylor et al., 2011). We exclude one of the [N II]/Hα-selected candidates (CATAID 5227891) when calculating these values because it has an erroneous M_g estimate. See section 5.2 for more details.

The Dwarf Galaxy Sample

Searches for AGNs in the low-mass regime often use different criteria for selecting their samples. In some cases, low BH masses are used (e.g., Chilingarian et al., 2018; Greene & Ho, 2007) and in others, absolute magnitude (Barth et al., 2008) or stellar mass limits (e.g., Reines et al., 2013) are used. As described above, our main sample of low-mass active galaxies has an upper stellar mass limit of $10^{10} M_{\odot}$, which has also been used by Moran et al. (2014) and Baldassare et al. (2018). Here we focus on AGNs in the dwarf galaxy mass range, which is usually taken to be $M_{\star} \leq 3 \times 10^{9} M_{\odot}$ (Reines et al., 2013).

As discussed in Section 2, our parent sample of low-mass emission-line galaxies with $M_{\star} \leq 10^{10} M_{\odot}$ consists of 23,460 objects, of which 9,094 are dwarf galaxies with $M_{\star} \leq 3 \times 10^{9} M_{\odot}$. In total, we identify 70 unique dwarf galaxies hosting AGNs based on our diagnostics described in Section 4. We find 9 AGNs and 25 composites using the [N II]/Hα diagram. Two of the dwarf composites also have broad Hα emission and virial BH masses of $\sim 10^{5} M_{\odot}$ and $\sim 7 \times 10^{6} M_{\odot}$. There are 13 dwarf galaxies with detectable He II emission, 9 of which are AGN candidates with high He II/Hβ ratios. We find that 27 of the [Fe X]-emitting galaxies are dwarf galaxies, while none of the [Ne V]-emitting galaxies are in this mass range. We show $grz-$band images of most of the dwarf galaxies in our sample in Figure 12, which we obtained from the DESI Legacy Imaging Survey SkyViewer (Dey et al., 2019).

Summary and Conclusions

In this work, we have systemically searched for optical signatures of active massive BHs in ∼23,000 galaxies with stellar masses $M_{\star} \leq 10^{10} M_{\odot}$ and redshifts $z \leq 0.3$ by analyzing spectroscopic data from GAMA DR4. We employed four optical emission-line diagnostics and identified 388 unique active galaxies, 70 of which are in the dwarf galaxy regime with $10^{8} \leq M_{\star}/M_{\odot} \leq 10^{9.5}$. Our main results are summarized in Figures 4 and 11.

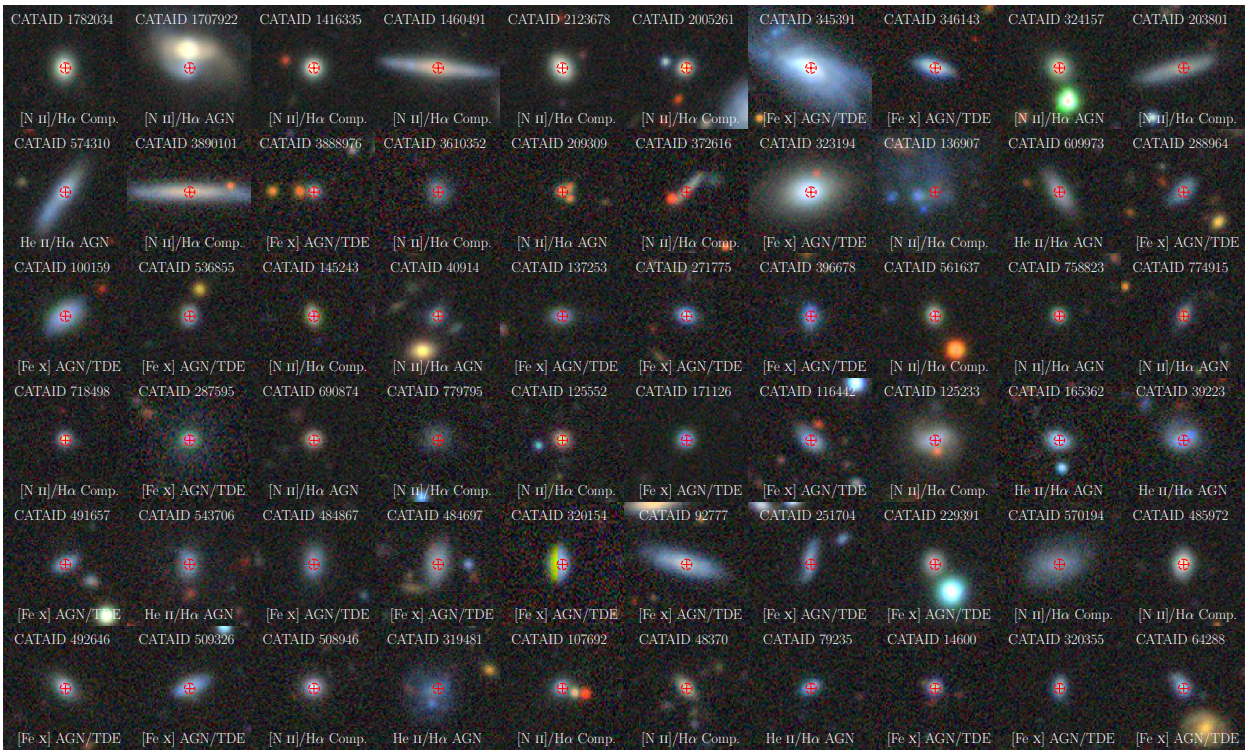

Figure 12: DESI Legacy Imaging Survey SkyViewer $grz-$band images of dwarf galaxies ($M_\star \leq 3 \times 10^9 M_\odot$) in our sample with available images (60/70). Red crosses indicate the positions of the spectra and the red dashed circles indicate the sizes of the GAMA spectroscopic fibers (with 2 arcsec diameters).

We used the ratio of [O III]/Hβ vs. [N II]/Hα as our first diagnostic. This diagnostic diagram has previously been used to identify AGNs in low-mass/dwarf galaxies (e.g., Moran et al., 2014; Reines et al., 2013; Sartori et al., 2015), and follow-up observations with X-rays have confirmed the existence of massive BHs in some of these sources independently (e.g., Baldassare et al., 2017). Moreover, the clean separation between the AGN and composite galaxies, and those consistent with star formation make these AGN candidates easily distinguishable. For these reasons, we consider the 71 AGNs identified by this diagnostic as secure and the 238 composite galaxies as strong AGN candidates. While this diagnostic provides a relatively clean sample, it can miss weakly accreting BHs and/or those residing in actively star-forming galaxies (particularly those with low metallicities).

Next, we searched for low-mass galaxies with relatively high He II/Hβ ratios. We employed a stricter criterion, $\log(\mathrm{He\,II/H}\beta) > -1$, to select AGNs than previous works (e.g., Sartori et al., 2015; Shirazi & Brinchmann, 2012) with the goal of providing a clean sample. This ratio is expected to be higher than what can be produced by stellar-mass X-ray binaries and Wolf-Rayet stars (Schaerer et al., 2019). We find 36 galaxies that meet this criterion. Of these, 10 are also [N II]/Hα AGNs and 1 is a composite. Given that the majority of the AGN candidates identified by this diagnostic are star-forming in the [N II]/Hα diagram, further observations are needed to confirm our results independently.

We also systematically searched for two high-ionization coronal lines ([Fe X]λ6374 and [Ne V]λ3426) in the spectra of our parent sample of low-mass galaxies. The [Fe X]λ6374 coronal line is detectable in 56 galaxies, only 2 of which have additional AGN indicators. As discussed in detail in Molina et al. (2021b), [Fe X]λ6374 can be produced by certain types of supernovae. However, one of the most extreme known examples is SN 2005ip supernovae with a peak luminosity of 2×10^{37} erg s^{-1} (Smith et al., 2009). This is an order of magnitude less than the minimum [Fe X] luminosity of 10^{38} erg s^{-1} in our sample. Thus, we are optimistic that these [Fe X] lines are produced by AGN activity or extreme coronal-line emitting TDEs, both of which require massive BHs. We found three galaxies with strong [Ne V] emission that are also [N II]/Hα AGNs. Two of these objects were also selected as AGNs using our He II/Hβ criterion.

In total we have found 388 unique low-mass galaxies exhibiting narrow-line signatures of active massive BHs, 47 of which have detectable broad Hα emission in their spectra. Using standard virial techniques, we estimated BH masses for these objects and find a range of $M_{\mathrm{BH}} \sim 10^{5.0-7.7} M_{\odot}$. The median BH mass is $10^{6.2} M_{\odot}$, consistent with expectations given the host galaxy stellar masses (Reines & Volonteri, 2015). We found an additional 56 star-forming galaxies with broad Hα emission in their spectra, with no narrow-line signatures indicating the presence of AGNs. Given that broad Hα in many star-forming dwarf galaxies

can be produced by transient stellar processes such as supernovae (Baldassare et al., 2016), we are suspicious of the broad-line objects without narrow-line signatures of AGNs and do not include them in our final sample of low-mass active galaxies.

As seen in previous works (Molina et al., 2021b; Reines et al., 2013), the various emission-line AGN diagnostics that we have used tend to probe different parts of the parameter space spanned by our parent sample of low-mass/dwarf galaxies (see Figure 11). For example, the [N II]/Hα AGNs/Composites are biased towards redder and more massive galaxies within our parent sample, and the [Fe X]-selected AGNs tend to be in bluer star-forming galaxies with a color and mass distribution more representative of our parent sample. Thus, using a multi-diagnostic approach can provide a more complete census of AGNs in low-mass/dwarf galaxies. While we have strived to strike a balance between assembling a clean yet comprehensive sample of low-mass/dwarf active galaxies in GAMA, large-scale follow-up campaigns would be useful to check the robustness of the AGN diagnostics we (and others) have applied in the low-mass regime.

Ultimately this work has provided an entirely new sample of hundreds of low-mass/dwarf active galaxies, which extends to southern sky regions and higher redshifts than previous searches in the low-mass regime. We find an AGN fraction of $\sim 1\%$, which is similar to other spectroscopic searches in this mass range. This active fraction provides a lower limit on the BH occupation fraction in low-mass galaxies with implications for the origin of the first BH seeds.

We thank the anonymous reviewer for their helpful comments and suggestions that improved this work. AER acknowledges support for this work provided by Montana State University and NASA through EPSCoR grant number 80NSSC20M0231.

MM is supported by funding from Ford Foundation Postdoctoral Fellowship, administered by the National Academies of Sciences, Engineering, and Medicine, awarded to MM in 2021-2022.

GAMA is a joint European-Australasian project based around a spectroscopic campaign using the Anglo-Australian Telescope. The GAMA input catalogue is based on data taken from the Sloan Digital Sky Survey and the UKIRT Infrared Deep Sky Survey. Complementary imaging of the GAMA regions is being obtained by a number of independent survey programmes including GALEX MIS, VST KiDS, VISTA VIKING, WISE, Herschel-ATLAS, GMRT and ASKAP providing UV to radio coverage. GAMA is funded by the STFC (UK), the ARC (Australia), the AAO, and the participating institutions. The GAMA website is http://www.gama-survey.org/. Based on observations made with ESO Telescopes at the La Silla Paranal Observatory under programme ID 179.A-2004. Based on observations made with ESO Telescopes at the La Silla Paranal Observatory under programme ID 177.A-3016.

The Legacy Surveys consist of three individual and complementary projects: the Dark Energy Camera Legacy Survey (DECaLS; Proposal ID 2014B-0404; PIs: David Schlegel and Arjun Dey), the Beijing-Arizona Sky Survey (BASS; NOAO Prop. ID 2015A-0801; PIs: Zhou Xu and Xiaohui Fan), and the Mayall z-band Legacy Survey (MzLS; Prop. ID 2016A-0453; PI: Arjun Dey). DECaLS, BASS and MzLS together include data obtained, respectively, at the Blanco telescope, Cerro Tololo Inter-American Observatory, NSF's NOIRLab; the Bok telescope, Steward Observatory, University of Arizona; and the Mayall telescope, Kitt Peak National Observatory, NOIRLab. The Legacy Surveys project is honored to be permitted to conduct astronomical research on Iolkam Du'ag (Kitt Peak), a mountain with particular significance to the Tohono O'odham Nation.

NOIRLab is operated by the Association of Universities for Research in Astronomy (AURA) under a cooperative agreement with the National Science Foundation.

This project used data obtained with the Dark Energy Camera (DECam), which was constructed by the Dark Energy Survey (DES) collaboration. Funding for the DES Projects has been provided by the U.S. Department of Energy, the U.S. National Science Foundation, the Ministry of Science and Education of Spain, the Science and Technology

Facilities Council of the United Kingdom, the Higher Education Funding Council for England, the National Center for Supercomputing Applications at the University of Illinois at Urbana-Champaign, the Kavli Institute of Cosmological Physics at the University of Chicago, Center for Cosmology and Astro-Particle Physics at the Ohio State University, the Mitchell Institute for Fundamental Physics and Astronomy at Texas A&M University, Financiadora de Estudos e Projetos, Fundacao Carlos Chagas Filho de Amparo, Financiadora de Estudos e Projetos, Fundacao Carlos Chagas Filho de Amparo a Pesquisa do Estado do Rio de Janeiro, Conselho Nacional de Desenvolvimento Cientifico e Tecnologico and the Ministerio da Ciencia, Tecnologia e Inovacao, the Deutsche Forschungsgemeinschaft and the Collaborating Institutions in the Dark Energy Survey. The Collaborating Institutions are Argonne National Laboratory, the University of California at Santa Cruz, the University of Cambridge, Centro de Investigaciones Energeticas, Medioambientales y Tecnologicas-Madrid, the University of Chicago, University College London, the DES-Brazil Consortium, the University of Edinburgh, the Eidgenossische Technische Hochschule (ETH) Zurich, Fermi National Accelerator Laboratory, the University of Illinois at Urbana-Champaign, the Institut de Ciencies de l'Espai (IEEC/CSIC), the Institut de Fisica d'Altes Energies, Lawrence Berkeley National Laboratory, the Ludwig Maximilians Universitat Munchen and the associated Excellence Cluster Universe, the University of Michigan, NSF's NOIRLab, the University of Nottingham, the Ohio State University, the University of Pennsylvania, the University of Portsmouth, SLAC National Accelerator Laboratory, Stanford University, the University of Sussex, and Texas A&M University.

BASS is a key project of the Telescope Access Program (TAP), which has been funded by the National Astronomical Observatories of China, the Chinese Academy of Sciences (the Strategic Priority Research Program "The Emergence of Cosmological Structures" Grant No. XDB09000000), and the Special Fund for Astronomy from the Ministry of Finance. The BASS is also supported by the External Cooperation Program of Chinese Academy

of Sciences (Grant No. 114A11KYSB20160057), and Chinese National Natural Science Foundation (Grant No. 11433005).

The Legacy Survey team makes use of data products from the Near-Earth Object Wide-field Infrared Survey Explorer (NEOWISE), which is a project of the Jet Propulsion Laboratory/California Institute of Technology. NEOWISE is funded by the National Aeronautics and Space Administration.

The Legacy Surveys imaging of the DESI footprint is supported by the Director, Office of Science, Office of High Energy Physics of the U.S. Department of Energy under Contract No. DE-AC02-05CH1123, by the National Energy Research Scientific Computing Center, a DOE Office of Science User Facility under the same contract; and by the U.S. National Science Foundation, Division of Astronomical Sciences under Contract No. AST-0950945 to NOAO.

Appendix: Observed Spectra and Emission-Line Fits for the He II AGNs and [Fe X] AGNs/TDEs

In this appendix, we show spectra of a selection of He II/Hβ AGNs that are SF in the [N II]/Hα diagram in Figure 13 and the He II emission-line fits for all the 36 He II/Hβ AGNs in Figure 14, while the spectra of a selection of [Fe X] AGNs/TDEs are plotted in Figure 15 and the [Fe X] and [O I] doublet emission-line fits for all 56 [Fe X] galaxies in Figure 16.

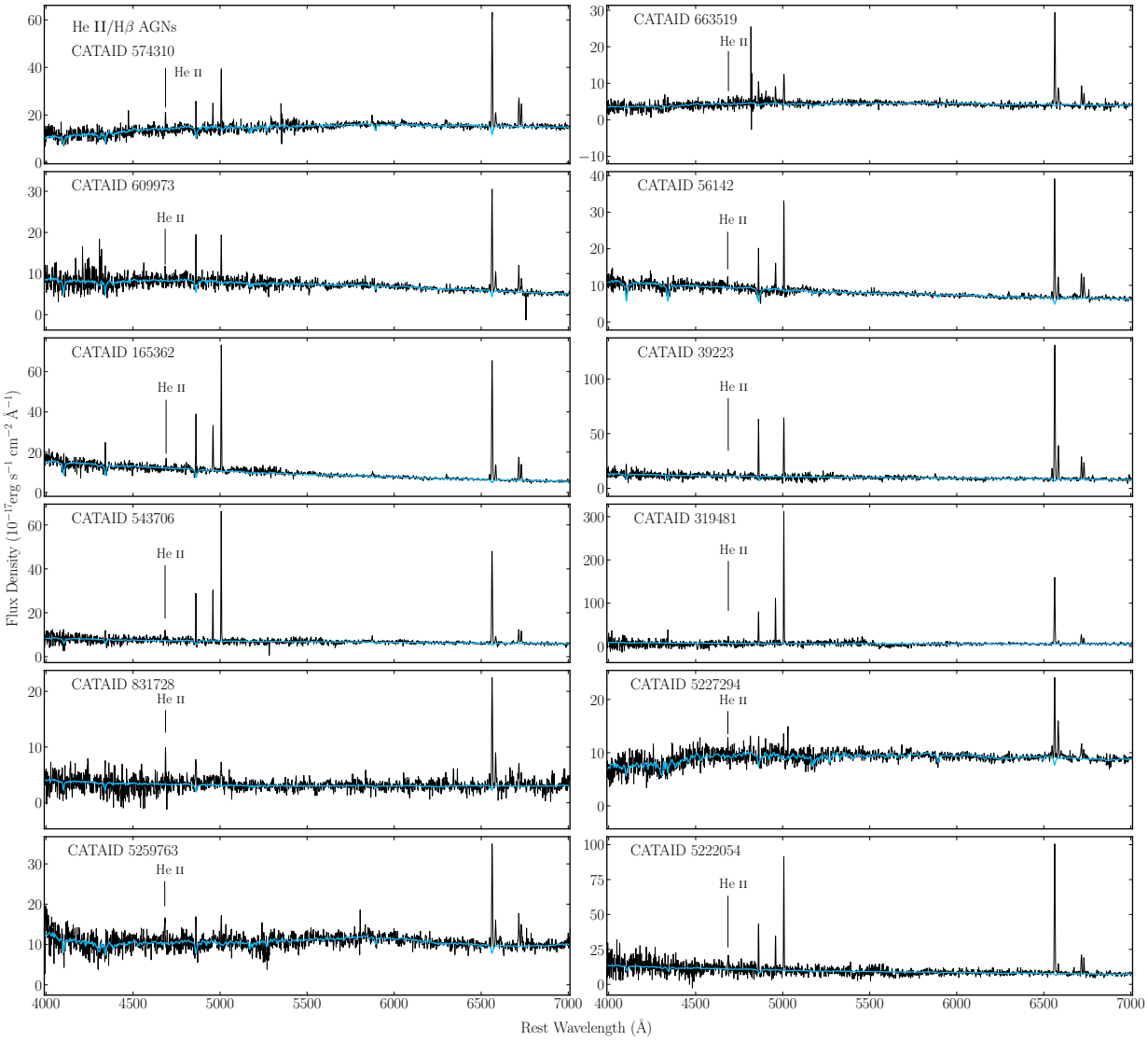

Figure 13: Redshift-corrected spectra of a selection of He II/Hβ AGNs overplotted with the continuum model (sky blue). These He II/Hβ AGNs are SF in the [N II]/Hα diagram.

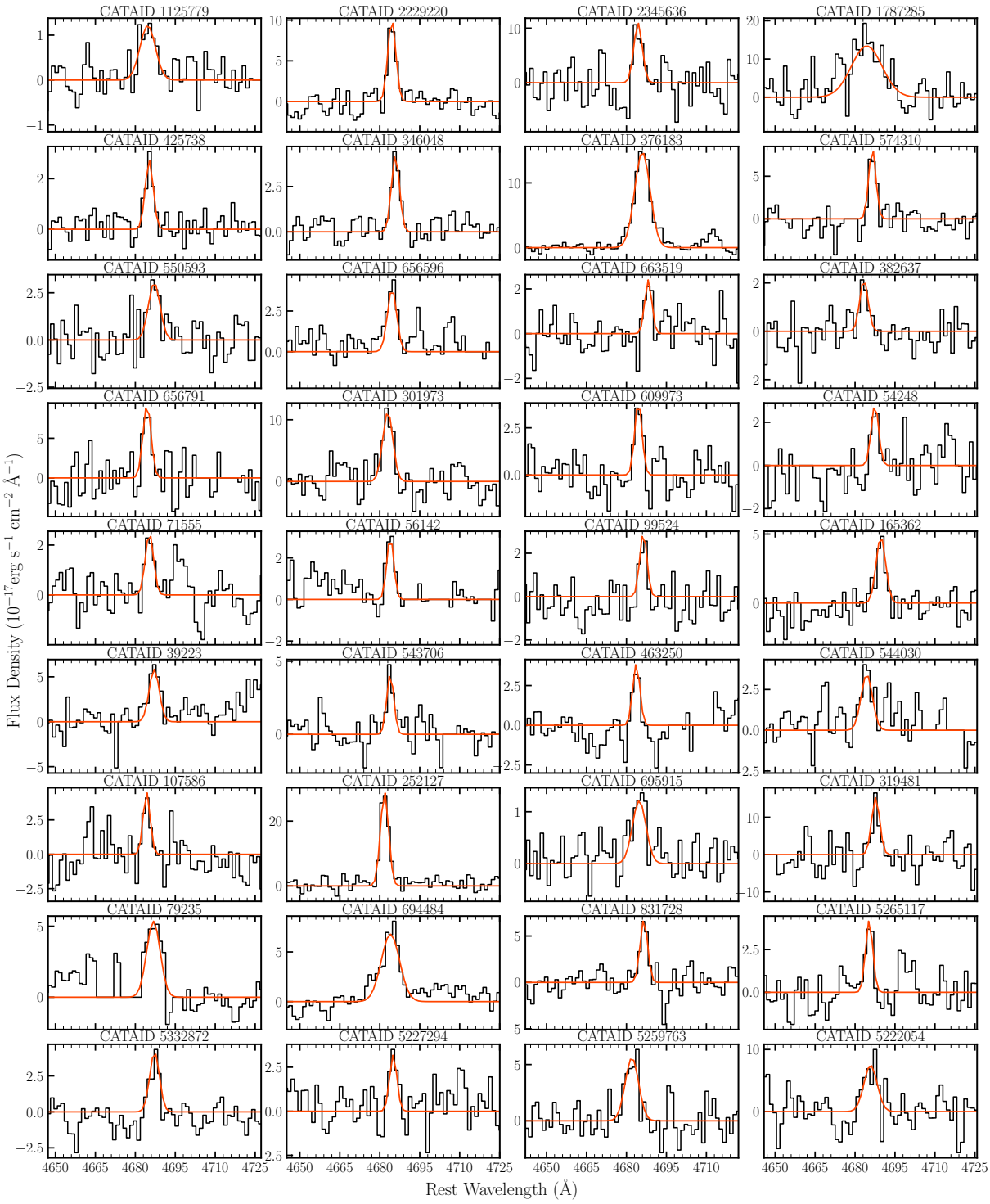

Figure 14: Chunks of the He II spectra and the single Gaussian emission-line fits for the 36 He II/Hβ AGN candidates. Here the continuum-subtracted spectrum are shown as black and the individual Gaussian component as orange-red. 10 of these galaxies are [N II]/Hα AGNs, while 1 is a composite object. See section 4.2 for details.

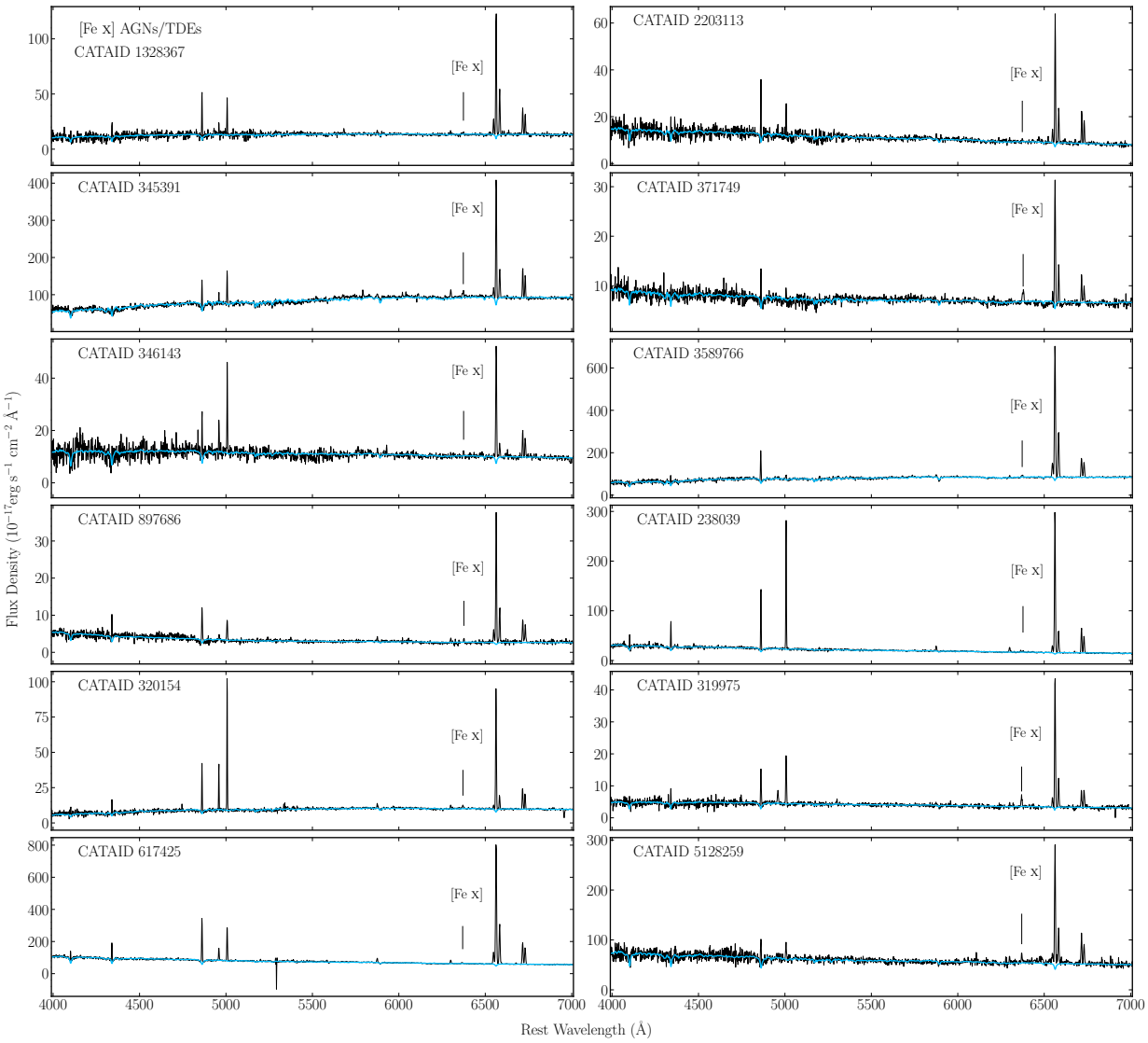

Figure 15: Redshift-corrected spectra of a selection of [Fe X] AGNs/TDEs overplotted with the continuum model (sky blue). These objects are SF in the [N II]/Hα diagram.

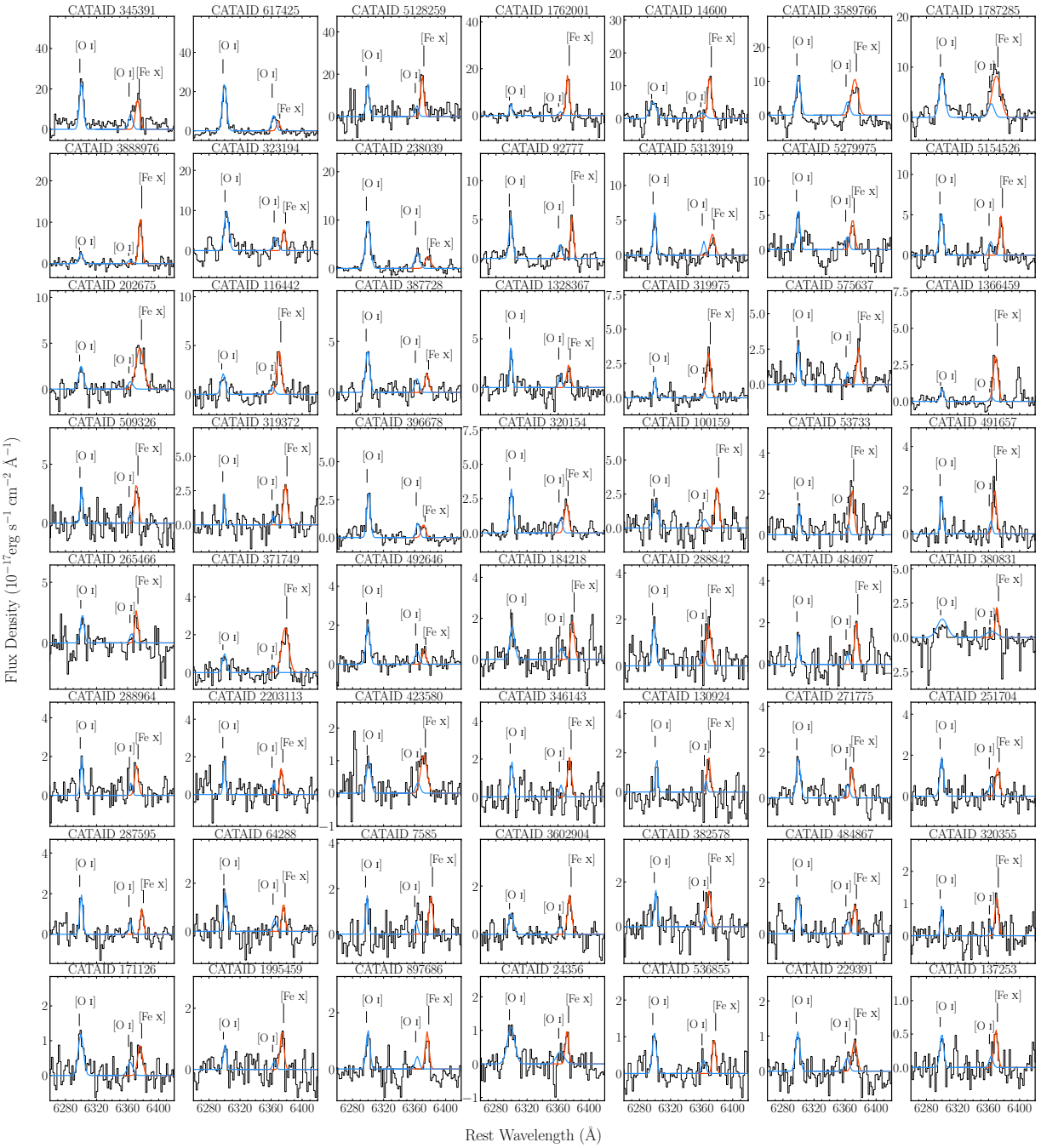

Figure 16: Chunks of [Fe X] emission-line spectra and the Gaussian emission-line fits for the 56 galaxies with this emission. We plot the single Gaussian models for the [O I]λ6300,6363 lines in blue and [Fe X]λ6374 line in red. Here the galaxy with CATAID 1787285 is an [N II]/Hα and He II/Hβ AGN, and the object with CATAID 387728 is an [N II]/Hα Composite. The [Fe X] lines in our sample have luminosities that span a range of 10^{38}–10^{41} erg s^{-1}, with a median of $10^{39.6}$ erg s^{-1}, which can be explained by AGNs or TDEs. See Section 4.3 for details.

IONIZED GAS OUTFLOWS IN THE GALAXY AND MASS ASSEMBLY (GAMA) SURVEY: SIGNATURES OF AGN FEEDBACK IN LOW-MASS GALAXIES

Contribution of Authors and Co-Authors

Manuscript in Chapter 3

Author: Sheyda Salehirad

Contributions: Analyzed the data, visualized the data, and wrote the manuscript.

Author: Amy E. Reines

Contributions: Provided feedback on the results, edited and provided comments on the manuscript.

Author: Mallory Molina

Contributions: Edited and provided comments on the manuscript.

Manuscript Information

Sheyda Salehirad, Amy Reines, Mallory Molina

The Astrophysical Journal

Status of Manuscript:
____ Prepared for submission to a peer-reviewed journal
____ Officially submitted to a peer-reviewed journal
____ Accepted by a peer-reviewed journal
_X_ Published in a peer-reviewed journal

IOP Publishing
The Astrophysical Journal,Volume 979, Number 1
DOI: 10.3847/1538-4357/ad9a57

Introduction

Supermassive black holes (BHs) with masses $M_{\rm BH} \sim 10^{6-10} M_{\odot}$ are found in the nuclei of almost all massive galaxies (Kormendy & Ho, 2013; Kormendy & Richstone, 1995) and these BHs have primarily grown over cosmic time through merger-driven accretion. Observations show a tight correlation between BH mass and both galaxy bulge mass and stellar velocity dispersion (e.g., Ferrarese & Merritt, 2000; Gebhardt et al., 2000; Gültekin et al., 2009; Marconi & Hunt, 2003; McConnell & Ma, 2013; Tremaine et al., 2002), suggesting a connection between the evolution of these BHs and their host galaxies. Theoretical models indicate that this co-evolution can be regulated by feedback from an active galactic nucleus (AGN; Churazov et al., 2005; Schaye et al., 2015; Silk & Rees, 1998; Somerville et al., 2008; Vogelsberger et al., 2014). AGN feedback via radiation and outflows can impact the interstellar medium (ISM) in a galaxy and heat or eject the gas, ultimately inhibiting star formation and BH growth.

Without incorporating AGN feedback in galaxy models, key observational properties of galaxies such as the sharp cut-off at the end of the galaxy luminosity function can not be reproduced (e.g., Baldry et al., 2012; Bower et al., 2006). AGN feedback explains the red color of spheroidal galaxies, the lack of super bright and very massive galaxies, and the X-ray temperature-luminosity relationship (e.g., Benson et al., 2003; Croton et al., 2006; Markevitch, 1998; McCarthy et al., 2010; Menci et al., 2006).

Evidence for outflows has been found in both nearby galaxies (Balmaverde et al., 2016; Mullaney et al., 2013; Rupke & Veilleux, 2011; Veilleux et al., 2005), and high-redshift objects (Alexander et al., 2010; Carniani et al., 2015), and in ionized, atomic, and molecular phases of gas (Cazzoli et al., 2014; Cicone et al., 2012, 2014; Feruglio et al., 2010; Fluetsch et al., 2021; Morganti, 2017; Veilleux et al., 2020). Outflows produced by AGNs are usually thought to reduce or quench star formation (e.g., Ellison et al., 2021; Hopkins et al., 2006; Pereira-

Santaella et al., 2018; Springel et al., 2005), however, in some cases, it can increase star formation activity (Cresci et al., 2015; Schutte & Reines, 2022; Silk, 2013; Zubovas et al., 2013). We know the radiation fields and jets from accretion disks can launch outflows in AGNs, while star formation (e.g., stellar winds and supernovae) can also produce them (see, Heckman & Thompson, 2017; Rupke, 2018; Veilleux et al., 2020; Wylezalek & Morganti, 2018, for reviews). However, many of the exact driving mechanisms are still elusive. It is often unknown if the same mechanisms drive different phases of outflows and if they have similar spatial distributions. We also usually do not know the exact morphology of the outflows (shell-like or conical).

It has long been believed that stellar feedback is the main source of feedback in low-mass galaxies (e.g., Martín-Navarro & Mezcua, 2018). However, the rising observational evidence of AGNs (Baldassare et al., 2016; Molina et al., 2021b; Moran et al., 2014; Reines, 2022; Reines et al., 2013; Salehirad et al., 2022; Sartori et al., 2015) as well as recent findings of AGN-driven outflows in this mass range (Aravindan et al., 2023; Liu et al., 2020; Manzano-King et al., 2019; Penny et al., 2018) suggest the notable impact of AGN feedback in these objects. Theoretical models have proposed contrasting results regarding AGN feedback in low-mass galaxies. Some studies found that AGN feedback quenches star formation (Barai & de Gouveia Dal Pino, 2019; Dashyan et al., 2018), while others predict a negligible effect from AGN feedback contrary to stellar feedback (Trebitsch et al., 2018). Additionally, some simulations indicate that AGN feedback increases the outflow energetics in these galaxies (Koudmani et al., 2021, 2019).

The existence of broad-line features in the [O III]$\lambda\lambda$4959, 5007 doublet line profile is a well-established tracer of ionized gas outflows (Heckman et al., 1981; Stockton, 1976). Given the forbidden transition of this line, [O III] can not be produced in the dense broad line region (BLR) around an AGN and it can be used to investigate ionized gas dynamics in the narrow line region (NLR). Strong velocity gradients in the NLR associated with outflows can

be observed as broadening or shifting of the [O III] line that exceeds normal galaxy dynamics and can extend to kiloparsecs (e.g., Pogge, 1989).

In this paper, we search for ionized gas outflows in a large sample of galaxies with spectra in the Galaxy and Mass Assembly (GAMA) Survey Data Release 4 (DR4; Driver et al., 2022; Liske et al., 2015). Our primary focus is on identifying outflows in low-mass galaxies with stellar masses $M_\star < 10^{10} M_\odot$. The GAMA survey covers equatorial and southern sky regions and has minor overlaps with galaxies in the Sloan Digital Sky Survey (SDSS). GAMA is also two magnitudes deeper than the SDSS. While extensive research has been conducted on galaxies exhibiting outflow signatures in SDSS (e.g, Matzko et al., 2022; Mullaney et al., 2013), the GAMA survey remains relatively unexplored. Therefore, our objective is to discover new galaxies displaying ionized outflow signatures among both massive and low-mass objects, including AGNs and SF galaxies. We aim to analyze the outflow properties of these objects, specifically their offset and outflow velocities.

Section 2 details our data and sample selection process. Sections 3 and 4 present the analysis and results. The summary and conclusions can be found in Section 5. We assume a ΛCDM cosmology with $\Omega_m = 0.3$, $\Omega_\Lambda = 0.7$ and $H_0 = 70$ km s^{-1} Mpc^{-1}.

Data and Parent Sample

The GAMA Survey

We use the publicly available data from the GAMA Survey DR4 (Driver et al., 2022; Liske et al., 2015) to conduct our study. The GAMA survey comprises optical spectroscopic observations taken with the AAOmega multi-object spectrograph (Saunders et al., 2004; Sharp et al., 2006; Smith et al., 2004) on the 3.9 m Anglo-Australian Telescope. The wavelength range of the dual-beam set-up of the spectrograph is 3730–8850 Å, the spectral resolution of the blue and red arms are 3.5 and 5.3 Å, respectively, and the spectroscopic fibers are 2" in diameter. The survey covers 2 southern regions (G02 and G23), with respective

areas of 56 and 51 deg^2, and three 60 deg^2 equatorial regions (G09, G12 and G15). The magnitude limit for the main survey of galaxies in the equatorial and G02 regions is each r < 19.8 mag and the limiting magnitude of the G23 region is i < 19.8 mag (Baldry et al., 2018; Driver et al., 2022).

Parent Sample of Galaxies

We define our parent sample using the spectra provided in the `AATSpecAll v27` table in the `SpecCat` data management unit (DMU; Liske et al., 2015) and following the Salehirad et al. (2022) methodology, as described here. To ensure high-quality data, we select spectra with `COMMENTS_FLAG` $= 0$, which excludes unreliable detections such as those with fringing and bad splicing. We choose spectra with normalized redshift values of `NQ`> 2, as suggested by GAMA, corresponding to a minimum 90% probability that the best redshift estimate is accurate. If multiple observations are available for a galaxy, we select the spectrum with the best redshift using the column value `IS_SBEST` $= 1$. The redshift is determined using cross-correlation of spectra and stellar templates, with the best-estimated redshift adopted from the highest cross-correlation peak, normalized by a root mean square value. The confidence in this redshift estimate is assessed by comparing the height of the highest correlation peak with those of the next three best redshift estimates (Liske et al., 2015, and the references therein). Finally, we only include objects with redshifts z < 0.3 to ensure the lines of interest such as the [S II] doublet are detected.

We then apply signal-to-noise ratio (S/N) cuts similar to Reines et al. (2013), using the emission-line fluxes and equivalent width (EW) measurements given in the `GaussFitSimple v05` table from the `SpecLineSFR` DMU (Gordon et al., 2017). We select galaxies that have S/N ≥ 3 and EW > 1 Å for the Hα, [O III] λ5007 and [N II] λ6583 lines. Given that the Hβ line is generally a weaker line compared to the Hα line, we select those with S/N ≥ 2.

The stellar masses are stored in the `StellarMasses` DMU (Taylor et al., 2011)

and in various tables depending on the sky regions. We include all the galaxies with available stellar mass estimates and impose a mass cut of $M_\star > 10^5$ $M_\odot$ to avoid possible star detections. Stellar masses for galaxies in the G23 region are only given in the `StellarMassesGKV v24` table (Driver et al., 2022) which also contains stellar masses for the equatorial galaxies. Here, the masses are derived using all band photometry from the Kilo-Degree Survey (KiDS; Kuijken et al., 2019) and the Visible and Infrared Survey Telescope for Astronomy Kilo-degree Infrared Galaxy Public Survey (VIKING; Edge et al., 2013). Tables `StellarMassesG02SDSS v24` and `StellarMassesG02CFHTLS v24` provide stellar masses for the G02 galaxies. The values in these tables are derived by multi-band spectral energy distribution (SED) fitting to SDSS and Canada-France-Hawaii Telescope Lensing (CFHTLenS; Heymans et al., 2012) photometry, respectively. We utilize the stellar masses given in the `StellarMassesG02CFHTLS v24` table but use the `StellarMassesG02SDSS v24` table to exclude the galaxies with masses that are different by 0.3 dex in both tables. Our final sample consists of 39,612 galaxies.

Spectral Analysis

In this paper, we systematically search for double-component features in the [O III] $\lambda\lambda 4959, 5007$ doublet lines that may signify outflows. Complex emission line profiles exhibiting asymmetries, shoulders, and/or double peaks can indicate the presence of two or more gaseous components with distinct kinematics along the line of sight. However, non-Gaussian line structure can also result from beam-spearing of the velocity gradient due to relatively coarse spatial resolution (García-Lorenzo et al., 2015).

In previous studies, the broad blueshifted wings in the [O III] line profile have been interpreted as outflows (e.g., Geach et al., 2018; Guolo-Pereira et al., 2021; Harrison et al., 2016; Mullaney et al., 2013; Zakamska & Greene, 2014), constituting around 40% of the overall flux of the [O III] line (e.g., Concas et al., 2017). Fewer studies have focused on

broad redshifted lines in the [O III] line profile, but they could also be attributed to outflows depending on the inclination of the galaxy with respect to the line of sight (Bae & Woo, 2016; Crenshaw et al., 2010). In cases of bipolar outflows and depending on the orientation, we can also observe symmetric broad lines (Harrison et al., 2012). Therefore, to accumulate a more comprehensive outflow sample, we do not limit our search to blueshifted broad wings and freely select the center of the second component.

While our parent sample is determined using the emission-line flux measurements provided in the GAMA survey, we write our custom code to analyze the spectra and fit the emission lines. We subsequently visually inspect each flagged galaxy spectrum and exclude the unreliable ones, such as those with bad fits (fits to the noise in the spectrum), those with missing pixel values within the emission lines, and those affected by bad splicing or fringing. In this section, we describe our method for fitting the continuum, selecting outflow candidates, evaluating outflow velocities, and modeling other relevant emission lines.

Stellar Continuum Subtraction

We use the Penalized Pixel-Fitting method (`pPXF`; Cappellari, 2017) to fit the stellar continuum for each galaxy. We utilize the stellar population synthesis models from Bruzual & Charlot (2003) as our stellar continuum templates in 3 metallicities ($Z = 0.008, 0.02, 0.05$) and 10 ages (t=0.005, 0.025, 0.1, 0.29, 0.64, 0.9, 1.4, 2.5, 5, and 11 Gyr). Initially, we model the spectra with a combination of single-metallicity templates of various ages, modified by a low-order multiplicative polynomial to account for dust reddening, and select the model metallicity with the smallest χ^2 value. This method produces reliable continuum fits for the majority of the galaxies in our sample. However, the initial continuum fit in some cases yields unrealistically large velocity dispersion values given by `pPXF`, which is evident in the extreme broadening of the absorption line fits. For these objects, we redo the fits by changing the order of the multiplicative polynomials, adding additive polynomials as they can minimize

the template mismatch by changing the strength of the absorption lines (Cappellari, 2017), or changing the wavelength range of the spectrum to cut the noisy ends. Since our primary goal is to measure the emission lines, we attempt good fits to the stellar continua but do not fully explore the parameter space. An example of a fitted galaxy spectrum in our sample is shown in Figure 17.

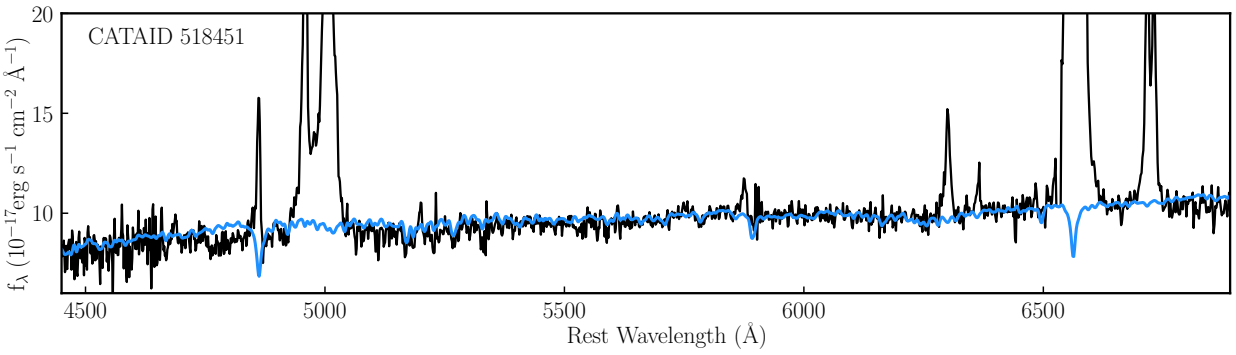

Figure 17: An example of stellar continuum fit (AGN with CATAID 518451). Here the redshift-corrected spectrum is shown in black and the best-fitted stellar continuum model is in blue. See Section 3.1 for details.

We also find a handful of AGN-dominated spectra among the flagged galaxies in which the stellar templates do not provide an optimal fit to the continuum. However, since we include a linear component in the fit of the emission lines of interest (see below), the [O III] doublet lines are fitted sufficiently in the end.

Fitting the [O III] lines

We use the `LMFIT` package in python (Newville et al., 2014) to fit chunks of spectra around the [O III]$\lambda\lambda 4959, 5007$ doublet. We incorporate Gaussian models to fit the emission lines and a linear model which accounts for the continuum fit residuals.

We fit the [O III]$\lambda\lambda 4959, 5007$ doublet lines simultaneously with both one- and two-Gaussian models. In the one-Gaussian model, the lines in the doublet are restricted to have equal velocity widths, fixed laboratory separation, and a flux ratio

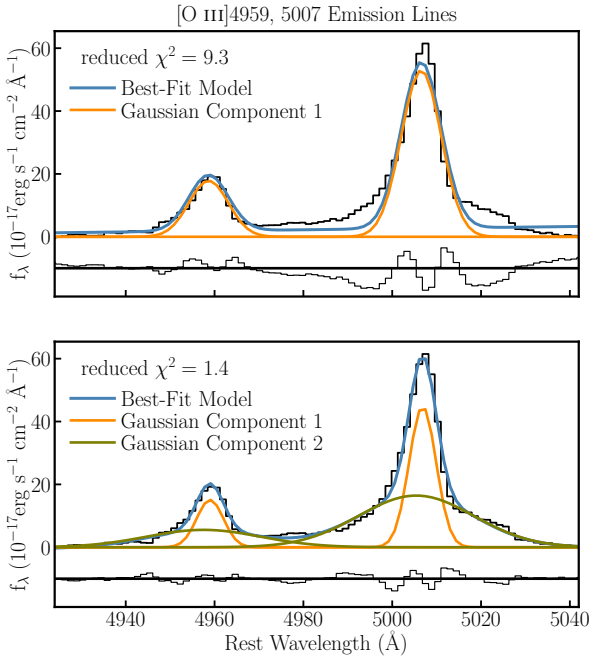

Figure 18: The [O III] doublet emission line plotted with two different fitting models. The top panel shows a single Gaussian model fitted to each line, while the bottom panel displays two Gaussian fits. The black line represents the observed emission line. The blue line indicates the best-fitting model, which consists of Gaussian and linear components. The orange line shows the narrow (systemic) component, while the olive line depicts the broad (outflow) component. Residuals are displayed in black with a vertical offset. Adding a second component into the [O III] fit for this galaxy significantly improves the final model. For more information, see Section 3.2.

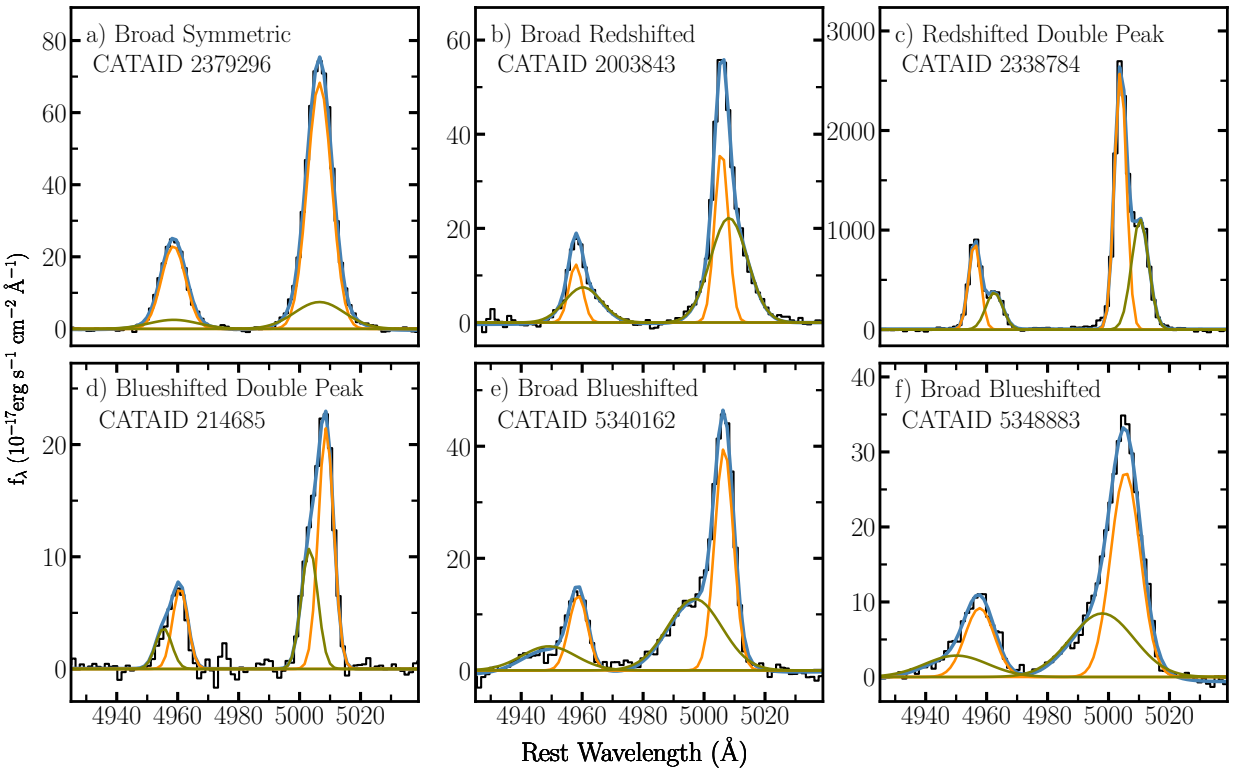

Figure 19: Examples of the [O III]$\lambda\lambda$4959, 5007 doublet line profiles from our outflow sample, fitted using two-Gaussian models. The color scheme matches that of Figure 18. Panels (a) and (b) show cases with broad symmetric and broad redshifted outflow lines, respectively. Panels (c) and (d) present lines exhibiting two peaks, with components that have similar widths. Panels (e) and (f) show broad blueshifted lines. In panel (e), the overall line profile indicates a blueshifted bump, while the components are blended in panel (f). For further details, refer to Section 3.2.

of [O III]λ5007/[O III]λ4959 = 3. In the two-Gaussian model, we allow the first and second components of the [O III]λ5007 line to change freely, however, the [O III]λ4959 line components have the same velocity widths, fixed separation, and fixed flux ratio to the respective [O III]λ5007 line components. The two-component model is adopted if the reduced χ^2 is lowered by at least 20% relative to the one-component model, and the second components are broader than the first components. We only select lines with widths that are at least equal to the instrumental spectral resolution ($v_{FWHM} \geq 200$ km s^{-1}), those that have a flux S/N ≥ 3 for each of the Gaussian components, and second components with line

peaks that are at least 3σ above the root mean square (rms) noise level of the continuum chunk. Figure 18 shows an example of modeled emission lines.

We identified 439 galaxies with outflow signatures in the [O III]$\lambda\lambda$4959, 5007 lines. After visually inspecting the fits of all the flagged candidates, we remove 41 objects with unreliable fits. These cases consist of objects with spectra affected by fringing and bad spicing and those with lines fit to the continuum noise. Our final sample consists of 398 galaxies.

We find outflow components that are symmetric with respect to the narrow (systemic) component, as well as those that are blueshifted or redshifted. Some of the identified second components contribute to as little as 5% of the total flux of the [O III] line, potentially representing weaker outflows or non-Gaussian profiles. Despite their weaker nature, these second components meet the necessary criteria, and hence, we include them in our final sample. In 9% of the outflow candidates, we observe either two distinct peaks in the overall [O III] line profile or less pronounced double peaks, but lines with similar widths. These lines can be what some studies call double-peaked lines, where they are usually associated with disk rotation of the NLR around a single BH, biconical outflows, or distinct NLRs in merging AGNs (e.g., Shen et al., 2011). Indeed, these lines have been found in single AGNs (e.g., Bizyaev et al., 2022; Müller-Sánchez et al., 2015; Nevin et al., 2018) as well as dual AGNs (Fu et al., 2023; Rosario et al., 2011). Examples of [O III] doublet emission-line profiles are shown in Figure 19.

Outflow Velocity

In this work, we use W_{80} to estimate outflow velocity, defined as the line width encompassing 80% of the flux of the emission line (Zakamska & Greene, 2014). For a Gaussian profile, W_{80} is related to the FWHM of the line and can be described as $W_{80} = 1.09$FWHM as shown in Figure 20. Some studies account for the offset velocity (v_o) between the outflow and systemic emission-line components when evaluating the outflow

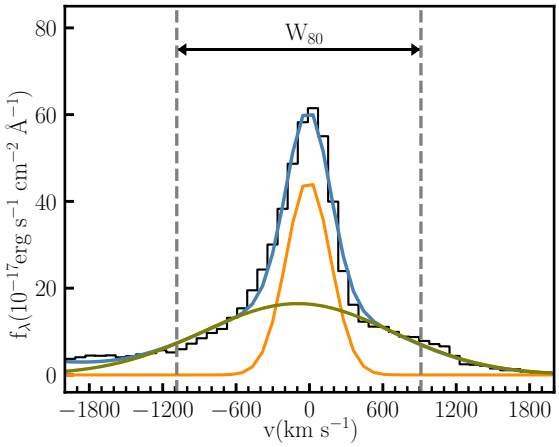

Figure 20: This plot illustrates an example of $W_{80} \sim$ FWHM (dashed gray lines) for the outflow component (green line) from the [O III]λ5007 emission, indicating outflow velocity. See Section 3.3 for details.

velocity (e.g., Manzano-King et al., 2019). However, the offset velocity is sensitive to dust extinction and inclination effects (Bae & Woo, 2016; Harrison et al., 2014), while W_{80} is less affected by these factors and can better reflect typical bulk motions (Harrison et al., 2014). Considering the sensitivity of v_o to extinction and the fact that our sample includes both redshifted and blueshifted outflows (see Section 3.2), we adopt W_{80} as our measure of outflow velocity.

Other Emission Line Measurements

We also fit Gaussian models to the [S II]$\lambda\lambda$6716, 6731, [N II]+Hα, Hβ, and [O I]λ6003 emission lines in our outflow sample following the methodology in Reines et al. (2013) and references therein, as described below. The profiles of these lines do not typically match the profile of the [O III] lines and therefore, we fit them independently. We use the derived emission line fluxes with S/N $\geq$ 3 to classify the outflow candidates based on their location on two-dimensional diagnostic diagrams (see Section 4.1). An example of our fits for these lines is shown in Figure 21 and the host galaxy properties and the emission-line fluxes of the outflow candidates are listed in Tables 5 and 6, respectively.

We fit the [S II] lines with one- and two-Gaussian components. For the single Gaussian model, the widths of the lines are assumed to be equal (in velocity space) while the laboratory separation between the lines is held fixed. In the two-component case, we restrict the relative widths, heights, and centers of the two components to be the same for both lines in the doublet. If the reduced χ^2 of the two-component model is at least 20% less and the width of the second component is larger than the first component, we select the two-Gaussian model for the [S II] lines. This is the case in 30 of the outflow candidates.

Given that the profiles of the [N II]$\lambda\lambda$6548, 6583 and Hα lines often match the [S II] lines (Filippenko & Sargent, 1988, 1989; Greene & Ho, 2004; Ho et al., 1997), we use the parameters from the [S II] doublet models to fit the [N II]+Hα complex. For the one-Gaussian model, we assume the [N II] lines have equal velocity widths to that of the [S II] lines, their laboratory relative wavelength separation is fixed, and the flux ratio of [N II]λ6583/[N II]λ6548 = 3. The width of the Hα line is allowed to increase as much as 25%. For the 30 objects with two-component fits to their [S II] doublet lines, we scale the widths, centers, and heights of their [N II] and Hα components to that of the [S II] lines.

To search for broad Hα emission that could signify dense gas orbiting a BH, we fit the lines with an additional broad Hα component and select this model if the full-width at half maximum (FWHM) of the broad Hα line is at least 500 km s^{-1} after correcting for the instrumental resolution, and the reduced χ^2 of the model with the addition of the broad Hα component is at least 20% less than the one without. We identify 206 outflow galaxies with broad Hα emission. The Hβ line is fitted using the same method as the Hα line, using the [S II] profile as a template for the narrow line.

We also fit the [O I]λ6003 line with one- and two-Gaussian models and select the two-component model if the width of the second component is larger than that of the first one, and the reduced χ^2 is lowered by at least 20%. Given that the [O I] line is often weak, in addition to requiring a flux S/N $\geq$ 3, we also only select those with line peaks at least 3σ

above the rms noise. We find that 268 galaxies meet the [O I] detection criteria, of which 25 have broad [O I]λ6003 component.

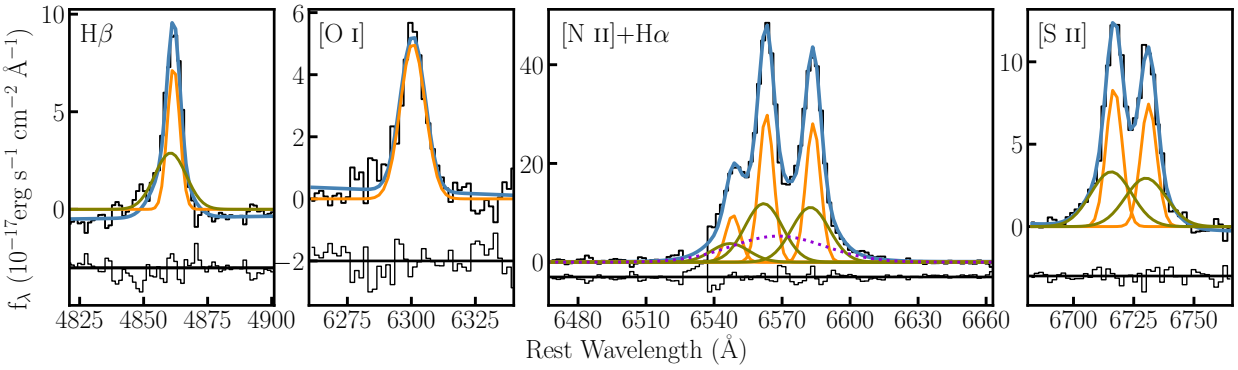

Figure 21: This figure shows chunks of emission-line spectra for Hβ, [O I]λ6003, [N II]+Hα complex, and the [S II]$\lambda\lambda$6716, 6731 lines. The color scheme matches that of Figure 18. The dotted violet line represents the broad Hα model. The residuals are plotted in black with a vertical offset. For more information, see Section 3.4.

Table 5: Outflow Galaxies

CATAID	RA (degrees)	DEC (degrees)	z	log $(M_*/M_\odot)$	$g-r$ (mag)	[N II]/Hα Classification	[S II]/Hα Classification	[O I]/Hα Classification	v_0 (km s^{-1})	v_{out} (km s^{-1})
(1)	(2)	(3)	(4)	(5)	(6)	(7)	(8)	(9)	(10)	(11)
1560359	30.28563	-4.67478	0.21100	10.73	0.62	AGN	Sy	...	-408±50	1415±80
1534204	30.75825	-6.25522	0.13416	10.29	0.39	SF	SF	SF	-3±22	684±104
1557617	30.82937	-4.83862	0.13701	8.91	0.04	SF	Sy	Sy	73±44	866±145
1485133	30.97987	-9.31706	0.29487	11.04	0.72	AGN	Sy	Sy	47±8	1349±35
1555278	31.00350	-4.98673	0.25509	10.34	0.41	AGN	Sy	Sy	-113±24	925±65
1568106	31.09625	-4.14728	0.21588	11.01	0.62	AGN	Sy	Sy	-317±50	1416±64
2230554	32.08583	-5.35770	0.20913	10.88	0.60	AGN	Sy	Sy	-151±40	1381±118
2202335	32.14975	-4.17996	0.05719	10.05	0.56	Comp.	SF	SF	0±54	1145±210
1307713	32.82988	-5.73585	0.04248	10.28	0.61	AGN	Sy	Sy	125±16	836±25
2204417	32.98467	-3.82524	0.09473	10.81	0.56	Comp.	Sy	Sy	212±79	829±114

Note—Properties of the outflow candidates in this work. Columns 1-6 are obtained from GAMA DR4 and assume $h = 0.7$. Column 1: Unique ID of the GAMA object. Columns 2–3: The right ascension and declination (in degrees) of the spectrum (J2000). Column 4: Redshift. Columns 5–6: The log galaxy stellar mass in units of $M_\odot$ and $g-r$ color. All values are obtained from the `StellarMassesGO2CFHTLS v24` and `StellarMassesGKV v24` tables (Bellstedt et al., 2020; Taylor et al., 2011). Columns 7–9: Classifications of the galaxy in the narrow-line diagnostic diagrams. Columns 10–11: The offset and outflow velocities derived from the components of the [O III]λ5007 line in km s^{-1} with errors included. A three-dot ellipsis indicates no line is detected, or the emission lines do not meet our reliable detection criteria. The entirety of Table 5 is published in the electronic edition of *The Astrophysical Journal*. We show a portion here to give information on its form and content.

Table 6: Emission-line Fluxes

CATAID (1)	Hβ_n (2)	Hβ_b (3)	[O III]λ5007$_n$ (4)	[O III]λ5007$_b$ (5)	[O I]λ6300 (6)	Hα_n (7)	Hα_b (8)	[N II]λ6583 (9)	[S II]λ6716 (10)	[S II]λ6731 (11)
1560359	62±6	...	234±12	183±17	...	205±6	132±18	213±5	76±4	64±4
1534204	802±13	...	366±41	233±39	87±4	3248±13	304±31	1114±12	598±8	408±7
1557617	204±3	...	1372±9	76±12	15±2	787±2	...	24±2	36±4	33±4
1485133	23±6	66±6	525±7	329±8	15±1	242±4	158±13	167±4	56±4	54±3
1555278	46±3	...	154±15	146±15	27±4	204±3	115±18	101±3	27±4	39±5
1568106	91±13	...	344±50	481±54	65±8	284±17	475±40	328±15	166±9	138±9
2230554	46±5	...	168±16	133±16	22±4	139±5	221±17	137±5	50±3	40±3
2202335	378±8	...	161±17	148±23	61±5	1907±5	238±19	1001±5	319±5	231±5
1307713	650±17	...	170±48	2069±65	282±16	2736±31	1165±125	3066±22	826±208	704±177
2204417	466±32	...	327±90	418±104	92±13	1401±27	731±66	934±23	371±15	278±14

Note—Emission line fluxes for our outflow sample. Column 1: Unique ID of the GAMA object. Columns 2–11: The emission-line fluxes and their errors in units of 10^{-17} erg s^{-1} cm^{-2}. No extinction correction has been applied. The subscripts n and b refer to the narrow and broad components, respectively. We do not show the flux values of the [O III]λ4959 and the [N II]λ4548 lines, since their fluxes are fixed to be weaker by factors of 3. A three-dot ellipsis indicates no line is detected, or the emission lines do not meet our reliable detection criteria. The entirety of Table 6 is published in the electronic edition of *The Astrophysical Journal*. We show a portion here to give information on its form and content.

Properties of the Outflow Candidates

We identify 398 galaxies with reliable ionized outflow signatures in their [O III]λ5007 line, which is $\sim$1% of our parent sample. In this section, we classify galaxies with outflows using narrow-line diagnostic diagrams, estimate BH masses for objects with detectable broad Hα emission, and determine the properties of both the outflows and their host galaxies. Additionally, we present findings on outflows in low-mass galaxies.

Narrow-line Diagnostic Diagrams

The harder radiation field of AGNs can result in higher fluxes of forbidden lines such as [N II]λ6583, [S II]$\lambda\lambda$6716, 6731, and [O I]λ6003 lines with respect to the Balmer lines. This enables us to separate AGNs and SF galaxies when these line ratios are plotted in two-dimensional narrow-line diagnostic diagrams.

We employ the [O III]/Hβ vs. [N II]/Hα Baldwin-Phillips-Terlevich (BPT) diagnostic diagram (Baldwin et al., 1981) to classify our outflow galaxies as shown in the left panel of Figure 22. In this diagram, the AGNs fall above the maximum starburst line from Kewley et al. (2006), while the SF objects occupy the area below the composite line from Kauffmann et al. (2003). Composite objects that fall between the two lines have both contributions from AGN and SF activity.

We only include objects with reliable emission line measurements relevant to this diagram, which is 394/398 of the outflow galaxies. We classify 79% of these objects as AGNs, 10% as composites, and 11% as SF-dominated galaxies. Therefore, the vast majority of our galaxies with outflow signatures also have AGN photoionization signatures in their spectra, which is in agreement with previous studies that found a higher incidence of outflows in AGNs than SF galaxies (e.g., Concas et al., 2017; Matzko et al., 2022). This result, in addition to the large outflow velocities we find for the AGNs/composites (see Section 4.3.1),

suggests that these outflows are predominantly driven by AGN feedback. For simplicity, we will refer to the AGNs and composites collectively as AGNs throughout the rest of the paper.

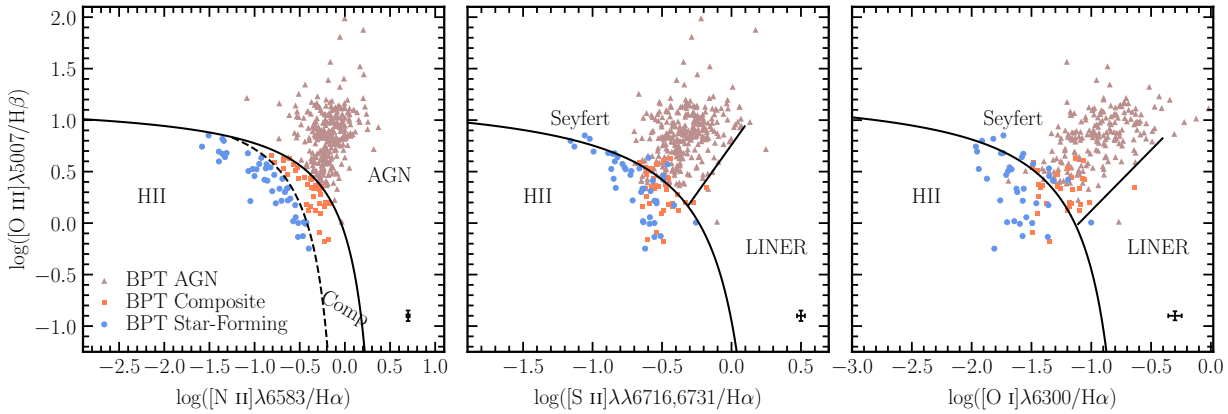

Figure 22: The left panel shows the [O III]/Hβ vs. [N II]/Hα narrow-line diagnostic diagram for our outflow candidates in the GAMA survey using the classification scheme summarized in Kewley et al. (2006). Here 394/398 of the outflow galaxies with reliable emission lines relevant to this diagram are plotted, of which 312 are AGNs (rosy brown triangles), 39 are composites (coral squares), and 43 are SF galaxies (cornflower blue circles). The middle and right panels show these objects in the [O III]/Hβ vs. [S II]/Hα and [O I]/Hα diagrams. Only galaxies with reliable emission lines are plotted in these panels. Characteristic error bars are located in the lower right region of each panel. See Section 4.1 for details.

We also plot the outflow galaxies in the [O III]/Hβ vs. [S II]/Hα and [O I]/Hα diagrams (Veilleux & Osterbrock, 1987) as shown in the middle and right panels of Figure 22. In these plots, the theoretical extreme starburst line from Kewley et al. (2001) separates the AGNs from SF galaxies, while the Seyfert/LINER line differentiates the Seyfert and low ionization nuclear emission region (LINER) objects. Among the BPT AGNs, ∼86% with reliable [S II] emission are located in the AGN region of the [S II]/Hα diagram. In the [O I]/Hα diagram, 62% of those with detected [O I] are classified as AGNs. Additionally, we find that 14% and 26% of the BPT-SF objects appear AGN-like in the [S II]/Hα and [O I]/Hα diagrams, respectively, while 9% are AGNs in both diagrams.

The small number of LINER galaxies in our outflow sample (7 in the [S II]/Hα and 7 the in [O I]/Hα diagrams) is in agreement with what Matzko et al. (2022) found and in

contrast with Hermosa Muñoz et al. (2022), where they found outflow signature in 50% of their LINER candidates. We note that Hermosa Muñoz et al. (2022) employ Integral Field Unit (IFU) data in their study which has a higher resolution than our sample and that of Matzko et al. (2022).

Broad Hα and BH Mass Estimates

The presence of a broad Hα line can be associated with rotating gas in the BLR around a BH. By utilizing the measured parameters of this line and employing standard virial techniques, we can estimate the mass of the central BH using the formula $M_{BH} \propto R_{BLR}\Delta V^2/G$. Here gas velocity comes from the broad line width and the radius of the BLR is known to scale with the broad line luminosity based on reverberation-mapped AGNs. However, in SF galaxies, broad Hα emission can be due to stellar activities such as supernovae, which can be transient and fade over time (e.g., Baldassare et al., 2016). Given this, we do not accept the broad Hα component in SF galaxies as a solid AGN indicator and do not estimate their BH mass.

As described in Section 3.4, we identify broad Hα emission in 206 galaxies with outflow signatures. The majority of these objects are classified as AGNs, with only 10 found among SF galaxies. The FWHM of the broad Hα lines varies from 501 to 8607 km s^{-1}. The median FWHM for AGNs is 1789 km s^{-1}, while for SF galaxies, it is 734 km s^{-1}. AGNs also display greater luminosities that scale from $10^{39.7-43.1}$ erg s^{-1}, with a median of $10^{41.4}$ erg s^{-1}, compared to the range of $10^{40.2-41.8}$ erg s^{-1} and a median of $10^{41.2}$ erg s^{-1} in the SF objects. We summarize these quantities for the AGNs in Table 7 and show their distributions in Figure 23.

We estimate the virial BH masses for broad-line AGNs using the following equation (Reines et al., 2013):

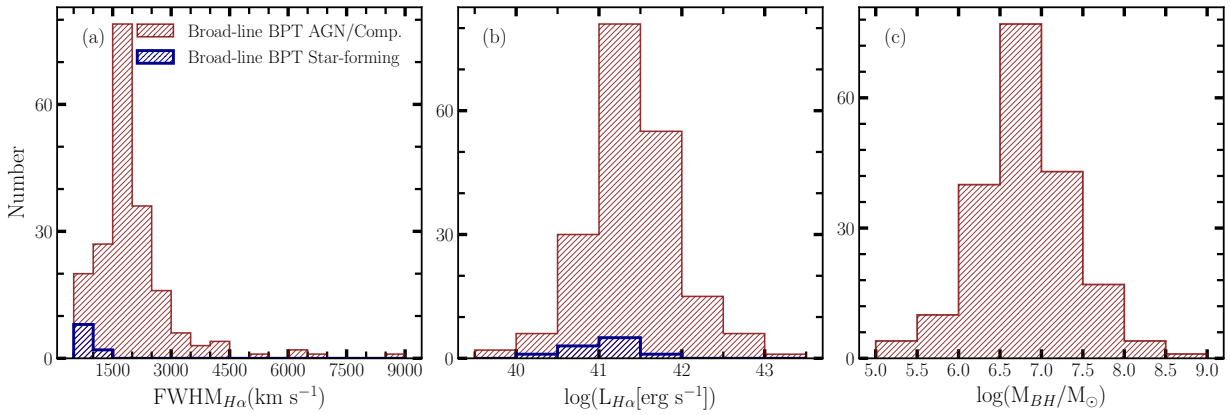

Figure 23: Distributions of Broad Hα emission parameters and BH mass. Panels (a) and (b) display the histograms of the FWHM and log luminosity of the broad Hα component for AGNs shown in maroon, and SF galaxies shown in blue. Virial BH mass distribution for the broad-line AGNs is plotted in panel (c). We estimate these BH masses using Equation (5) from Reines et al. (2013). Broad Hα emissions in star-forming objects are not considered strong indicators of AGNs, and we do not estimate virial BH masses for these galaxies. For further details, refer to Section 4.2.

$$\log(\frac{M_{BH}}{M_\odot}) = \log\epsilon + 6.57 + 0.47\log(\frac{L_{H\alpha}}{10^{42}\ \mathrm{erg\ s^{-1}}}) + 2.06\log(\frac{\mathrm{FWHM_{H\alpha}}}{10^{3}\ \mathrm{km\ s^{-1}}})$$

where $\epsilon = 1$ and $L_{H\alpha}$ represents the luminosity of the broad Hα line. The BH masses we calculate range from 10^5 to $10^{8.6}$ M$_\odot$, with a median value of $10^{6.8}$ M$_\odot$. These values are listed for each object in Table 7 and their distribution is shown in the last panel of Figure 23. We note that these BH masses are derived assuming negligible outflowing material in the BLR region. However, with the presence of outflows in this region, the reliability of this method has been debated (e.g., Collin et al., 2006; Vestergaard & Peterson, 2006) and alternative methods have been proposed (e.g., Everett, 2005; Murray & Chiang, 1995; Proga, 2007).

Outflow Properties

Outflow Velocity

As discussed in Section 3.3, W$_{80}$ measures the outflow velocity in our sample, which

Table 7: Broad-line AGNs

CATAID (1)	BPT Classification (2)	log $L(H\alpha)_b$ (3)	FWHM(Hα)$_b$ (4)	log M_{BH} (5)
1889137	Comp.	41.84	1474	6.8
1069351	AGN	41.58	1684	6.8
2132672	AGN	41.64	2281	7.1
1785686	AGN	42.23	2808	7.6
1890557	AGN	41.77	1774	7.0
1896259	AGN	41.55	1589	6.8
2379296	AGN	41.22	1952	6.8
1485133	AGN	41.48	1841	6.9
1982957	AGN	41.92	4065	7.8
1819774	AGN	41.19	1371	6.5

Note—Column 1: Unique ID of the GAMA object. Column 2: Classification of the object in the BPT diagram. Column 3: The luminosity of the broad Hα component in units of erg s^{-1}. Column 4: The width (FWHM) of the broad Hα component in units of km s^{-1}, corrected for instrumental resolution. Column 5: The virial BH mass in units of M$_\odot$ by assuming the broad Hα emission is associated with the BLR. We only include BPT-AGNs and composites in this table. See section 4.2 for more details. The entirety of Table 7 is published in the electronic edition of *The Astrophysical Journal*. We show a portion here to give information on its form and content.

varies from 327 to 2689 km s^{-1}. The AGNs exhibit higher outflow velocities, with a median of 936 km s^{-1}, while SF galaxies are found with a median of 655 km s^{-1}. For the AGN candidates with broad Hα detection, the median outflow velocity is slightly higher at 961 km s^{-1}, compared to 880 km s^{-1} for those without broad Hα lines. Histograms of these velocities for each galaxy classification are shown in panels (a) and (c) of Figure 24. Additionally, the outflow velocity for each object is detailed in Table 5.

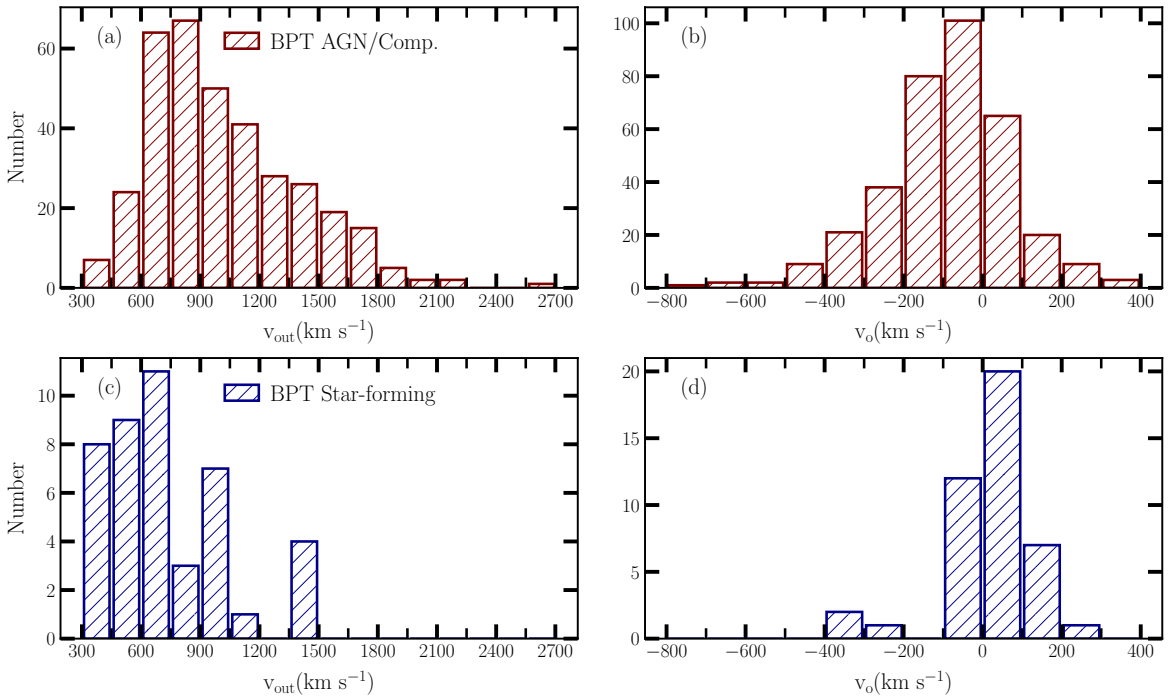

Figure 24: Outflow properties. *(a)–(b)*: Distributions of outflow velocity (v_{out}) and offset velocity (v_o) for the BPT-AGNs and composites in our outflow sample shown in maroon histograms. The medians of outflow velocity and offset velocity are 936 km s^{-1} and −84 km s^{-1}, respectively. *(c)–(d)*: Same as panels (a)–(b) except for the SF galaxies with outflow signatures plotted in blue histograms. Outflow and offset velocity median values are 655 km s^{-1} and 28 km s^{-1}, respectively. See Section 4.3 for more details.

Outflows in AGNs and SF galaxies have been observed with velocities ranging from a few hundred to thousands of km s^{-1} (e.g., Aravindan et al., 2023; Harrison et al., 2014; Matzko et al., 2022; Mullaney et al., 2013). Some studies suggest that velocities of at least 500

km/s are associated with AGN activity (Mullaney et al., 2013), as these require an outflow power that exceeds that of starbursts (Fabian, 2012). This is also related to the maximum linewidths observed in galaxy dynamics and mergers in high-redshift ultraluminous infrared galaxies (Harrison et al., 2012, and the references within). We find that ∼97% of the AGNs have outflow velocities of $W_{80} > 500$ km s^{-1}, indicating that AGN-driven mechanisms are responsible for the outflows in these galaxies.

Our results are consistent with the literature. The median outflow velocities in the starburst galaxies in Rupke et al. (2002, 2005) were ~ 300 km s^{-1}, while Hill & Zakamska (2014) and Rupke & Veilleux (2013) found median velocities of order ~ 600 km s^{-1} for their starburst objects. Matzko et al. (2022) found outflow velocities on the order 700 km s^{-1} for their AGNs and lower velocities with an average of 300 km s^{-1} for their SF galaxies. Harrison et al. (2012) found a median bulk outflow velocity of 780 km s^{-1} for their type 2 AGN sample while Mullaney et al. (2013) found a mean of 900 km s^{-1} for their type 1 AGNs. Zakamska & Greene (2014) found a median velocity of 752 km s^{-1} for their luminous obscured quasars.

Offset Velocity

The offset velocity v_0 in our sample, which is the separation between the [O III] line components, ranges from -779 to 386 km s^{-1}. The AGNs show a blueshifted median v_o of -84 km s^{-1}, while the SF objects exhibit a redshifted median of 28 km s^{-1}. We find that 32% of the outflows are redshifted ($v_0 > 0$), where the incidence of redshifted lines in AGNs is 28%, compared to 65% in SF galaxies. Furthermore, 27% of AGNs with broad Hα detection are found with redshifted second components, whereas 29% of AGNs without broad Hα have this feature. Histograms of the v_o for the AGNs and SF galaxies are shown in panels (b) and (d) of Figure 24, and Table 5 includes this velocity for each object.

The offset velocity is sensitive to dust extinction (Bae & Woo, 2016), and in the presence

of an obscured central region (like an AGN), the blueshifted broader component can trace outflows in the NLR around a BH. Hence, such lines are often attributed to an AGN origin (Harrison et al., 2012; Liu et al., 2020; Matzko et al., 2022). On the other hand, the redshifted outflow lines can be a consequence of the orientation of the galaxy to the line of sight (Bae & Woo, 2016), and have also been reported in AGNs (e.g., Crenshaw et al., 2010; Mullaney et al., 2013). Therefore, both the redshifted and blueshifted outflow components among our AGNs with velocities over 500 km s^{-1} likely signify AGN feedback. In contrast, stellar-driven outflows do not necessarily originate from the center of galaxies and can occur at any location, thus they generally are not affected by extinction (Aravindan et al., 2023) and are typically observed with symmetric outflow components (e.g., Concas et al., 2017; Davies et al., 2019; Matzko et al., 2022).

These results are consistent with previous studies that suggest mostly broad blueshifted outflow lines in AGNs and a more symmetric broad line in SF galaxies (e.g, Aravindan et al., 2023; Concas et al., 2017; Harrison et al., 2014; Manzano-King et al., 2019; Matzko et al., 2022). The ratio of our redshifted outflow lines is similar to the incidence ratio of 28% in Barth et al. (2008), while it is larger than the 6% in Greene & Ho (2005) and Crenshaw et al. (2010).

Host Galaxy Properties

We plot the stellar mass distribution of outflow hosts separated by their classifications in panels (a) and (d) of Figure 25. The lowest host galaxy mass belongs to an SF object with a stellar mass of $10^{8.1}$ $M_\odot$, while the highest mass is a BPT-AGN with a stellar mass of $10^{11.7}$ $M_\odot$. The median log galaxy mass for the SF galaxies and AGNs are 9.7 and 10.6 $M_\odot$, respectively. $\sim$ 96% of the AGNs have stellar masses $M_* > 10^{10}$ $M_\odot$, while 33% of the SF galaxies are within this mass range.

The redshift distribution of AGNs and SF galaxies can be found in panels (b) and (e)

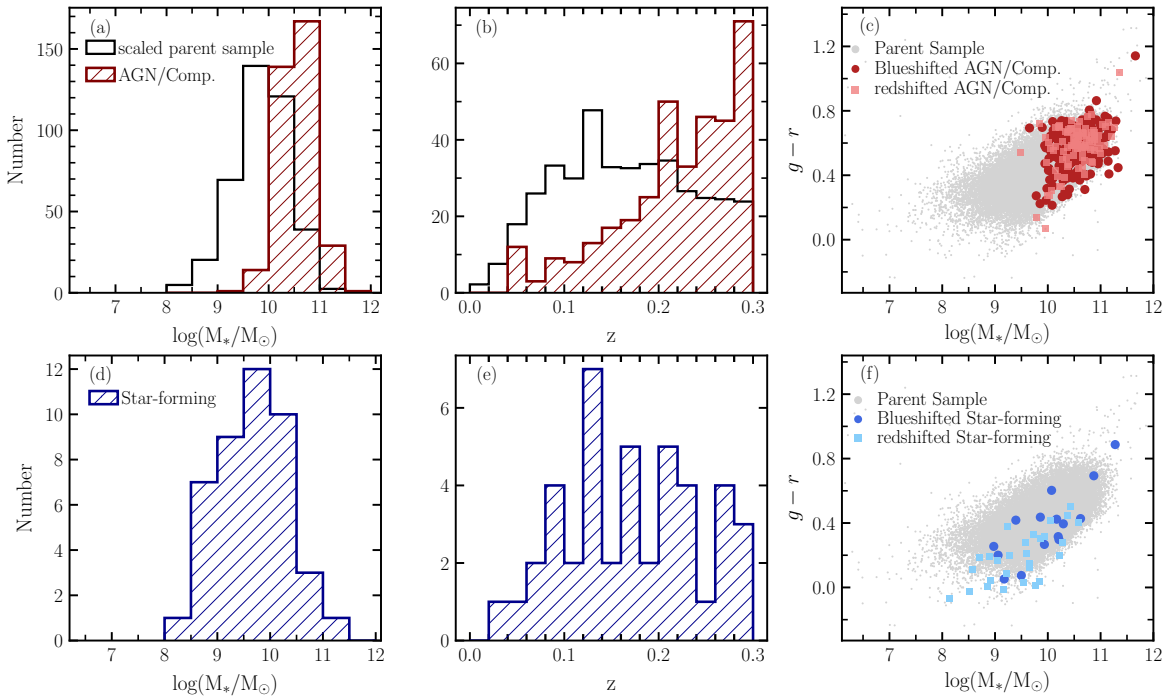

Figure 25: Host galaxy properties for the outflow candidates. *(a)–(c)*: Panels (a) and (b) show the distributions of host galaxy stellar mass and redshift (hashed maroon histograms) for AGNs/composites. Our parent sample (normalized to the number of outflow galaxies) is also shown as a black histogram. Panel (c) shows the $g-r$ vs. $\log(M_*/M_\odot)$ plot for AGNs. Here the distribution of the blueshifted and redshifted outflow components are displayed as red circles and pink squares, respectively. All values are adopted from `StellarMassesG02CFHTLS v24` and `StellarMassesGKV v24` tables (Bellstedt et al., 2020; Taylor et al., 2011). No noticeable difference between the host properties of the blueshifted and redshifted outflow lines can be seen. *(d)–(f)*: Same as panels (a)–(c) except for the SF galaxies with outflow signatures (hashed blue histograms). In panel f, the blueshifted and redshifted lines are shown as dark blue circles and light blue squares, respectively. See Section 4.4 for more details.

of Figure 25, respectively. We select objects with redshift z <0.3 by design to ensure the [S II] doublet is covered in the observed spectra. The median redshift for our AGNs and SF galaxies are 0.23 and 0.17, respectively.

We show the color-mass diagram for the AGNs in panel (c) of Figure 25. These objects are predominantly among more massive galaxies and follow a similar color range as the parent sample in the high mass range. There does not appear to be a significant difference between the AGN host galaxies with redshifted and blueshifted outflow lines. However, the median color of the galaxies with redshifted lines is 0.6 compared to the slightly bluer median color of 0.57 for the host galaxies with blueshifted lines.

The color-mass diagram for the SF galaxies is plotted in panel (f) of Figure 25. Here, the redshifted lines in the SF galaxies seem to be among less massive and bluer objects. The bluer color may indicate that the star formation has not been impacted by outflows (Aravindan et al., 2023). In contrast, the SF galaxies with blueshifted broad lines also extend to redder and higher masses.

Low-Mass Galaxies

While stellar feedback has been considered the main source of feedback in low-mass galaxies, theoretical models have attained contrasting results on the extent of AGN feedback and the impact of SF-driven outflows in them (Anglés-Alcázar et al., 2017; Barai & de Gouveia Dal Pino, 2019; Dashyan et al., 2018; Koudmani et al., 2021, 2019; Sharma et al., 2020; Trebitsch et al., 2018). Given the recent observations of AGNs in low-mass/dwarf galaxies (e.g., Molina et al., 2021b; Moran et al., 2014; Reines et al., 2013; Salehirad et al., 2022) as well as the evidence of outflows in this mass range (Aravindan et al., 2023; Liu et al., 2020), it is important to search for AGN feedback specifically in the low-mass regime.

In this work, we identify 45 galaxies with masses $M_* < 10^{10}$ $M_\odot$ among the outflow candidates, of which 11 are BPT AGNs, 4 are composites, and 29 are classified as SF galaxies.

The remaining low-mass galaxy has an unreliable Hα measurement and thus is not classified. All the AGNs/composites are among the Salehirad et al. (2022) sample. We have found that while AGN hosts are more common in our overall outflow sample, star-forming galaxies are the primary hosts of outflows in our low-mass galaxies. However, selection effects could contribute to this finding. For example, the BPT diagram has difficulty distinguishing AGNs in the low-mass range, and low-metallicity AGNs can overlap with low-metallicity starbursts in this diagram (Groves et al., 2006).

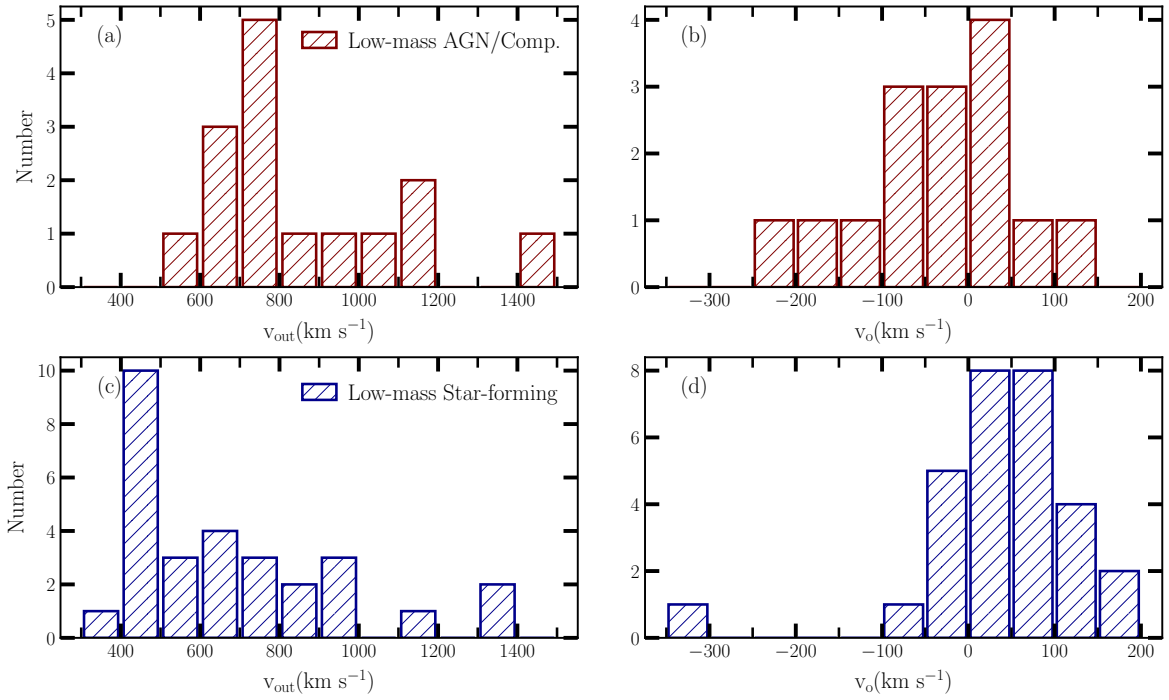

Figure 26: Same as Figure 24, but for the low-mass outflow galaxies with masses $M_* < 10^{10}$ $M_\odot$. The medians of outflow and offset velocities for AGNs and composites are 777 and -46 km s^{-1}, respectively, while SF galaxies have a lower median outflow velocity of 609 km s^{-1} and a redshifted median offset velocity of 42 km s^{-1}. See Section 4.5 for more details.

The outflow velocities among the low-mass galaxies span a range of 327 to 1449 km s^{-1}, where the median outflow velocity for the AGNs and SF galaxies are 777 km s^{-1} and

609 km s^{-1}, respectively. Distributions of outflow velocities are shown in panels (a) and (c) of Figure 26. Our median values are higher than what Aravindan et al. (2023) and Liu et al. (2020) found for their SF and AGN samples (484 km s^{-1}) and less than the weighted averages reported in Manzano-King et al. (2019).

The offset velocities vary from -303 to 191 km s^{-1}, with a median of -46 km s^{-1} for AGNs and a median of 42 km s^{-1} for SF galaxies. One of the SF objects is found with a blueshifted velocity of ~ -300 km s^{-1}, where the [O III] line components have similar widths and resemble the line profile shown in panel (d) of Figure 19. We display the distributions of offset velocities for low-mass galaxies in panels (b) and (d) of Figure 26. Previous studies such as Manzano-King et al. (2019) found an offset velocity of -108 km s^{-1} for their AGN candidates and 5 km s^{-1} for their SF galaxies. Liu et al. (2020) found the average offset velocity of -64 km s^{-1} for their AGN sample, while Aravindan et al. (2023) found an average offset velocity of 0 km s^{-1} for their SF galaxies, which was -60 km s^{-1} if only blueshifted regions were considered. If we include only the blueshifted outflow lines, our medians for AGNs and SF galaxies change to -62 and -34 km s^{-1}, respectively.

Outflow signatures among our low-mass AGNs suggest that BH feedback exists in this mass range and should be considered as a factor in the evolution models of low-mass galaxies. Moreover, we find that outflows in AGNs are typically faster and blueshifted compared to SF galaxies, which can deplete ISM from gas and quench SF (Bradford et al., 2018) or trigger SF (Schutte & Reines, 2022), again suggesting the importance of AGN feedback in low-mass galaxies.

Summary and Conclusions

In this work, we systematically search for ionized outflow signatures in the [O III]$\lambda\lambda 4959, 5007$ doublet emission line. Our parent sample consists of 39,612 galaxies with redshift $z < 0.3$ from the GAMA survey. We identify double-component features that may signify outflows

in 398 galaxies, of which 45 are among low-mass galaxies with stellar masses $M_* < 10^{10}$ $M_\odot$. Only 8 of our outflow candidates have SDSS spectra, and thus we are presenting novel outflow candidates in this work.

We classify our outflow galaxies using the BPT diagram as shown in the left panel of Figure 22. Of the 394 galaxies with reliable measurements of the emission lines used in this diagram, 79% are AGNs, 10% are composites, and the remaining 11% are SF-dominated galaxies. Thus, the majority of our outflow sample is among galaxies with at least some level of AGN activity, which is consistent with previous work that finds a higher incidence of outflows in AGNs (e.g., Concas et al., 2017).

We also search for broad Hα emission and identify 206 galaxies, of which 196 are among AGNs/composites and 10 are SF galaxies. We estimate virial BH masses for the AGNs and composites using the broad Hα line parameters, ranging from 10^5 to $10^{8.6}$ $M_\odot$. Distributions of the broad Hα parameters and BH masses are shown in Figure 23.

We identify outflow components that are symmetric, blueshifted, and redshifted with respect to the systemic components of the [O III] lines. In $\sim 9\%$ of the outflow candidates, either two peaks are visible by eye or they have components with similar widths (see Figure 19 and Section 3.2). These lines can represent double-peaked lines, which can be produced by the disk rotation of the NLR around a single BH, biconical outflows, or distinct NLRs in merging AGNs (e.g., Shen et al., 2011).

We adopt W_{80} to measure the outflow velocities as shown in Figure 20 and find generally faster outflow velocities in BPT-AGNs and composites with a median velocity of 936 km s^{-1} compared to 655 km s^{-1} in the SF galaxies. Moreover, the majority of the AGNs/composites have outflow velocities $W_{80} > 500$ km s^{-1}, which is considered the limit that AGN feedback due to outflows is noteworthy (Fabian, 2012), and indicates AGN-driven mechanisms for the outflows in these galaxies.

The offset velocity between the systemic and outflow components of the [O III]λ5007

line varies from ~ -780 to 390 km s^{-1} (see Section 4.3.2). The outflows in AGNs and composites have a blueshifted median offset velocity of -84 km s^{-1}, while the SF objects have a redshifted median of 28 km s^{-1}. The incidence of redshifted outflows in our sample is 32%, where the incidence among AGNs/composites and SF-dominated galaxies are 28% and 65%, respectively.

Host galaxy properties for our outflow sample are listed in Table 5 and their distributions are shown in Figure 25. The host galaxy stellar masses of our outflow sample range from $10^{8.1}$ to $10^{11.7}$ M$_\odot$, where the median galaxy mass of the AGNs/composites and SF galaxies are $10^{10.6}$ and $10^{9.7}$ M$_\odot$, respectively. 96% of the AGNs have stellar masses M$_* > 10^{10}$, while only 33% of the SF galaxies are within this mass range. The BPT AGNs and composites are predominantly among massive galaxies and follow a similar color range to our parent sample, while the SF objects are among lower-mass and bluer objects.

Of the 45 low-mass galaxies that exhibit outflow signatures, 11 are classified as AGNs, 4 are composites, and 29 are SF galaxies. Outflows in the low-mass AGNs/composites are faster and blueshifted with median outflow and offset velocities of 777 km s^{-1} and -46 km s^{-1}. On the other hand, outflows in SF objects are found with a median outflow velocity of 609 km s^{-1} and a redshifted median offset velocity of 42 km s^{-1}, see Figure 26. The existence of faster-moving outflows in low-mass AGNs suggests that AGN feedback is noteworthy in these objects and should be considered a factor in galaxy evolution models in this mass range.

Identifying these novel ionized gas outflows is the first step in furthering our knowledge of feedback and its impact on the evolution of the central BHs and their host galaxies. Future studies of the molecular and neutral gas outflows associated with these objects can help us understand the mechanisms involved in producing them and how they are distributed throughout galaxies. The *James Webb Space Telescope* could be used to trace the molecular phase of the outflows by observing the mid-infrared rotational and rovibrational transitions

of H_2, which can be further explored as a tracer of AGN feedback (Cicone et al., 2018). Studying the radio luminosity of these targets allows us to explore whether the mechanical energy from a radio jet is responsible for these outflows. From the X-ray spectra and the bolometric luminosity of the AGNs, we can investigate if the energy of radiatively driven outflows by AGNs is sufficient to couple with ISM and produce them or if the radiation from stellar processes is the more likely scenario. Finally, follow-up integral field spectroscopy observations of these galaxies would allow us to trace the kinematics and morphology of outflows on pc to kpc scales and investigate the impact on star formation.

We thank the anonymous reviewer for their helpful comments and suggestions that greatly improved this work. AER acknowledges support for this work provided by NASA through EPSCoR grant number 80NSSC20M0231 and the NSF through CAREER award 2235277. The work of M.M. is supported in part through a fellowship sponsored by the Willard L. Eccles Foundation.

GAMA is a joint European-Australasian project based around a spectroscopic campaign using the Anglo-Australian Telescope. The GAMA input catalogue is based on data taken from the Sloan Digital Sky Survey and the UKIRT Infrared Deep Sky Survey. Complementary imaging of the GAMA regions is being obtained by a number of independent survey programmes including GALEX MIS, VST KiDS, VISTA VIKING, WISE, Herschel-ATLAS, GMRT and ASKAP providing UV to radio coverage. GAMA is funded by the STFC (UK), the ARC (Australia), the AAO, and the participating institutions. The GAMA website is http://www.gama-survey.org/. Based on observations made with ESO Telescopes at the La Silla Paranal Observatory under programme ID 179.A-2004. Based on observations made with ESO Telescopes at the La Silla Paranal Observatory under programme ID 177.A-3016.

CONCLUSION

In this dissertation, I presented novel scientific findings that help further our understanding of supermassive black hole origins and their impact on host galaxies. The research used the spectroscopic observations from the less explored GAMA survey as presented in chapters 2 and 3. The key discoveries of this study include 1) identifying galaxies that host accreting black holes in low-mass galaxies utilizing multiple optical diagnostics, and 2) detecting AGN-driven outflows in the low-mass regime that are generally faster than those in the star-forming-dominated galaxies.

Over the past decade, the influx of active massive black hole observations in dwarf/low-mass galaxies has opened a new pathway to constrain the supermassive black hole seed mechanisms, ultimately helping to uncover the mystery of their origin. We analyzed spectra of 23,460 low-mass ($M_* < 10^{10}\ M_\odot$) GAMA galaxies by initially fitting the stellar continuum and absorption lines. We then fitted the emission lines of interest after subtracting the models found using the `pPXF` package and stellar synthesis population templates. We identified 388 new AGN candidates by employing the [O III]/Hβ versus [N II]/Hα and He II/Hβ versus [N II]/Hα narrow-line diagnostic diagrams as well as searching for [Ne V] and [Fe X] coronal emission lines. Additionally, we observed broad Hα emission in 47 and found virial black hole mass estimates for these galaxies. By employing this multi-diagnostic approach, we compiled a more comprehensive sample of AGNs, each mostly unique to their respective diagnostics. Furthermore, the host galaxies of the AGNs aligned better with the general trend of the parent sample. This work provided an entirely new sample of low-mass active galaxies, increasing the total number of known AGNs within this mass range and extending the search for AGNs to deeper southern regions and higher redshift galaxies. We found an AGN fraction of $\sim 1\%$, which is a lower limit on the BH occupation fraction in this mass range, and has implications for the origin of BH seeds.

We identified outflow signatures in the spectra of $\sim$ 40,000 GAMA galaxies with available masses. We searched for a second velocity component in the [O III]$\lambda\lambda$4959, 5007 doublet line profile, typically detected as broadening or asymmetry in each of these lines. Using the fitted line parameters, we measured the outflow properties (i.e., outflow and offset velocities). We found that 398 galaxies in this survey show outflow activity, of which 45 are among low-mass galaxies. The outflows were typically faster and blueshifted in AGNs compared to those dominated by star formation. This result was particularly important in the low-mass range since the impact of AGN-driven outflows is still a topic of debate. Our results highlight the significant role of AGN feedback within low-mass galaxies and provide observational constraints for theoretical models.

To advance our knowledge of supermassive black hole formation and its impact on the evolution of galaxies, it is crucial to discover as many AGNs as possible in dwarf galaxies and to conduct further research on AGN feedback. The work presented in this dissertation provided a new sample of galaxies with AGN activity, with implications for the black hole fraction in the low-mass/dwarf galaxy range. It also indicated that AGN feedback is strong enough to influence host galaxy evolution in low-mass galaxies, emphasized by faster outflows in AGNs than in star-forming objects. Yet, despite a decade of observations in this regime, the demographics and influence of massive black holes in these galaxies remain poorly understood. Follow-up observations of my samples can address these gaps, and I have contributed to two such efforts. In 2023, I helped develop a successful proposal led by Professor Jenny Greene (Princeton University), securing two nights on the Magellan Baade Telescope. Selecting galaxies from my sample with broad Hα emission or hints thereof, Dr. Megan Sturm used virial black hole mass estimates and stellar velocity dispersions to populate the low-mass end of black hole-galaxy evolution diagrams. Additionally, as co-investigator on a JWST-Chandra proposal by Dr. Amy Reines, I helped select 10 dwarf galaxies with broad Hα emission to probe X-ray AGNs and expand scaling relations;

observations are forthcoming. High-resolution integral field unit observations of our outflow sample could further reveal outflow morphology and kinematics, while radio and X-ray studies might identify their energy sources. Upcoming multi-wavelength facilities promise more progress: JWST infrared observations can distinguish AGN from stellar emission using color-color diagrams and coronal lines; the Square Kilometer Array and next-generation VLA could detect optically hidden black holes; Lynx X-ray observations could provide detailed views of nearby and distant dwarfs; the Vera C. Rubin Observatory will spot variable AGNs; and the Laser Interferometer Space Antenna might constrain seed mechanisms via gravitational waves from $\sim 10^4 - 10^7 M\odot$ mergers. Together, these efforts signal a major leap in unraveling supermassive black hole seeds and their galactic roles.

REFERENCES CITED

Alexander, D. M., Swinbank, A. M., Smail, I., McDermid, R., & Nesvadba, N. P. H. 2010, MNRAS, 402, 2211, doi: 10.1111/j.1365-2966.2009.16046.x

Anglés-Alcázar, D., Faucher-Giguère, C.-A., Quataert, E., et al. 2017, MNRAS, 472, L109, doi: 10.1093/mnrasl/slx161

Antonini, F., Gieles, M., & Gualandris, A. 2019, MNRAS, 486, 5008, doi: 10.1093/mnras/stz1149

Aravindan, A., Liu, W., Canalizo, G., et al. 2023, ApJ, 950, 33, doi: 10.3847/1538-4357/acca7c

Bae, H.-J., & Woo, J.-H. 2016, ApJ, 828, 97, doi: 10.3847/0004-637X/828/2/97

Baldassare, V. F., Geha, M., & Greene, J. 2018, ApJ, 868, 152, doi: 10.3847/1538-4357/aae6cf

Baldassare, V. F., Reines, A. E., Gallo, E., & Greene, J. E. 2015, ApJ Lett., 809, L14, doi: 10.1088/2041-8205/809/1/L14

—. 2017, ApJ, 836, 20, doi: 10.3847/1538-4357/836/1/20

Baldassare, V. F., Reines, A. E., Gallo, E., et al. 2016, ApJ, 829, 57, doi: 10.3847/0004-637X/829/1/57

Baldry, I. K., Driver, S. P., Loveday, J., et al. 2012, MNRAS, 421, 621, doi: 10.1111/j.1365-2966.2012.20340.x

Baldry, I. K., Liske, J., Brown, M. J. I., et al. 2018, MNRAS, 474, 3875, doi: 10.1093/mnras/stx3042

Baldwin, J. A., Phillips, M. M., & Terlevich, R. 1981, PASP, 93, 5, doi: 10.1086/130766

Balmaverde, B., Marconi, A., Brusa, M., et al. 2016, Astronomy and Astrophysics, 585, A148, doi: 10.1051/0004-6361/201526694

Barai, P., & de Gouveia Dal Pino, E. M. 2019, MNRAS, 487, 5549, doi: 10.1093/mnras/stz1616

Barth, A. J., Greene, J. E., & Ho, L. C. 2008, AJ, 136, 1179, doi: 10.1088/0004-6256/136/3/1179

Begelman, M. C., Volonteri, M., & Rees, M. J. 2006, MNRAS, 370, 289, doi: 10.1111/j.1365-2966.2006.10467.x

Bellovary, J., Volonteri, M., Governato, F., et al. 2011, ApJ, 742, 13, doi: 10.1088/0004-637X/742/1/13

Bellstedt, S., Driver, S. P., Robotham, A. S. G., et al. 2020, MNRAS, 496, 3235, doi: 10.1093/mnras/staa1466

Benson, A. J., Bower, R. G., Frenk, C. S., et al. 2003, ApJ, 599, 38, doi: 10.1086/379160

Bizyaev, D., Chen, Y.-M., Shi, Y., et al. 2022, MNRAS, 516, 3092, doi: 10.1093/mnras/stac2439

Blandford, R., Meier, D., & Readhead, A. 2019, Annual Review of Astronomy and Astrophysics, 57, 467, doi: 10.1146/annurev-astro-081817-051948

Bower, R. G., Benson, A. J., Malbon, R., et al. 2006, MNRAS, 370, 645, doi: 10.1111/j.1365-2966.2006.10519.x

Bradford, J. D., Geha, M. C., Greene, J. E., Reines, A. E., & Dickey, C. M. 2018, ApJ, 861, 50, doi: 10.3847/1538-4357/aac88d

Bromm, V., & Yoshida, N. 2011, Annual Review of Astronomy and Astrophysics, 49, 373, doi: 10.1146/annurev-astro-081710-102608

Bruzual, G., & Charlot, S. 2003, MNRAS, 344, 1000, doi: 10.1046/j.1365-8711.2003.06897.x

Cann, J. M., Satyapal, S., Abel, N. P., et al. 2019, ApJ Lett., 870, L2, doi: 10.3847/2041-8213/aaf88d

Cappellari, M. 2017, MNRAS, 466, 798, doi: 10.1093/mnras/stw3020

Carniani, S., Marconi, A., Maiolino, R., et al. 2015, Astronomy and Astrophysics, 580, A102, doi: 10.1051/0004-6361/201526557

Cazzoli, S., Arribas, S., Colina, L., et al. 2014, Astronomy and Astrophysics, 569, A14, doi: 10.1051/0004-6361/201323296

Cerqueira-Campos, F. C., Rodríguez-Ardila, A., Riffel, R., et al. 2021, MNRAS, 500, 2666, doi: 10.1093/mnras/staa3320

Chilingarian, I. V., Katkov, I. Y., Zolotukhin, I. Y., et al. 2018, ApJ, 863, 1, doi: 10.3847/1538-4357/aad184

Churazov, E., Sazonov, S., Sunyaev, R., et al. 2005, MNRAS, 363, L91, doi: 10.1111/j.1745-3933.2005.00093.x

Cicone, C., Brusa, M., Ramos Almeida, C., et al. 2018, Nature Astronomy, 2, 176, doi: 10.1038/s41550-018-0406-3

Cicone, C., Feruglio, C., Maiolino, R., et al. 2012, Astronomy and Astrophysics, 543, A99, doi: 10.1051/0004-6361/201218793

Cicone, C., Maiolino, R., Sturm, E., et al. 2014, Astronomy and Astrophysics, 562, A21, doi: 10.1051/0004-6361/201322464

Collin, S., Kawaguchi, T., Peterson, B. M., & Vestergaard, M. 2006, Astronomy and Astrophysics, 456, 75, doi: 10.1051/0004-6361:20064878

Concas, A., Popesso, P., Brusa, M., et al. 2017, Astronomy and Astrophysics, 606, A36, doi: 10.1051/0004-6361/201629519

Conti, P. S. 1991, ApJ, 377, 115, doi: 10.1086/170340

Crenshaw, D. M., Schmitt, H. R., Kraemer, S. B., Mushotzky, R. F., & Dunn, J. P. 2010, ApJ, 708, 419, doi: 10.1088/0004-637X/708/1/419

Cresci, G., Marconi, A., Zibetti, S., et al. 2015, Astronomy and Astrophysics, 582, A63, doi: 10.1051/0004-6361/201526581

Croton, D. J., Springel, V., White, S. D. M., et al. 2006, MNRAS, 365, 11, doi: 10.1111/j.1365-2966.2005.09675.x

Czerny, B., & Hryniewicz, K. 2011, Astronomy and Astrophysics, 525, L8, doi: 10.1051/0004-6361/201016025

Dashyan, G., Silk, J., Mamon, G. A., Dubois, Y., & Hartwig, T. 2018, MNRAS, 473, 5698, doi: 10.1093/mnras/stx2716

Davies, R. L., Förster Schreiber, N. M., Übler, H., et al. 2019, ApJ, 873, 122, doi: 10.3847/1538-4357/ab06f1

Devecchi, B., & Volonteri, M. 2009, ApJ, 694, 302, doi: 10.1088/0004-637X/694/1/302

Dey, A., Schlegel, D. J., Lang, D., et al. 2019, AJ, 157, 168, doi: 10.3847/1538-3881/ab089d

Dong, X.-B., Ho, L. C., Yuan, W., et al. 2012, ApJ, 755, 167, doi: 10.1088/0004-637X/755/2/167

Driver, S. P., Bellstedt, S., Robotham, A. S. G., et al. 2022, MNRAS, 513, 439, doi: 10.1093/mnras/stac472

Edge, A., Sutherland, W., Kuijken, K., et al. 2013, The Messenger, 154, 32

Ellison, S. L., Wong, T., Sánchez, S. F., et al. 2021, MNRAS, 505, L46, doi: 10.1093/mnrasl/slab047

Everett, J. E. 2005, ApJ, 631, 689, doi: 10.1086/432678

Fabian, A. C. 2012, Annual Review of Astronomy and Astrophysics, 50, 455, doi: 10.1146/annurev-astro-081811-125521

Ferrarese, L., & Merritt, D. 2000, ApJ Lett., 539, L9, doi: 10.1086/312838

Feruglio, C., Maiolino, R., Piconcelli, E., et al. 2010, Astronomy and Astrophysics, 518, L155, doi: 10.1051/0004-6361/201015164

Filippenko, A. V., & Ho, L. C. 2003, ApJ Lett., 588, L13, doi: 10.1086/375361

Filippenko, A. V., & Sargent, W. L. W. 1988, ApJ, 324, 134, doi: 10.1086/165886

—. 1989, ApJ Lett., 342, L11, doi: 10.1086/185472

Fluetsch, A., Maiolino, R., Carniani, S., et al. 2021, MNRAS, 505, 5753, doi: 10.1093/mnras/stab1666

Fryer, C. L., Woosley, S. E., & Heger, A. 2001, ApJ, 550, 372, doi: 10.1086/319719

Fu, Y., Cappellari, M., Mao, S., et al. 2023, MNRAS, 524, 5827, doi: 10.1093/mnras/stad2214

García-Lorenzo, B., Márquez, I., Barrera-Ballesteros, J. K., et al. 2015, Astronomy and Astrophysics, 573, A59, doi: 10.1051/0004-6361/201423485

Geach, J. E., Tremonti, C., Diamond-Stanic, A. M., et al. 2018, ApJ Lett., 864, L1, doi: 10.

3847/2041-8213/aad8b6

Gebhardt, K., Bender, R., Bower, G., et al. 2000, ApJ Lett., 539, L13, doi: 10.1086/312840

Giersz, M., Leigh, N., Hypki, A., Lützgendorf, N., & Askar, A. 2015, MNRAS, 454, 3150, doi: 10.1093/mnras/stv2162

Gilli, R., Vignali, C., Mignoli, M., et al. 2010, Astronomy and Astrophysics, 519, A92, doi: 10.1051/0004-6361/201014039

Gordon, Y. A., Owers, M. S., Pimbblet, K. A., et al. 2017, MNRAS, 465, 2671, doi: 10.1093/mnras/stw2925

Goulding, A. D., & Alexander, D. M. 2009, MNRAS, 398, 1165, doi: 10.1111/j.1365-2966.2009.15194.x

Greene, J. E., & Ho, L. C. 2004, ApJ, 610, 722, doi: 10.1086/421719

—. 2005, ApJ, 627, 721, doi: 10.1086/430590

—. 2007, ApJ, 670, 92, doi: 10.1086/522082

Greene, J. E., Strader, J., & Ho, L. C. 2020, Annual Review of Astronomy and Astrophysics, 58, 257, doi: 10.1146/annurev-astro-032620-021835

Groves, B. A., Heckman, T. M., & Kauffmann, G. 2006, MNRAS, 371, 1559, doi: 10.1111/j.1365-2966.2006.10812.x

Gültekin, K., Richstone, D. O., Gebhardt, K., et al. 2009, ApJ, 698, 198, doi: 10.1088/0004-637X/698/1/198

Guolo-Pereira, M., Ruschel-Dutra, D., Storchi-Bergmann, T., et al. 2021, MNRAS, 502, 3618, doi: 10.1093/mnras/stab245

Habouzit, M., Volonteri, M., & Dubois, Y. 2017, MNRAS, 468, 3935, doi: 10.1093/mnras/stx666

Haiman, Z., & Loeb, A. 1998, ApJ, 503, 505, doi: 10.1086/306017

Harrison, C. M., Alexander, D. M., Mullaney, J. R., & Swinbank, A. M. 2014, MNRAS, 441, 3306, doi: 10.1093/mnras/stu515

Harrison, C. M., Alexander, D. M., Swinbank, A. M., et al. 2012, MNRAS, 426, 1073,

doi: 10.1111/j.1365-2966.2012.21723.x

Harrison, C. M., Alexander, D. M., Mullaney, J. R., et al. 2016, MNRAS, 456, 1195, doi: 10.1093/mnras/stv2727

Heckman, T. M., Miley, G. K., van Breugel, W. J. M., & Butcher, H. R. 1981, ApJ, 247, 403, doi: 10.1086/159050

Heckman, T. M., & Thompson, T. A. 2017, arXiv e-prints, arXiv:1701.09062, doi: 10.48550/arXiv.1701.09062

Hermosa Muñoz, L., Márquez, I., Cazzoli, S., Masegosa, J., & Agís-González, B. 2022, Astronomy and Astrophysics, 660, A133, doi: 10.1051/0004-6361/202142629

Heymans, C., Van Waerbeke, L., Miller, L., et al. 2012, MNRAS, 427, 146, doi: 10.1111/j.1365-2966.2012.21952.x

Hill, M. J., & Zakamska, N. L. 2014, MNRAS, 439, 2701, doi: 10.1093/mnras/stu123

Ho, L. C. 2008, Annual Review of Astronomy and Astrophysics, 46, 475, doi: 10.1146/annurev.astro.45.051806.110546

Ho, L. C., Filippenko, A. V., & Sargent, W. L. W. 1997, ApJ, 487, 568, doi: 10.1086/304638

Hopkins, P. F., Hernquist, L., Cox, T. J., et al. 2006, ApJ Supp., 163, 1, doi: 10.1086/499298

Inayoshi, K., Visbal, E., & Haiman, Z. 2020, Annual Review of Astronomy and Astrophysics, 58, 27, doi: 10.1146/annurev-astro-120419-014455

Izotov, Y. I., Noeske, K. G., Guseva, N. G., et al. 2004, Astronomy and Astrophysics, 415, L27, doi: 10.1051/0004-6361:20040006

Kauffmann, G., Heckman, T. M., Tremonti, C., et al. 2003, MNRAS, 346, 1055, doi: 10.1111/j.1365-2966.2003.07154.x

Kewley, L. J., Dopita, M. A., Sutherland, R. S., Heisler, C. A., & Trevena, J. 2001, ApJ, 556, 121, doi: 10.1086/321545

Kewley, L. J., Groves, B., Kauffmann, G., & Heckman, T. 2006, MNRAS, 372, 961, doi: 10.1111/j.1365-2966.2006.10859.x

Kewley, L. J., Nicholls, D. C., & Sutherland, R. S. 2019, Annual Review of Astronomy and Astrophysics, 57, 511, doi: 10.1146/annurev-astro-081817-051832

Kimbro, E., Reines, A. E., Molina, M., Deller, A. T., & Stern, D. 2021, ApJ, 912, 89, doi: 10.3847/1538-4357/abec6a

Komossa, S., Zhou, H., Wang, T., et al. 2008, ApJ Lett., 678, L13, doi: 10.1086/588281

Kormendy, J., & Ho, L. C. 2013, Annual Review of Astronomy and Astrophysics, 51, 511, doi: 10.1146/annurev-astro-082708-101811

Kormendy, J., & Richstone, D. 1995, Annual Review of Astronomy and Astrophysics, 33, 581, doi: 10.1146/annurev.aa.33.090195.003053

Koudmani, S., Henden, N. A., & Sijacki, D. 2021, MNRAS, 503, 3568, doi: 10.1093/mnras/stab677

Koudmani, S., Sijacki, D., Bourne, M. A., & Smith, M. C. 2019, MNRAS, 484, 2047, doi: 10.1093/mnras/stz097

Kuijken, K., Heymans, C., Dvornik, A., et al. 2019, Astronomy and Astrophysics, 625, A2, doi: 10.1051/0004-6361/201834918

Lasota, J.-P. 2022, in Active Galactic Nuclei, ed. F. Combes, 101–153, doi: 10.1002/9781394163724.ch3

Liske, J., Baldry, I. K., Driver, S. P., et al. 2015, MNRAS, 452, 2087, doi: 10.1093/mnras/stv1436

Liu, W., Veilleux, S., Canalizo, G., et al. 2020, ApJ, 905, 166, doi: 10.3847/1538-4357/abc269

Lodato, G., & Natarajan, P. 2006, MNRAS, 371, 1813, doi: 10.1111/j.1365-2966.2006.10801.x

Loeb, A., & Rasio, F. A. 1994, ApJ, 432, 52, doi: 10.1086/174548

Madau, P., Rees, M. J., Volonteri, M., Haardt, F., & Oh, S. P. 2004, ApJ, 604, 484, doi: 10.1086/381935

Manzano-King, C. M., Canalizo, G., & Sales, L. V. 2019, ApJ, 884, 54, doi: 10.3847/1538-4357/ab4197

Marconi, A., & Hunt, L. K. 2003, ApJ Lett., 589, L21, doi: 10.1086/375804

Markevitch, M. 1998, ApJ, 504, 27, doi: 10.1086/306080

Martín-Navarro, I., & Mezcua, M. 2018, ApJ Lett., 855, L20, doi: 10.3847/2041-8213/aab103

Matzko, W., Satyapal, S., Ellison, S. L., et al. 2022, MNRAS, 514, 4828, doi: 10.1093/mnras/stac1506

McCarthy, I. G., Schaye, J., Ponman, T. J., et al. 2010, MNRAS, 406, 822, doi: 10.1111/j.1365-2966.2010.16750.x

McConnell, N. J., & Ma, C.-P. 2013, ApJ, 764, 184, doi: 10.1088/0004-637X/764/2/184

Menci, N., Fontana, A., Giallongo, E., Grazian, A., & Salimbeni, S. 2006, ApJ, 647, 753, doi: 10.1086/505528

Miller, M. C., & Davies, M. B. 2012, ApJ, 755, 81, doi: 10.1088/0004-637X/755/1/81

Molina, M., Eracleous, M., Barth, A. J., et al. 2018, ApJ, 864, 90, doi: 10.3847/1538-4357/aad5ed

Molina, M., Reines, A. E., Greene, J. E., Darling, J., & Condon, J. J. 2021a, ApJ, 910, 5, doi: 10.3847/1538-4357/abe120

Molina, M., Reines, A. E., Latimer, L. J., Baldassare, V., & Salehirad, S. 2021b, ApJ, 922, 155, doi: 10.3847/1538-4357/ac1ffa

Moran, E. C., Filippenko, A. V., & Chornock, R. 2002, ApJ Lett., 579, L71, doi: 10.1086/345314

Moran, E. C., Shahinyan, K., Sugarman, H. R., Vélez, D. O., & Eracleous, M. 2014, AJ, 148, 136, doi: 10.1088/0004-6256/148/6/136

Morganti, R. 2017, Frontiers in Astronomy and Space Sciences, 4, 42, doi: 10.3389/fspas.2017.00042

Mortlock, D. J., Warren, S. J., Venemans, B. P., et al. 2011, Nature, 474, 616, doi: 10.1038/nature10159

Mullaney, J. R., Alexander, D. M., Fine, S., et al. 2013, MNRAS, 433, 622, doi: 10.1093/mnras/stt751

Müller-Sánchez, F., Comerford, J. M., Nevin, R., et al. 2015, ApJ, 813, 103, doi: 10.1088/0004-637X/813/2/103

Murray, N., & Chiang, J. 1995, ApJ Lett., 454, L105, doi: 10.1086/309775

Natarajan, P. 2014, General Relativity and Gravitation, 46, 1702, doi: 10.1007/s10714-014-1702-6

Negus, J., Comerford, J. M., Müller Sánchez, F., et al. 2021, arXiv e-prints, arXiv:2107.11631. https://arxiv.org/abs/2107.11631

Nevin, R., Comerford, J. M., Müller-Sánchez, F., Barrows, R., & Cooper, M. C. 2018, MNRAS, 473, 2160, doi: 10.1093/mnras/stx2433

Newville, M., Stensitzki, T., Allen, D. B., & Ingargiola, A. 2014, LMFIT: Non-Linear Least-Square Minimization and Curve-Fitting for Python, 0.8.0, Zenodo, doi: 10.5281/zenodo.11813

Nussbaumer, H., & Osterbrock, D. E. 1970, ApJ, 161, 811, doi: 10.1086/150585

Oetken, L. 1977, Astronomische Nachrichten, 298, 187, doi: https://doi.org/10.1002/asna.19772980312

Penny, S. J., Masters, K. L., Smethurst, R., et al. 2018, MNRAS, 476, 979, doi: 10.1093/mnras/sty202

Penston, M. V., Fosbury, R. A. E., Boksenberg, A., Ward, M. J., & Wilson, A. S. 1984, MNRAS, 208, 347, doi: 10.1093/mnras/208.2.347

Pereira-Santaella, M., Colina, L., García-Burillo, S., et al. 2018, Astronomy and Astrophysics, 616, A171, doi: 10.1051/0004-6361/201833089

Pier, E. A., & Voit, G. M. 1995, ApJ, 450, 628, doi: 10.1086/176171

Pogge, R. W. 1989, ApJ, 345, 730, doi: 10.1086/167945

Polimera, M. S., Kannappan, S. J., Richardson, C. T., et al. 2022, arXiv e-prints, arXiv:2204.03633. https://arxiv.org/abs/2204.03633

Portegies Zwart, S. F., Baumgardt, H., Hut, P., Makino, J., & McMillan, S. L. W. 2004, Nature, 428, 724, doi: 10.1038/nature02448

Prieto, M. A., Pérez García, A. M., & Rodríguez Espinosa, J. M. 2002, MNRAS, 329, 309, doi: 10.1046/j.1365-8711.2002.04985.x

Proga, D. 2007, ApJ, 661, 693, doi: 10.1086/515389

Reines, A. E. 2022, Nature Astronomy, 6, 26, doi: 10.1038/s41550-021-01556-0

Reines, A. E., Greene, J. E., & Geha, M. 2013, ApJ, 775, 116, doi: 10.1088/0004-637X/775/2/116

Reines, A. E., & Volonteri, M. 2015, ApJ, 813, 82, doi: 10.1088/0004-637X/813/2/82

Rosario, D. J., McGurk, R. C., Max, C. E., et al. 2011, ApJ, 739, 44, doi: 10.1088/0004-637X/739/1/44

Rupke, D. 2018, Galaxies, 6, 138, doi: 10.3390/galaxies6040138

Rupke, D. S., Veilleux, S., & Sanders, D. B. 2002, ApJ, 570, 588, doi: 10.1086/339789

—. 2005, ApJ Supp., 160, 115, doi: 10.1086/432889

Rupke, D. S. N., & Veilleux, S. 2011, ApJ Lett., 729, L27, doi: 10.1088/2041-8205/729/2/L27

—. 2013, ApJ, 768, 75, doi: 10.1088/0004-637X/768/1/75

Salehirad, S., Reines, A. E., & Molina, M. 2022, ApJ, 937, 7, doi: 10.3847/1538-4357/ac8876

—. 2025, ApJ, 979, 26, doi: 10.3847/1538-4357/ad9a57

Sartori, L. F., Schawinski, K., Treister, E., et al. 2015, MNRAS, 454, 3722, doi: 10.1093/mnras/stv2238

Satyapal, S., Vega, D., Dudik, R. P., Abel, N. P., & Heckman, T. 2008, ApJ, 677, 926, doi: 10.1086/529014

Saunders, W., Bridges, T., Gillingham, P., et al. 2004, in Society of Photo-Optical Instrumentation Engineers (SPIE) Conference Series, Vol. 5492, Ground-based Instrumentation for Astronomy, ed. A. F. M. Moorwood & M. Iye, 389–400, doi: 10.1117/12.550871

Schaerer, D., Contini, T., & Pindao, M. 1999, Astronomy and Astrophysics Supplement, 136, 35, doi: 10.1051/aas:1999197

Schaerer, D., Fragos, T., & Izotov, Y. I. 2019, Astronomy and Astrophysics, 622, L10, doi: 10.1051/0004-6361/201935005

Schaye, J., Crain, R. A., Bower, R. G., et al. 2015, MNRAS, 446, 521, doi: 10.1093/mnras/

stu2058

Schleicher, D. R. G. 2018, arXiv e-prints, arXiv:1807.06055. https://arxiv.org/abs/1807.06055

Schmidt, M., Hasinger, G., Gunn, J., et al. 1998, Astronomy and Astrophysics, 329, 495. https://arxiv.org/abs/astro-ph/9709144

Schutte, Z., & Reines, A. E. 2022, Nature, 601, 329, doi: 10.1038/s41586-021-04215-6

Sharma, R. S., Brooks, A. M., Somerville, R. S., et al. 2020, ApJ, 897, 103, doi: 10.3847/1538-4357/ab960e

Sharp, R., Saunders, W., Smith, G., et al. 2006, in Society of Photo-Optical Instrumentation Engineers (SPIE) Conference Series, Vol. 6269, Society of Photo-Optical Instrumentation Engineers (SPIE) Conference Series, ed. I. S. McLean & M. Iye, 62690G, doi: 10.1117/12.671022

Shen, Y. 2013, Bulletin of the Astronomical Society of India, 41, 61, doi: 10.48550/arXiv.1302.2643

Shen, Y., Liu, X., Greene, J. E., & Strauss, M. A. 2011, ApJ, 735, 48, doi: 10.1088/0004-637X/735/1/48

Shirazi, M., & Brinchmann, J. 2012, MNRAS, 421, 1043, doi: 10.1111/j.1365-2966.2012.20439.x

Silk, J. 2013, ApJ, 772, 112, doi: 10.1088/0004-637X/772/2/112

Silk, J., & Rees, M. J. 1998, Astronomy and Astrophysics, 331, L1, doi: 10.48550/arXiv.astro-ph/9801013

Smith, G., Brzeski, J., Miziarski, S., et al. 2004, in Society of Photo-Optical Instrumentation Engineers (SPIE) Conference Series, Vol. 5495, Astronomical Structures and Mechanisms Technology, ed. J. Antebi & D. Lemke, 348–359, doi: 10.1117/12.551004

Smith, N., Silverman, J. M., Chornock, R., et al. 2009, ApJ, 695, 1334, doi: 10.1088/0004-637X/695/2/1334

Somerville, R. S., Hopkins, P. F., Cox, T. J., Robertson, B. E., & Hernquist, L. 2008, MNRAS, 391, 481, doi: 10.1111/j.1365-2966.2008.13805.x

Springel, V., Di Matteo, T., & Hernquist, L. 2005, MNRAS, 361, 776, doi: 10.1111/j.

1365-2966.2005.09238.x

Stasińska, G., Cid Fernandes, R., Mateus, A., Sodré, L., & Asari, N. V. 2006, MNRAS, 371, 972, doi: 10.1111/j.1365-2966.2006.10732.x

Stockton, A. 1976, ApJ Lett., 205, L113, doi: 10.1086/182102

Taylor, E. N., Hopkins, A. M., Baldry, I. K., et al. 2011, MNRAS, 418, 1587, doi: 10.1111/j.1365-2966.2011.19536.x

Tollerud, E. J., Boylan-Kolchin, M., Barton, E. J., Bullock, J. S., & Trinh, C. Q. 2011, ApJ, 738, 102, doi: 10.1088/0004-637X/738/1/102

Trebitsch, M., Volonteri, M., Dubois, Y., & Madau, P. 2018, MNRAS, 478, 5607, doi: 10.1093/mnras/sty1406

Tremaine, S., Gebhardt, K., Bender, R., et al. 2002, ApJ, 574, 740, doi: 10.1086/341002

Tremonti, C. A., Heckman, T. M., Kauffmann, G., et al. 2004, ApJ, 613, 898, doi: 10.1086/423264

Veilleux, S., Cecil, G., & Bland-Hawthorn, J. 2005, Annual Review of Astronomy and Astrophysics, 43, 769, doi: 10.1146/annurev.astro.43.072103.150610

Veilleux, S., Maiolino, R., Bolatto, A. D., & Aalto, S. 2020, The Astronomy and Astrophysics Review, 28, 2, doi: 10.1007/s00159-019-0121-9

Veilleux, S., & Osterbrock, D. E. 1987, ApJ Supp., 63, 295, doi: 10.1086/191166

Vestergaard, M., & Peterson, B. M. 2006, ApJ, 641, 689, doi: 10.1086/500572

Vito, F., Brandt, W. N., Yang, G., et al. 2018, MNRAS, 473, 2378, doi: 10.1093/mnras/stx2486

Vogelsberger, M., Genel, S., Springel, V., et al. 2014, MNRAS, 444, 1518, doi: 10.1093/mnras/stu1536

Volonteri, M. 2010, The Astronomy and Astrophysics Review, 18, 279, doi: 10.1007/s00159-010-0029-x

Volonteri, M., Lodato, G., & Natarajan, P. 2008, MNRAS, 383, 1079, doi: 10.1111/j.1365-2966.2007.12589.x

Volonteri, M., & Reines, A. E. 2016, ApJ Lett., 820, L6, doi: 10.3847/2041-8205/820/1/L6

Wang, T.-G., Zhou, H.-Y., Komossa, S., et al. 2012, ApJ, 749, 115, doi: 10.1088/0004-637X/749/2/115

Wang, T.-G., Zhou, H.-Y., Wang, L.-F., Lu, H.-L., & Xu, D. 2011, ApJ, 740, 85, doi: 10.1088/0004-637X/740/2/85

Whittle, M. 1985, MNRAS, 213, 1, doi: 10.1093/mnras/213.1.1

Wilson, A. S., & Raymond, J. C. 1999, ApJ Lett., 513, L115, doi: 10.1086/311923

Wylezalek, D., & Morganti, R. 2018, Nature Astronomy, 2, 181, doi: 10.1038/s41550-018-0409-0

York, D. G., Adelman, J., Anderson, John E., J., et al. 2000, AJ, 120, 1579, doi: 10.1086/301513

Zakamska, N. L., & Greene, J. E. 2014, MNRAS, 442, 784, doi: 10.1093/mnras/stu842

Zubovas, K., Nayakshin, S., King, A., & Wilkinson, M. 2013, MNRAS, 433, 3079, doi: 10.1093/mnras/stt952